Hochschule für Angewandte Wissenschaften Hamburg
Hamburg University of Applied Sciences

Bachelor's Thesis

Chhabi Lal Bashyal

Numerical Study of Ultrasound-Based Level Sensors in Liquid Hydrogen Tanks

Fakultät Technik und Informatik
Department Fahrzeugtechnik und Flugzeugbau

Faculty of Engineering and Computer Science
Department of Automotive and Aeronautical Engineering

Chhabi Lal Bashyal

Numerical Study of Ultrasound-Based Level Sensors in Liquid Hydrogen Tanks

Bachelor's Thesis as Part of the Bachelor's Examination
Course of Study: Bachelor of Engineering in Aeronautical Engineering
In Department: Automotive and Aeronautical Engineering
Faculty of Technology and Computer Science
Hamburg University of Applied Science

Supervising Professor: Prof. Dr.-Ing. Kay Kochan
Second Examiner: Prof. Dr.-Ing. Thomas Kletschkowski

Submission Date: 20.11.2024

Chhabi Lal Bashyal

Title of the paper

Numerical Study of Ultrasound-Based Level Sensors in Liquid Hydrogen Tanks

Keywords

LH_2, Piezoelectricity, Impedence, Boiloff, Sloshing, Reflection and Transmission

Abstract

Liquid hydrogen (LH_2) holds immense potential for decarbonizing aviation, offering a sustainable alternative to conventional fuels. However, its adoption is constrained by its lower volumetric energy density, necessitating storage in liquid form at 20 K. Precise LH_2 level measurement in cryogenic aircraft tanks under varying flight conditions presents significant challenges due to its low viscosity, thermal stratification, and the risk of hydrogen embrittlement. This study explores the use of ultrasonic sensors for LH_2 level detection, employing FEM simulations in COMSOL Multiphysics 6.2. The findings reveal that placing the sensor within the LH_2 medium makes level detection feasible due to the low transmission of acoustic waves at the LH_2-GH_2 interface. Under the stationary fluid assumption, using a 50 kHz frequency, the sensor achieved a relative error of 0.65% at a fuel level of 1.9 m, with absolute errors ranging from 12.3 to 12.5 mm. However, cryogenic temperature variations between 18 K and 20 K directly influenced sensor accuracy, with lower temperatures leading to higher absolute errors. Additionally, increasing sloshing angles reduced the sensor's accuracy and detectability. These findings demonstrate the feasibility of ultrasound sensors for reliable LH_2 level measurement. However, practical implementation must address the challenges posed by sloshing effects, thermal stratification, and hydrogen embrittlement to ensure long-term reliability and operational safety.

Contents

List of Tables

List of Figures

List of Abbreviations

CFL	Courant Friedrichs Lewy
CO_2	Carbon Dioxide
EASA	European Union Aviation Safety Agency
FBGs	Fiber Bragg Gratings
FEM	Finite Element Method
FQIS	Fuel Quantity Indication System
FQMS	Fuel Quantity Measurement Systems
GH_2	Gaseous Hydrogen
H_2O	Water
LH_2	Liquid Hydrogen
LN_2	liquid nitrogen
LNG	Liquefied Natural Gas
LOX	Liquid Oxygen
N2O4	Dinitrogen Tetroxide
NASA	National Aeronautics and Space Administration
NOX	Nitrogen Oxides
PDEs	Partial Differential Equations
PTFE	Polytetrafluoroethylene
PZT	Lead Zirconate Titanate
RP-1	Rocket Propellant-1 (Refined Kerosene)
STZ	Strontium Titanate
TOF	Time of Flight
UDMH	Unsymmetrical Dimethylhydrazine
ZEROe	Zero Emission

List of Symbols

Symbol	Unit	Description
c	m/s	Speed of sound
K	Pa	Bulk modulus
ρ	kg/m^3	Density of the medium
Z	kg/(m^2 · s)	Acoustic impedance
ToF	s	Time of flight
γ	-	Specific heat ratio
R	J/(kg·K)	Gas constant
T	K	Temperature
M	kg/mol	Molar mass
θ_I, θ_{II}	rad	Incident and refracted angles
R	-	Reflection coefficient
T	-	Transmission coefficient
ρ_1, ρ_2	kg/m^3	Densities of media 1 and 2
c_1, c_2	m/s	Speeds of sound in media 1 and 2
θ_{cr}	rad	Critical angle
τ_p	-	Transmission pressure ratio
γ_p	-	Reflection pressure ratio
$A(x)$	-	Amplitude at distance x
A_0	-	Initial amplitude
α	m^{-1}	Absorption coefficient
$P(x)$	Pa	Pressure at distance x
P_0	Pa	Initial pressure
α_{cal}	m^{-1}	Calculated absorption coefficient
η	Pa·s	Dynamic viscosity
k	W/(m·K)	Thermal conductivity
C_p	J/(kg·K)	Specific heat at constant pressure
f	Hz	Frequency
f_s	Hz	Resonance frequency of a cylindrical piezoelectric disc
h	m	Thickness of the piezoelectric element

Table 1: List of Symbols, Units, and Descriptions

Symbol	Unit	Description
l_0	m	End of the near field, marking the transition to the far field
d	m	Diameter of the piezoelectric element
λ	m	Wavelength
Z_m	$\mathrm{kg}/(\mathrm{m}^2 \cdot \mathrm{s})$	Impedance of the matching layer
d_m	m	Thickness of the matching layer
c_m	m/s	Speed of sound in the matching layer
$V(t)$	V	Voltage as a function of time
V_0	V	Amplitude of the signal input voltage
f_0	Hz	Frequency of the sinusoidal wave
T_0	s	Period of the sinusoidal wave
λ_{min}	m	Minimum wavelength in the medium
f_{max}	Hz	Maximum frequency
h_{max}	m	Maximum element size for mesh resolution
Δt	s	Time step for simulation
N	-	Number of elements per wavelength
Z_I	$\mathrm{kg}/(\mathrm{m}^2 \cdot \mathrm{s})$	Impedance in medium I
Z_{II}	$\mathrm{kg}/(\mathrm{m}^2 \cdot \mathrm{s})$	Impedance in medium II
ΔC	F (Farads)	Change in capacitance
$\epsilon_{r,\text{liq}}$	-	Relative permittivity of the liquid
$\epsilon_{r,\text{gas}}$	-	Relative permittivity of the gas
ϵ_0	F/m	Permittivity of free space
S	m^2	Surface area of the capacitor
d_0	m	Distance between capacitor plates
M	kg	Mass
V	m^3	Volume
L	m	Distance to the unknown height
D	m	Known distance

Table 2: Additional Symbols, Units, and Descriptions

1 Introduction

1.1 Motivation

The aviation industry is a major contributor to global greenhouse gas emissions, creating an urgent need for climate action. In 2019, the International Air Transport Association (IATA) set a goal for the industry to reach net-zero CO_2 emissions by 2050(14). Technological advancements, fleet renewal, and operational improvements have led to an average annual fuel efficiency gain of 1.3%. Despite these efforts, aviation still accounts for approximately 2.4% of global CO_2 emissions(15). With air traffic demand expected to grow by 3.8% each year, emissions from aviation are projected to increase without significant intervention. In response, the United Nations has proposed ambitious climate action goals, including reducing emissions by 50% by 2030 and achieving net-zero emissions by 2050(16). Meeting these targets requires the aviation industry to adopt cleaner and more sustainable energy sources, with hydrogen emerging as one of the most promising alternatives.

Hydrogen fuel presents a strong pathway for decarbonizing aviation. Unlike kerosene, which releases significant CO_2 emissions, hydrogen produces water vapour during combustion. Research into hydrogen as an aviation fuel has been ongoing for decades, with experimental aircraft proving its feasibility. For instance, in 1988, an experimental aircraft developed in the USSR TU-155 successfully utilized liquid hydrogen to power a single turbofan engine, showcasing the potential of hydrogen powered aviation(17). In 2023 DLR, in collaboration with H2Fly, demonstrated their HY4 aircraft, achieving the world's first manned electric flights powered by liquid hydrogen(18). This milestone, along with Airbus' ZEROe program aiming to launch the first hydrogen-powered commercial aircraft by 2035, underscores the strong potential of hydrogen as a sustainable fuel in aviation.

1.2 Problem Statement

Despite its promise, integrating hydrogen into aviation poses unique challenges, especially when stored as a cryogenic liquid. Liquid hydrogen (LH_2) offers enhanced energy density compared to its gaseous form, enabling more efficient storage within the constraints of aircraft design. However, maintaining hydrogen at cryogenic temperatures below -253° C and ensuring its safe storage and handling introduces significant engineering and technological hurdles. Among these challenges, Precise measurement of LH_2 levels in an aircraft's storage tanks is essential. It is not only crucial for determining the total fuel mass, but also for enabling accurate monitoring and management, which are critical for ensuring the safe and efficient operation of the aircraft.

The PRECISE project, a joint initiative by the University of Applied Sciences (HAW) Hamburg and AUTOFLUG GmbH, seeks to address these challenges by developing a fuel measurement sensor for liquid hydrogen tanks(7). This thesis contributes to the project by focusing on the numerical modelling of an ultrasound sensor for LH_2 level measurement. Ultrasound sensors have been used in aircraft for fuel level measurement; however, their feasibility and potential for accurately measuring LH_2 levels under cryogenic conditions remain uncertain. Factors such as cryogenic temperatures, variable hydrogen density, and fuel sloshing caused by aircraft manoeuvres add complexity to their performance in such environments.

1.3 Objective of the Study

The objective of this thesis is to evaluate the feasibility of ultrasound-based sensor for the measurement of liquid hydrogen levels in cryogenic tanks designed for aircraft applications. This study employs numerical modelling methods to analyse the performance and accuracy of such sensors and addresses the challenges associated with accurate level measurement under cryogenic conditions.

2 State of the Art

2.1 Properties of Hydrogen

Hydrogen is the lightest element, containing a single proton and an electron. It primarily exists as the isotopes Protium (approximately 99.9%), Deuterium, and the rare Tritium. It is mostly found in the stable diatomic H_2 form. Hydrogen is abundantly present on Earth in water (H_2O) and organic compounds, rather than in its Pure form. It is generally produced through the electrolysis of water and steam methane reforming(19).

At standard temperature and pressure, hydrogen is present in the gaseous form and has a very low density of around 0.084kg/m^3. At cryogenic temperatures below 20.4 K and normal pressure, hydrogen transitions to a liquid state with a density of 71 kg/m^3. This density is approximately 845 times greater than that of gaseous hydrogen under standard temperature and pressure conditions(1).

One unique property of hydrogen is the Ortho-Para conversion, where hydrogen molecules transition between two nuclear spin states. At standard temperature, normal hydrogen consists of 75% ortho-hydrogen (o-H_2) and 25% Para-hydrogen (p-H_2). With decreasing temperature, the proportion of Para-hydrogen increases, reaching approximately 99.8% at 20 K in liquid hydrogen (LH_2). The proportion of Ortho- and Para-hydrogen as a function of temperature is shown in Figure 2.1. This conversion is exothermic, releasing heat during the transition. It plays a significant role in cryogenic storage, as the heat generated must be managed to maintain stable temperatures and minimize boil-off losses in liquid hydrogen tanks(1).

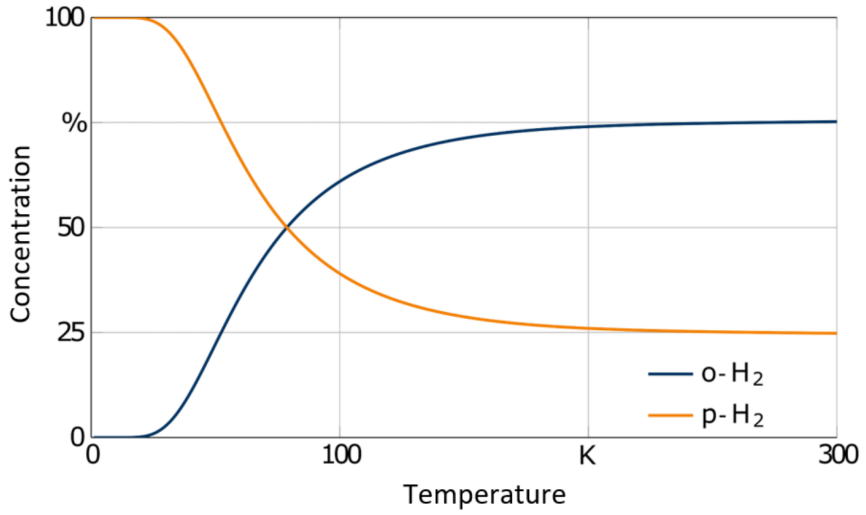

Figure 2.1: Ortho-para Equilibrium concentration of the H_2(1)

The phase behaviour of para-hydrogen, as shown in Figure 2.2, is particularly relevant in cryogenic applications. Its triple point is observed at 13.8 K and 0.07 bar, marking the precise conditions at which solid, liquid, and gas phases coexist (19). At temperatures below 20.3 K, hydrogen can be maintained in a fluid state, making it suitable for storage in LH_2 tanks.

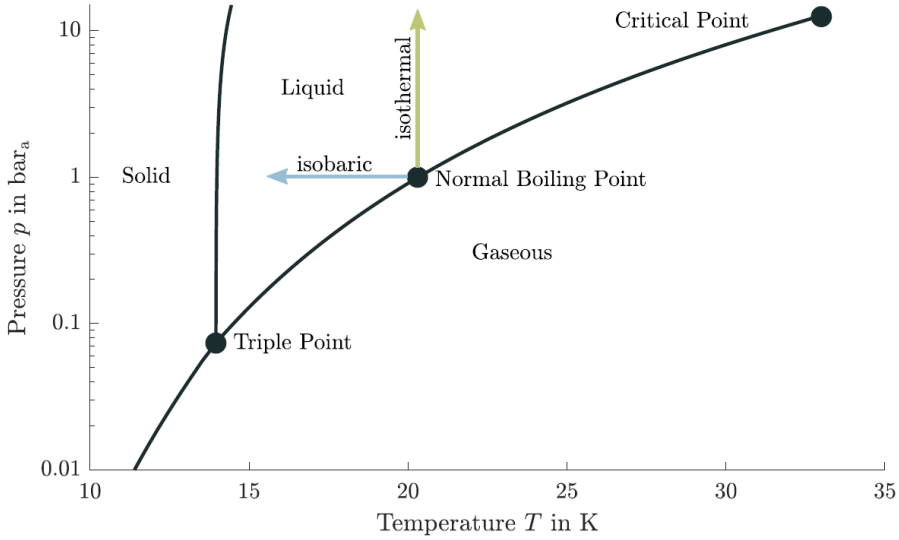

Figure 2.2: Phase diagram of Para-hydrogen(2)

The density of liquid hydrogen along the Vapour pressure line can vary widely under equilibrium conditions, decreasing from 77kg/m^3 at the triple point to 31.3kg/m^3 at the critical point due to temperature fluctuations, as shown in Figure 2.3. In enclosed LH_2 tanks, any unavoidable heat influx raises both pressure and temperature, causing density to decrease through thermal expansion. Due to this reason, a 10%-30% expansion space must be maintained inside the tank.

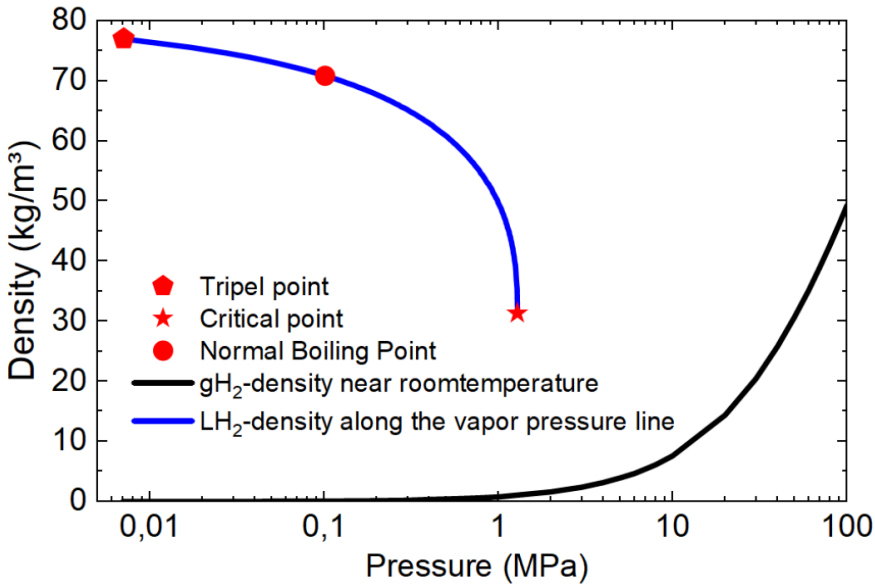

Figure 2.3: Density of LH_2 along the vapour pressure line(1)

Hydrogen is extremely volatile with an ignition energy threshold of 0.017 mJ which is 10 times lower than Kerosene, which should be taken into account while designing the sensor in the LH_2 tank to avoid accidental ignition(2). Hydrogen, as an aviation fuel, has a notably high energy density by mass, with approximately 122.8 MJ/kg, making it one of the most energy-dense fuels per kilogram. In its liquid form, hydrogen achieves a density of about 70.8kg/m^3 at cryogenic temperatures of -253 °C. This low density, however, results in a relatively low energy density by volume, meaning that a larger storage volume is required to be compared to conventional fuels. By comparison, kerosene has an energy density of 42.8 MJ/kg and a much higher density, between 775 and 840 kg/m^3 at ambient conditions. This allows kerosene to store more energy in a compact volume, with roughly four times the volumetric energy density of liquid hydrogen. Consequently, while hydrogen provides significant energy per unit mass potentially reducing overall fuel weight it necessitates substantially larger tanks and advanced insulation systems to

maintain cryogenic temperatures, marking a key difference from the compact storage afforded by kerosene(20).

Acoustic Properties

The propagation of acoustic waves in liquid hydrogen is primarily influenced by thermodynamic properties, such as temperature and pressure, as well as physical characteristics like density and compressibility. These factors directly impact the speed of sound. The speed of sound in the liquid can be calculated using

$$c = \sqrt{\frac{K}{\rho}} \tag{2.1}$$

where K is the bulk modulus and ρ is the density of LH_2. In cryogenic conditions near its boiling point 20.27 K, liquid hydrogen has a speed of sound around 1100 m/s (21). However, this value is sensitive to variations in temperature and pressure, with even slight deviations causing changes in the speed of sound. As shown in Figure 2.4, the speed of sound in LH_2 decreases with increasing temperature. These changes directly influence the time-of-flight (TOF) measurement, which is discussed in detail in Chapter 3.

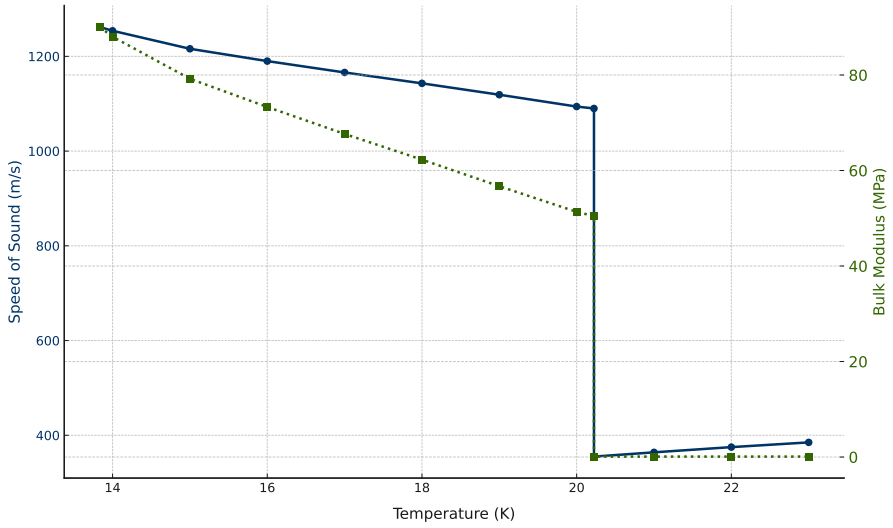

Figure 2.4: Speed of Sound in para Hydrogen at 0.1MPa vs temperature

The acoustic impedance Z, defined by the product of the medium's density and the speed of sound, is calculated as:

$$Z = \rho \cdot c \tag{2.2}$$

As shown in Equation(2.2), the acoustic impedance depends on both the density and the speed of sound, making it a critical parameter for analysing the reflection and transmission of acoustic waves between two fluids. At 20 K and normal pressure, liquid hydrogen (LH_2) has an acoustic impedance of $77789.64\,\mathrm{kg\,m^{-2}s^{-1}}$, which is significantly lower than that of kerosene, approximately $1072000\,\mathrm{kg\,m^{-2}s^{-1}}$ under ambient conditions. The effect of impedance mismatch and the transmission and reflection of acoustic waves are described in more detail in Chapter 3.

Additionally, phenomena like viscosity, and thermal conductivity in cryogenic conditions further influence wave propagation by altering energy dissipation and acoustic absorption. These properties, alongside the low viscosity of liquid hydrogen, make ultrasound wave propagation sensitive to even slight variations in environmental conditions.

2.2 Literature Review and Related Work

Fuel Quantity Measurement Systems (FQMS) are designed to measure the mass of fuel rather than its volume, providing continuous and accurate readings across the full range of fuel quantities. Figure 2.5 illustrates the FQMS of a Boeing 777, which is equipped with 20 ultrasonic sensors in each wing and 12 sensors in the central wing box, along with one densitometer in each tank. The densitometers provide real-time density measurements, which depend on the fuel's temperature. Each Ultrasonic sensor measures the fuel level in the tank with the Known dynamic aircraft conditions. Through the measured level and known tank geometry, the volume of the fuel inside the tank can be determined. With the real-time density measurements, fuel mass (M) inside the tank can be calculated with the following relation:

$$M = \rho \cdot V \tag{2.3}$$

where ρ represents the density, and V is the volume derived from the fuel level, tank shape, and dynamic aircraft conditions.

Mass measurement is critical as it directly corresponds to the stored energy available from the fuel's calorific content, which determines engine thrust. This energy, in turn,

is a direct measure of the aircraft's range. Errors in fuel level measurement can adversely affect the aircraft's range and overall weight and performance, posing significant operational and safety challenges(13).

Another essential function of the level sensors is to ensure sufficient fuel expansion space within the tank by initiating a fuel shut-off mechanism during refuelling(13). As discussed in earlier chapters, LH_2 is highly sensitive to temperature variations, which can affect its density, volume, and overall fuel level. Therefore, to accurately determine the total quantity of LH_2 in the tank, it is vital to precisely measure the LH_2 level, even under varying aircraft dynamics and across the entire operational range.

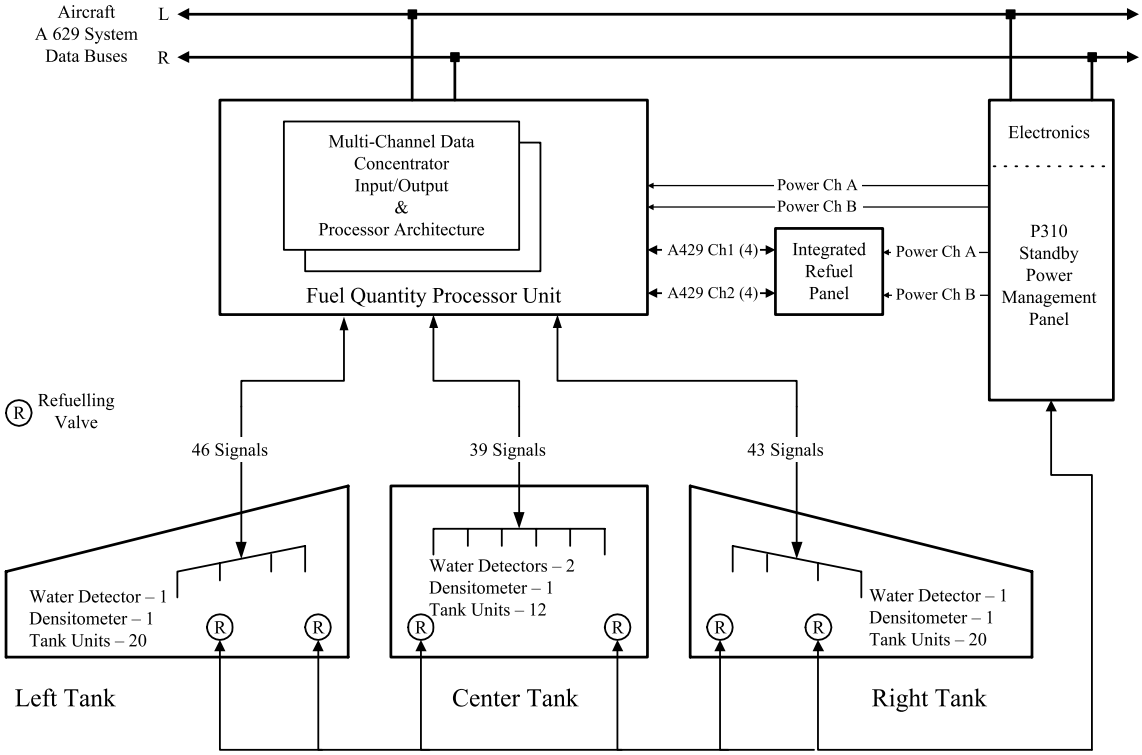

Figure 2.5: Simplified B777 fuel gauging/fuel management System(3)

2.2.1 Ultrasonic Level Sensors in Aircraft

Ultrasonic fuel level sensors emit sound waves from a transducer positioned at the bottom of the fuel tank. The sensor measures the time it takes for these waves to travel through the fuel and reflect from the fuel surface, a method known as the TOF technique, as shown in Figure 2.6. This time interval is then converted into a distance with the

known speed of sound in the Fuel, corresponding to the tank's fuel level. To improve accuracy, ultrasonic reflectors are positioned at a known height within the tank. This reflector provides a reference echo from the known height and with the TOF measured from the reflector, the speed of sound can be calculated accurately. With the real-time Speed of sound and the TOF measured from the fuel level, the Height of the Fuel can be calculated with the following equation:

$$L = \frac{c \cdot TOF}{2} \tag{2.4}$$

where L is the distance to the unknown surface, c is the velocity of sound in the medium, and TOF is the time taken for the wave to make a round trip to the surface.

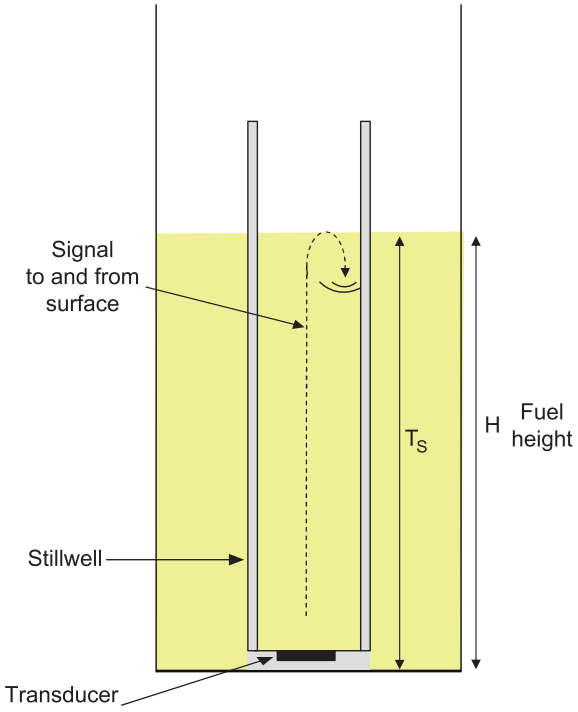

Figure 2.6: Ultrasonic level sensor Probe

However, the only known aircraft types equipped with ultrasonic fuel gauges are the Boeing 777 and the F-22. In contrast, their successors, the Boeing 787 and the F-35(22), reverted to capacitive fuel gauges due to issues with faulty fuel level readings. These inaccuracies were caused by a design flaw in the FQIS and complications related to fuel stratification. Ultrasonic sensors in the FQIS struggled to provide accurate measurements when fuel Temperature and density varied within the tank, leading to discrepancies and

multiple incidents related to the accuracy of the fuel level(23). Ultrasonic liquid level sensors have also been used in the Ariane 1/2/3/4 rockets in the first and second stages, specifically for measuring the levels of the propellants N_2O_4 and UDMH. Over numerous flights, this method proved reliable, with no reported issues(12).

According to the findings of this research, no existing system currently uses ultrasonic-level sensors to measure the level of liquid hydrogen. However, the literature indicates that ultrasonic sensors are capable of detecting the liquid-gas interface of Cryogenic Fluid including LH_2, suggesting their potential application for measuring the level of LH_2(24; 25; 26; 27). As Martin Siegl et al.(25) demonstrated in their experiments on cryogenic liquid nitrogen (LN_2), level sensing presents significant challenges related to the performance of piezoelectric transducers at extremely low temperatures. One key finding is the unavoidable decrease in the oscillation displacement of piezoelectric transducers at cryogenic temperatures. For example, at 77 K in LN_2, the displacement is reduced to 70% of its room temperature value, and at 20 K in liquid hydrogen LH_2, it decreases further to just 30%. Despite these limitations, even at 77 K, the transmitted signal retains an amplitude of several hundred millivolts, sufficient for accurate level evaluation. In another experiment conducted by Amamchyan et al. (27), ultrasonic level sensors were used to measure the levels of LN_2 and LNG. The sensors utilized strontium zirconate titanate (SZT) as the piezoelectric crystal, demonstrating their effectiveness in cryogenic conditions. Chapter 3 builds on this by focusing on the application of ultrasonic transducers in liquid hydrogen and the Challenges Posed by LH_2 for precise level measurement in LH_2.

2.2.2 Alternative Method to Measure LH_2 in Cryogenic Tanks

In this section, alternative methods for cryogenic LH_2 measurement are briefly reviewed.

Fiber Optic Liquid Level Sensor

Fiber optic technology offers an innovative approach to measuring cryogenic liquid levels, utilizing fiber Bragg gratings (FBGs) combined with anemometry principles. This method employs FBGs embedded along a single-mode optical fiber, positioned adjacent to a heating element within protective tubing. By cycling the heating element on and

off, controlled heat pulses are generated, and the rate of temperature change along the fiber is observed during both heating and cooling phases(28).

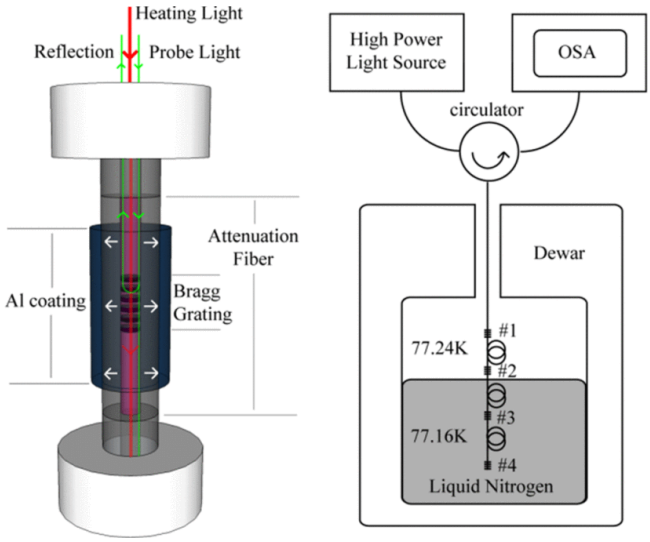

Figure 2.7: Fiber Optic level sensor with fiber Bragg grating(4)

This technique exploits the differing thermal conductivities of the liquid and gas phases to precisely detect the liquid-gas interface. In the gaseous region, the fiber heats up more rapidly due to lower thermal conductivity, whereas in the liquid region, higher thermal conductivity leads to slower temperature changes. Upon deactivating the heater, residual heat dissipates faster in the liquid phase than in the gas phase, allowing for accurate identification of the transition point between the liquid and gaseous H_2(29; 28).

One of the main drawbacks of the fibre optic sensor is its limited resolution, providing measurements only at intervals of 1/4 inch. Additionally, the use of a heating element can increase the boil-off of the cryogenic liquid, leading to potential inefficiencies. Furthermore, this method is significantly more expensive compared to ultrasound sensors, making it less practical for cost-sensitive applications.

Capacitive Fuel Level Sensors

Capacitive fuel level sensors operate by measuring changes in capacitance as the fuel level inside the tank fluctuates. These sensors consist of two conductive plates or electrodes

arranged in parallel, with the liquid fuel acting as the dielectric medium. The change in capacitance, ΔC, as the level of liquid and gas phases fluctuates, is given by

$$\Delta C = (\epsilon_{r,\text{liq}} - \epsilon_{r,\text{gas}})\, \epsilon_0 \frac{S}{d_0} \tag{2.5}$$

where $\epsilon_{r,\text{liq}}$ and $\epsilon_{r,\text{gas}}$ represent the dielectric constants of the liquid and gas phases, respectively, ϵ_0 is the permittivity of free space, S is the electrode surface area, and d_0 is the distance between the plates(30). This relationship allows capacitive sensors to provide a continuous and accurate measurement of fuel levels by detecting the variations in the dielectric medium as the liquid level changes.

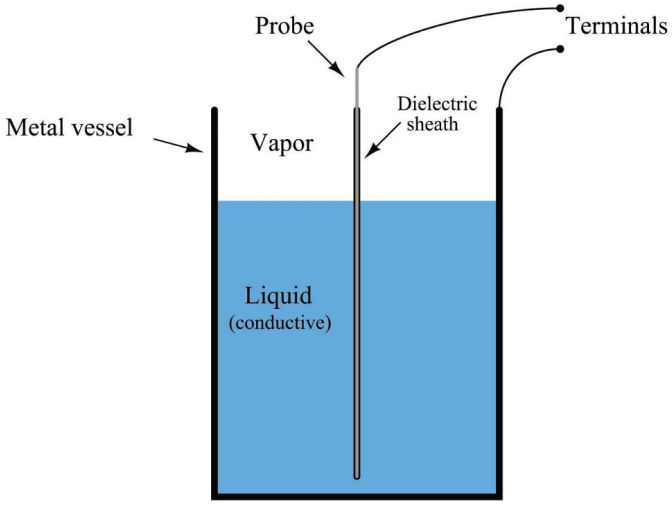

Figure 2.8: Capacitive Level Sensor(5)

Capacitive sensors are widely used in aircraft fuel tanks due to their high precision, and reliability. They provide continuous measurements, which are crucial in dynamic environments, where factors like changes in flight attitude and vibrations can impact sensor accuracy. For cryogenic conditions, such as liquid hydrogen monitoring, the basic principles of capacitive sensing are applied, but with materials that are specifically designed to withstand extremely low temperatures. Research by Matsumoto et al.(30) demonstrated that a capacitive level meter with multi-parallel plate capacitors could effectively measure liquid hydrogen levels at cryogenic temperatures. This method has shown high sensitivity, achieving measurement accuracy better than 0.2 mm, even under pressurized conditions up to 0.2 MPa.

Differential Pressure Level sensor

Differential pressure sensors are a common and effective method for measuring the height and volume of liquids in tanks, including Cryogenic Liquids. These sensors work by measuring the pressure difference between two points, typically one at the bottom of the tank, where the liquid is present, and one at the top, where only the gas phase exists. In cryogenic tanks, the sensor at the bottom detects the combined pressure of the liquid and Vapour above it, while the sensor at the top records the Vapour pressure alone. The difference between these two measurements isolates the pressure attributed solely to the liquid's weight, which is directly proportional to the height of the liquid column. By utilizing the known density of the cryogenic liquid and accounting for the acceleration due to gravity, the sensor can accurately calculate the liquid height. Once the liquid height is determined, the volume can be calculated based on the tank's shape and dimensions(31).

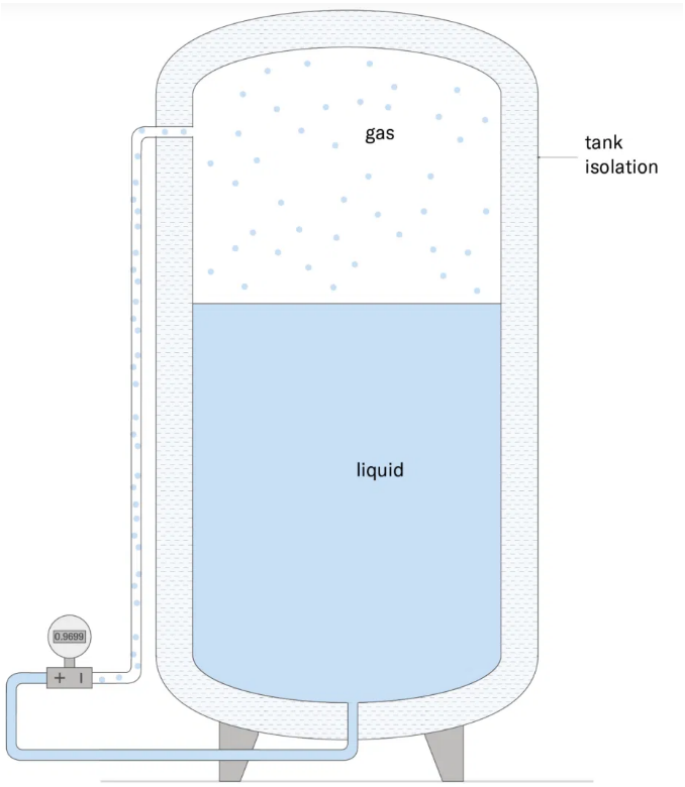

Figure 2.9: Differential Pressure Sensor(6)

In practice, differential pressure sensors have been adopted for monitoring liquid levels in rockets, as seen in the ATLAS 3, 4, and 5 rockets. These sensors were utilized in both the first and second stages to monitor propellant levels (LOX) and RP-1 in the first stage, and LH_2 and LOX in the second stage. Before the upgrade in the 1990s, the ATLAS series used capacitance probes, but differential pressure sensors were introduced as a more cost-effective and dependable solution(32).

2.3 Tank Geometry for Storing Liquid Hydrogen

In conventional aircraft, fuel is typically stored in the wings and the central wing box, which are designed as integral tanks forming part of the aircraft's structure. However, hydrogen necessitates a dedicated fuel tank capable of maintaining cryogenic temperatures. As discussed in section (2.1) in its liquid form, hydrogen has a lower energy density compared to kerosene. This means that the hydrogen fuel tank must be over four times larger than a conventional fuel tank to store an equivalent amount of energy. Hydrogen is stored as a liquid at cryogenic temperatures of approximately 20 K and is pressurized to slightly above atmospheric pressure, at around 1.4–1.5 bar. This pressurization is essential to prevent air leakage into the tank and ensure sufficient net positive suction head (NPSH) for the fuel boost pump(33). To meet these requirements and minimize heat influx, large cylindrical tanks are utilized, as they are the most practical shape after spheres and have the lowest surface to volume ratio(34). However, their size makes it impractical to place them in the wings. For this reason, they are typically placed in the aft section of the fuselage, beyond the pressure bulkhead. The size of the cylindrical tank depends on the aircraft size and the diameter of the aft fuselage. To design a hydrogen-powered aircraft with similar dimensions to the ATR 72, a storage tank with a diameter of 1.9m is required. For an aircraft comparable in size to the A320, the tank diameter needs to be approximately 3.6m(33).

Figure 2.10: Airbus ZeroE conceptual aircraft with Hydrogen Tank(7)

While integral tanks provide advantages such as weight savings and better total gravimetric efficiency, they require the aircraft fuselage to withstand significantly higher loads due to the pressurization of liquid hydrogen(34). This structural challenge makes non-integral tanks the preferred choice for hydrogen-powered aircraft. As shown in Figure 2.10 depicting the ZEROe concept aircraft by Airbus.

2.3.1 Challenges in Hydrogen Storage

One of the significant challenges posed by hydrogen is hydrogen embrittlement. This phenomenon occurs when hydrogen atoms permeate through materials, leading to structural damage. To address this, the materials used in hydrogen storage systems must be resistant to hydrogen embrittlement. Typically, materials like AL2219 and CFRP are employed due to their low density, durability and resistance to hydrogen embrittlement.

To maintain cryogenic temperatures and minimize boil-off of LH_2, specialized insulation is essential. Multilayer insulation (MLI), made from materials with low thermal conductivity, is commonly used for its effectiveness in reducing heat transfer. Another highly efficient insulation technique is vacuum insulation, which significantly minimizes boil-off by creating a vacuum barrier. However, vacuum insulation comes with trade-offs, such as increased structural weight and the energy required to maintain the vacuum, ultimately adding to the overall weight and cost of the fuel system(35).

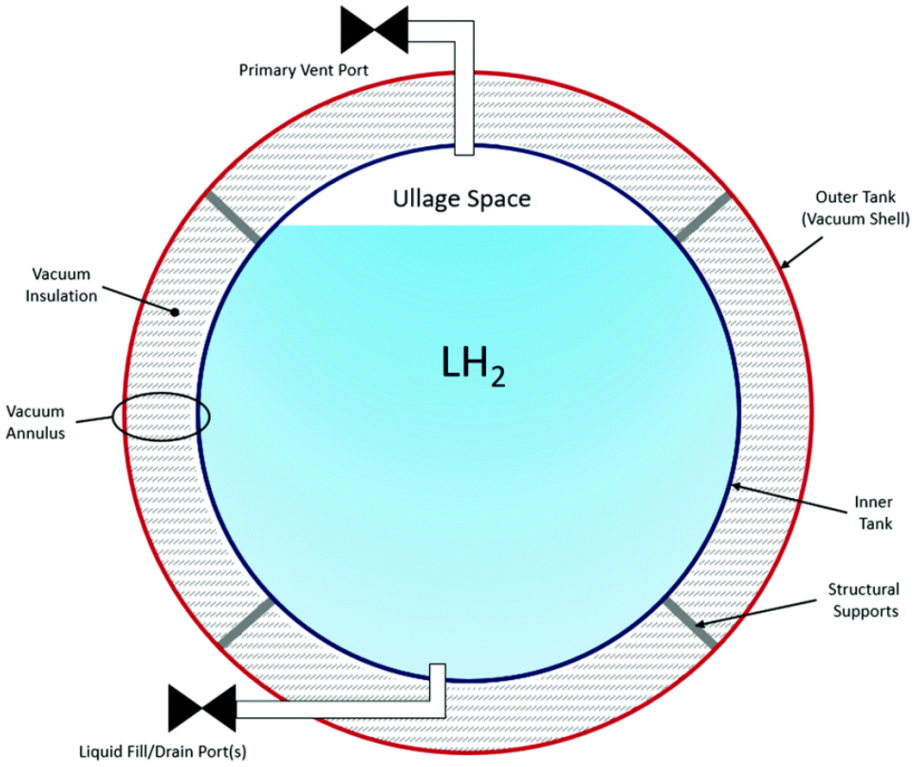

Figure 2.11: Illustration of the Cross-Sectional Area of a Hydrogen Tank(8)

A more cost-effective alternative is foam insulation, which also employs materials with low thermal conductivity. While foam insulation is effective in reducing weight, it is less efficient at minimizing boil-off compared to vacuum insulation, requiring a balance between insulation performance and weight considerations. Figure 2.11 illustrates the cross-section of a vacuum-insulated tank system(35).

2.3.2 Influence of Tank Geometry on Liquid Behaviour and Measurement Accuracy

Tank geometry plays a crucial role in determining the behaviour of liquid hydrogen. The tank's shape, aspect ratio, and volume directly affect fluid dynamics within the tank. An elongated cylindrical tank designed to store LH_2 introduces another challenge. As the level of LH_2 decreases, the fluid is free to move in response to the aircraft's motion. This phenomenon is commonly known as sloshing. This is a well-known issue in conventional aircraft. The motion of the fluid can exert forces on the structure and alter the aircraft's centre of gravity, posing potential stability concerns.

Moreover, due to LH_2's low viscosity, even slight vibrations can induce significant liquid motion within the storage tank, creating sloshing. The sloshing accelerates the boil-off issue by increasing the free surface area of the liquid. LH_2 fuel tank maintains a significant temperature difference between the liquid and gas phases. Sloshing-induced mixing leads to interfacial heat and mass transfer (thermodynamic effects), resulting in undesirable phenomena such as rapid pressure drops and liquid saturation, creating disturbances that complicate pressure regulation.

Furthermore, sloshing negatively influences the accuracy of LH_2 level measurement within the tank, as it introduces dynamic changes to the liquid surface, leading to potential errors in sensor readings(36).

2.3.3 Boil-Off of LH_2 in Cryogenic Tank

The boil-off effect refers to the gradual evaporation of liquid hydrogen due to heat leakage into the storage tank. This phenomenon poses a significant challenge in cryogenic storage systems, as maintaining LH_2 at cryogenic temperatures requires minimizing heat transfer to prevent vaporization. Even a slight temperature increase leads to evaporation, resulting in increased tank pressure. Managing boil-off is crucial for ensuring both operational safety and efficiency (37).

Boil-off is primarily influenced by the insulation and geometry of the storage tank. Although advanced insulation systems such as multi-layer insulation and vacuum insulation significantly reduce heat influx, the inherent properties of hydrogen such as its low viscosity and high thermal conductivity make it prone to vaporization. Any thermal disturbance can expose the liquid phase to warmer gaseous hydrogen, accelerating evaporation (38). The Graphical representation of Boil-off is Presented in Figure 2.12 below:

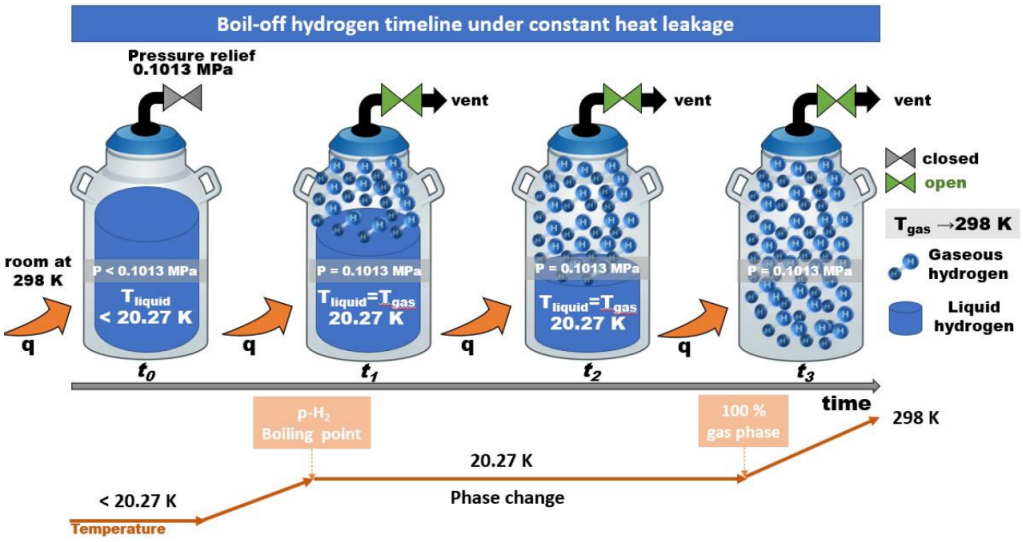

Figure 2.12: Representation of Boil-off phenomenon in LH_2(9)

Multi-layer and vacuum insulations are effective, but even these cannot completely prevent boil-off. Despite these measures, small amounts of heat inevitably penetrate the tank, causing some LH_2 to vaporize into GH_2. This vaporization increases tank pressure, necessitating the use of venting systems to prevent tank failure. Venting, however, is not ideal, as it results in hydrogen loss and increased costs. To address this, tanks are designed with a venting pressure of approximately 3.5 bar, which is sufficient to handle expected boil-off during an aircraft's mission without venting (39).

Tank design constraints, including the interplay of fill pressure, venting pressure, and the required volume allowance for gaseous hydrogen at venting pressure, further limit the maximum fill percentage of the tank. For instance, a maximum fill percentage of 88.5% is commonly specified to accommodate these factors. Additional allowances for internal baffles, tank shrinkage, and unusable fuel further reduce the maximum usable fill percentage by 3.5% to approximately 85% (39).

2.4 Numerical Modelling Methods

One of the most economical and efficient approaches to understanding the behaviour of a system without conducting physical experiments is through numerical modelling. Modelling and simulation tools are extensively used throughout the design and development

process, offering valuable insights into system behaviour. Numerical modelling methods are integral from the concept development phase through system design, development, and verification, and play a critical role during the final stages of system integration and aircraft certification(13). Numerical methods are powerful tools for solving systems of ordinary differential equations (ODEs) and partial differential equations (PDEs). PDEs are the governing equations for time and space-dependent problems. For a wide variety of problems and geometries, it is often not possible to solve these PDEs analytically. In such cases, an approximation of these equations, based on various discretization methods, is used, which becomes solvable with the help of numerical methods(40).

Ultrasound propagation in fluids is derived from the governing equations of fluid flow, while the generation of ultrasound is achieved through the piezoelectric effect, a distinct physical phenomenon. The complexity of real-world problems, often involving coupled physics, makes analytical solutions impractical. For such cases, numerical methods become highly useful. COMSOL Multiphysics software is a powerful tool for addressing these challenges, as it enables the simulation of complex coupled physics problems.

In the Acoustics Module of COMSOL, the physics interfaces are primarily based on the finite element method (FEM). Solving models using FEM requires the creation of a computational mesh, where the solution is approximated on each finite element using shape functions. This discretization process transforms the problem into a system of equations that can be solved numerically(40). To successfully conduct the numerical modelling of the ultrasonic level sensor for measuring the liquid hydrogen level, the process involves multiple stages, as illustrated in Figure 2.13. A detailed explanation of each stage is provided in Chapter 4.

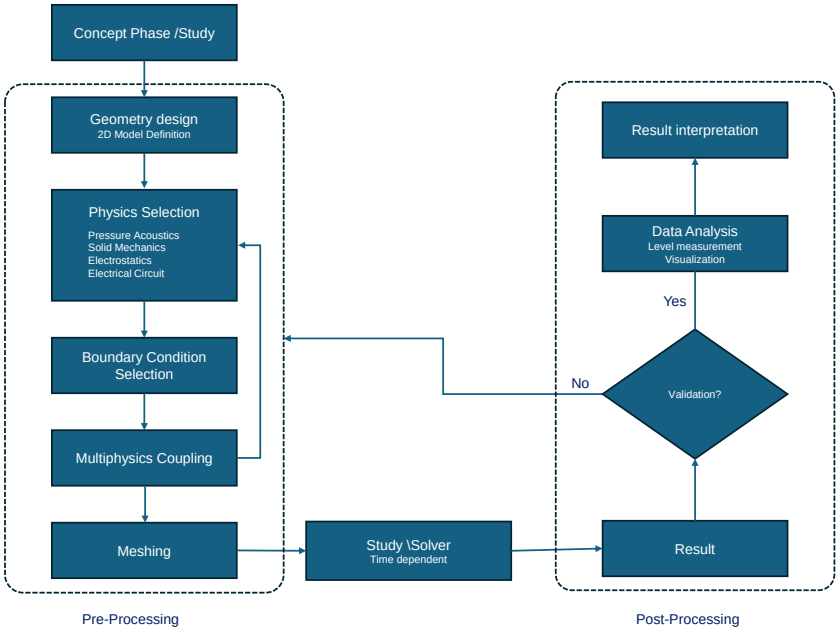

Figure 2.13: Process Framework for FEM Simulations

3 Ultrasonic Level Sensor

Ultrasound refers to mechanical pressure waves with frequencies above the audible range for humans, specifically frequencies beyond 20 kHz, as the human hearing range spans from approximately 20 Hz to 20 kHz. Ultrasound requires a propagation medium and is typically transmitted in the form of longitudinal waves when travelling through fluids. Ultrasonic level sensors generally operate within a frequency range of 40 kHz to 200 kHz, optimized for accurate measurements in various liquid and gaseous environments (41).

3.1 Theoretical Background

Ultrasonic waves used in the level measurement are produced through a transducer, which operates based on the piezoelectric effect. Materials like ceramics and quartz have piezoelectric properties, allowing them to convert electrical signals into acoustic waves and vice versa. When an electrical signal is applied to the transducer, it generates an ultrasonic wave that propagates through the medium. This wave travels until it encounters a boundary, such as the liquid-gas interface. Upon reaching this boundary, part of the wave reflects to the transducer, which detects the returning signal.

By measuring the TOF of the wave and knowing the speed of sound in the medium, the distance to the fluid level can be calculated. The speed of sound in the medium can be determined if the travel distance and TOF are known using the following relation.

$$c = \frac{2D}{TOF} \tag{3.1}$$

where c is the speed of sound, D is the known distance travelled by the wave, and TOF is the time taken for the wave to reach the boundary and return.

When the speed of sound c and the level of the fluid D are known, the Time of Flight (TOF) can be calculated theoretically using the following formula:

$$\text{TOF} = \frac{2D}{c} \tag{3.2}$$

when the speed of sound in the medium is known, the distance to an unknown surface, such as a fluid level, can be calculated by measuring the time of flight:

$$L = \frac{c \cdot TOF}{2} \tag{3.3}$$

where L is the distance to the unknown surface, c is the velocity of sound in the medium, and TOF is the time taken for the wave to make a round trip to the surface.

Alternatively, the speed of sound in LH_2 can be calculated using Equation (2.1), which depends on properties such as temperature, density, and compressibility. For gases like GH_2, the speed of sound c is influenced by the ratio of specific heats, the universal gas constant, temperature, and the molar mass of the gas. It can be determined using the following equation:

$$c = \sqrt{\gamma \cdot \frac{R \cdot T}{M}} \tag{3.4}$$

The accuracy of the ultrasonic level measurement depends on the acoustic impedance of the medium defined by Equation (2.2). Acoustic impedance is an important physical quantity to characterize the acoustic properties of media.

3.1.1 Reflection and Refraction of Ultrasonic wave

When ultrasonic waves encounter an interface between two fluids with different acoustic properties (density and sound speed), the behaviour of the transmitted and reflected waves depends on the acoustic impedance mismatch and the principle of continuous sound pressure and continuous vibration velocity on the interface, which leads to Snell's law of refraction and determines the conditions for the reflection and transmission of sound(10). For an incident angle θ_I in the first fluid as shown in the Figure 3.1, Snell's law governs the angle of refraction θ_{II} in the second fluid:

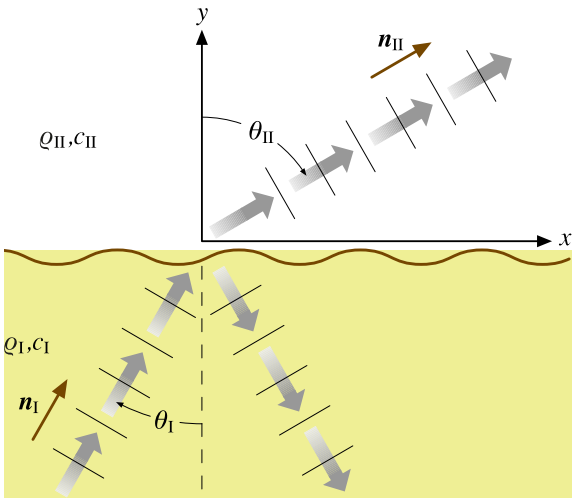

Figure 3.1: Reflection and transmission of sound in two medium(10)

$$\frac{\sin\theta_I}{c_1} = \frac{\sin\theta_{II}}{c_2} \tag{3.5}$$

Where c_1 and c_2 are the speeds of sound in the first and second fluids, respectively. This relation indicates that a change in propagation direction, or refraction, occurs at the interface due to the difference in sound speeds.

To satisfy the conditions of continuity at the interface, the pressure and normal components of fluid velocity must remain continuous across the boundary. This leads to the following relations for the reflection and transmission coefficients:

Continuity of Pressure

$$1 + R = T \tag{3.6}$$

Continuity of Normal Velocity

$$\cos\theta_I \frac{1-R}{\rho_1 c_1} = \cos\theta_{II} \frac{T}{\rho_2 c_2} \tag{3.7}$$

From these relations, the reflection coefficient R can be derived as:

$$R = \frac{Z_{II} - Z_I}{Z_{II} + Z_I} \tag{3.8}$$

Where:

$$Z_I = \frac{\rho_1 c_1}{\cos\theta_I} \tag{3.9}$$

$$Z_{II} = \frac{\rho_2 c_2}{\cos\theta_{II}} \tag{3.10}$$

Here, Z_I and Z_{II} are the acoustic impedances of the two fluids, accounting for their densities (ρ_1 and ρ_2) and sound speeds (c_1 and c_2), adjusted by the cosine of the incident and transmitted angles.

If the speed of sound in the second fluid c_2 is greater than that in the first fluid c_1, a critical angle θ_{cr} exists:

$$\theta_{cr} = \arcsin\left(\frac{c_1}{c_2}\right) \tag{3.11}$$

When θ_I exceeds θ_{cr}, total reflection occurs, and an inhomogeneous plane wave is generated in the second medium. This wave propagates along the x-axis and decays exponentially in the y-direction.

When ultrasonic waves are perpendicularly located on the two mediums with different acoustic impedances, the reflected wave returns in a path opposite to the incident wave, and the rest of the ultrasonic waves penetrate the interface and enter the second medium. The reflection coefficient and transmission coefficient of sound pressure can be obtained by Equation (3.12) and Equation (3.13)

$$\tau_p = \frac{P_t}{P_0} = \frac{2Z_{II}}{Z_I + Z_{II}} \tag{3.12}$$

$$\gamma_p = \frac{P_r}{P_0} = \frac{Z_{II} - Z_I}{Z_{II} + Z_I} \tag{3.13}$$

where P_0 is the incident sound pressure; P_r is the reflected sound pressure; P_t is the transmitted sound pressure. Z_I is the acoustic impedance of the medium on the incident side; Z_{II} is the acoustic impedance of the medium on the transmission side(42).

Parameter	Z
LH_2	78079.84
GH_2	453.84

Table 3.1: Impedance values for LH_2 and Gaseous Hydrogen GH_2

Table 3.1 presents the calculated impedance values for LH_2 at 20K and GH_2 at 22K, both under a pressure of 1.5 bar. These values were obtained using the impedance Equation (2.2).

With GH_2 as the initial medium and LH_2 as the transmission medium, the total reflected pressure coefficient, calculated using Equation (3.13), is 0.9884. This indicates that the reflected wave will have the same phase as the incident wave. Furthermore, according to Equation (3.12), the transmission coefficient is 1.9884, meaning that the transmitted wave will have a larger amplitude than the incident wave. Despite this higher amplitude in the transmitted wave, energy remains conserved across the interface, consistent with the principles of wave transmission(43). As illustrated in Figure 3.2, the transmitted pressure in the LH_2 medium demonstrates both increased amplitude and larger wave transmission from GH_2 into LH_2.

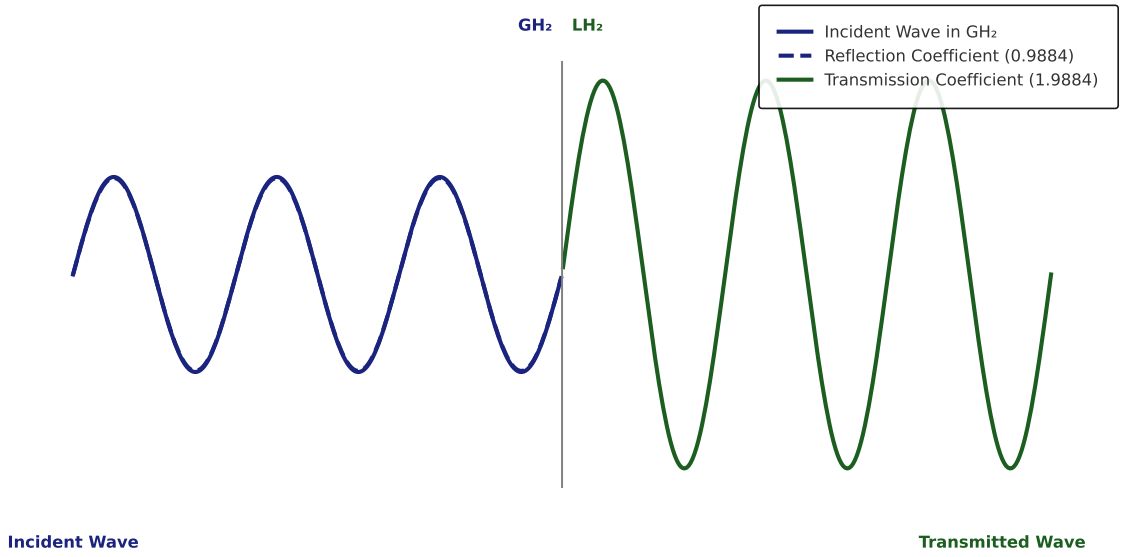

Figure 3.2: Reflection and transmission coefficient from GH_2 to LH_2 Transmission

With LH_2 as the initial medium and gaseous hydrogen GH_2 as the transmission medium, the calculated reflection coefficient is -0.9884. This negative value signifies that the reflected wave maintains almost the same amplitude as the incident wave but with an inverted phase, creating a 180-degree phase shift relative to the incoming wave. The transmission coefficient, on the other hand, is 0.0115578, indicating that only a very small portion of the incident wave amplitude passes into the GH_2 medium. This minimal transmission reflects the substantial acoustic impedance mismatch between LH_2 and

GH_2, causing the majority of the wave energy to reflect into the LH_2. As depicted in Figure 3.3, this interface results in negligible wave transmission into GH_2.

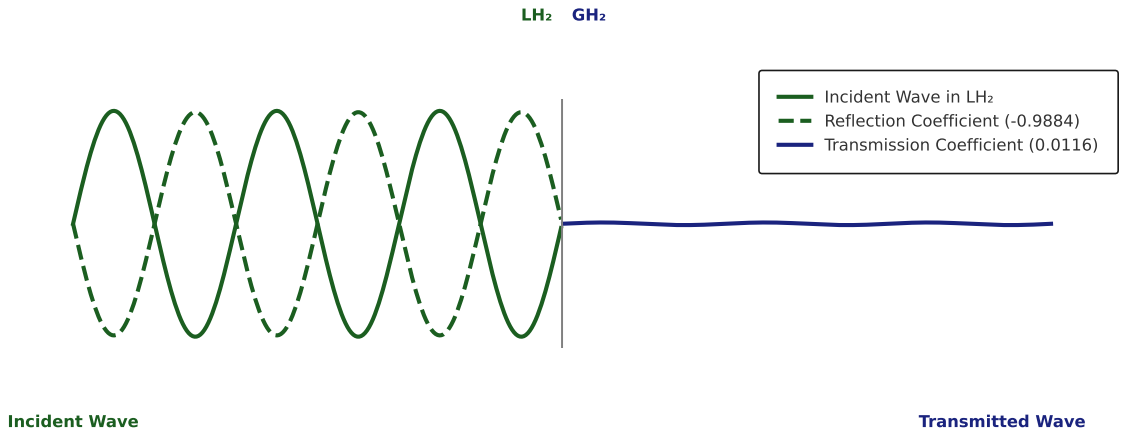

Figure 3.3: Reflection and transmission coefficient from LH_2 to GH_2 Transmission

Building upon this finding, the ultrasound transducer will be positioned in the LH_2 medium, with LH_2 as the incident medium and GH_2 as the transmission medium. This configuration maximizes reflection and minimizes transmission losses at the liquid-gas interface, ensuring high signal clarity and accurate LH_2 level measurements.

3.1.2 Attenuation of ultrasound

Another factor to consider is the attenuation of ultrasound, which encompasses the combined effects of sound scattering where sound waves are deflected from their original path and absorption, where sound energy is converted into other forms of energy.

For a longitudinal ultrasound wave generated by a piezoceramic crystal, the change in wave amplitude can be described by the following relationship:

$$A(x) = A_0 \cdot e^{-\alpha x} \tag{3.14}$$

where $A(x)$ represents the wave amplitude at a distance x, A_0 is the initial amplitude, and α denotes the attenuation coefficient. It can be observed that, with increasing distance, the sound amplitude decays exponentially. Therefore, only a portion of the energy is reflected downward by the LH_2/GH_2 interface. The amount of sound energy reflected in the crystal can be quantified in this manner(13).

The experimental attenuation α_{exp} is defined by the relation:

$$P(x) = P_0 e^{-x\alpha_{\text{exp}}} \tag{3.15}$$

The variable x represents the distance between the point where the peak pressure of the sound wave is P_0 and the point where it reaches P. The attenuation coefficient can be theoretically determined using the following formula:

$$\alpha_{\text{cal}} = \frac{2\pi^2}{\gamma c}\left[\frac{4}{3}\eta + \frac{k(\gamma-1)}{C_p}\right]\frac{f^2}{P} \tag{3.16}$$

where γ is the specific heat ratio, c is the speed of sound, f is the frequency, P is the pressure, η is the dynamic viscosity, and k is the thermal conductivity(21).

This equation accounts for losses due to viscous absorption and thermal conduction, which cause the ultrasound wave to attenuate as it propagates through the medium. From the above Equation (3.16), it is evident that attenuation increases with the square of the frequency. For applications such as LH_2 tank level measurement, where longer propagation distances are required, lower frequencies are advantageous. They experience reduced attenuation, allowing the ultrasound wave to travel farther while maintaining higher pressure amplitudes. In contrast, higher frequencies, while providing greater resolution, suffer from greater attenuation and are less suitable for longer distances in the LH_2 medium.

3.1.3 Governing Equation for Pressure Acoustics in FEM

The governing equations for sound propagation in fluids are derived from the fundamental principles of fluid flow, including the conservation of mass (continuity equation), conservation of momentum (Navier-Stokes equations), and conservation of energy (energy conservation equation). Constitutive equations define the material properties, while an equation of state establishes the relationship between thermodynamic variables. Under the assumptions of classical pressure acoustics, which accurately describe most acoustic phenomena, the flow is considered lossless and adiabatic, viscous effects are neglected, and a linearized isentropic equation of state is used(44).

Under these assumptions, the acoustic field can be described by a single variable, the acoustic pressure p, governed by the linear acoustic wave equation:

$$\frac{1}{\rho_0 c^2}\frac{\partial^2 p}{\partial t^2} + \nabla \cdot \left(-\frac{1}{\rho_0}\nabla p\right) = 0 \tag{3.17}$$

where ρ_0 is the equilibrium density of the fluid, c is the speed of sound in the fluid, p is the acoustic pressure, and t is time. This equation represents the fundamental linear wave equation for pressure acoustics, capturing the essential behavior of sound propagation under the linear acoustic approximation.

In the linear elastic fluid model, the total pressure p_t is given by the sum of the static pressure p and the perturbation pressure p_b, as shown:

$$p_t = p + p_b$$

The governing equation for sound propagation in a linear elastic fluid model, incorporating both monopole and dipole sources, is:

$$\frac{1}{\rho c^2}\frac{\partial^2 p_t}{\partial t^2} + \nabla \cdot \left(-\frac{1}{\rho}\nabla p_t - \mathbf{q_d}\right) = Q_m \tag{3.18}$$

where p_t is the total pressure, p is the static pressure, p_b is the perturbation pressure, ρ is the density of the medium, c is the speed of sound in the medium, ∇ denotes the nabla operator, $\mathbf{q_d}$[1] is the dipole source term, and Q_m[2] is the monopole source term. Both terms are later neglected in the simulation.

For media such as LH_2 and GH_2, additional attenuation effects arise due to thermoviscous damping, which includes both viscous absorption and thermal conduction. To account for these effects, a thermoviscous damping term is incorporated into the model, characterized by the thermoviscous diffusivity term δ, given by:

$$\delta = \frac{1}{\rho}\left(\frac{4\mu}{3} + \mu_B + \frac{(\gamma - 1)k}{C_p}\right) \tag{3.19}$$

where ρ is the density of the medium, μ is the dynamic viscosity, μ_B is the bulk viscosity, γ the ratio of specific heats, k is the thermal conductivity, and C_p is the specific heat capacity at constant pressure.

[1] domain volumetric source
[2] domain source with uniform strength in all directions

The final governing equation for pressure acoustics in LH_2-GH_2 systems, incorporating thermoviscous damping, is:

$$\frac{1}{\rho c^2}\frac{\partial^2 p_t}{\partial t^2} + \nabla \cdot \left(-\frac{1}{\rho}\nabla p_t - \mathbf{q_d}\right) + \frac{\delta}{\rho c^2}\frac{\partial}{\partial t}\nabla p_t = Q_m \tag{3.20}$$

where p_t is the acoustic pressure, ρ is the density of the medium, c is the speed of sound in the medium, ∇ denotes the nabla operator, $\mathbf{q_d}$ is the dipole source term, δ is the thermoviscous diffusivity term, and Q_m is the monopole source term(40).

Building upon the theoretical framework of attenuation, this governing Equation (3.20) comprehensively captures the thermoviscous dissipation effects in both LH_2 and GH_2 medium. It accounts for the propagation and attenuation of acoustic waves in both phases, providing an accurate model for analysing acoustic behaviour in Hydrogen. This governing equation will be applied in the pressure acoustics simulation section of this thesis to evaluate acoustic wave propagation and attenuation characteristics in LH_2-GH_2 medium.

3.2 Piezoelectric Transducer

Piezoelectric transducers convert electrical energy into Acoustic waves through the piezoelectric effect. These transducers consist of key components: the matching layer, backing layer, active element, and housing, as shown in Figure 3.4. The matching layer enhances acoustic wave transmission to the surrounding medium. The backing layer, made of absorbing material, dampens vibrations behind the active element. The housing protects the transducer from environmental damage and secures its components.

Two main techniques are used in pulsed operation to measure the time of flight with ultrasound transducers: through-transmission and pulse-echo. In through-transmission, one transducer sends an ultrasound signal while another receives it, detecting changes caused by defects, fluid velocity or level of the Fluids. The pulse-echo technique, used in this thesis, employs a single transducer to send pulses and receive echoes from LH_2-GH_2 interfaces.

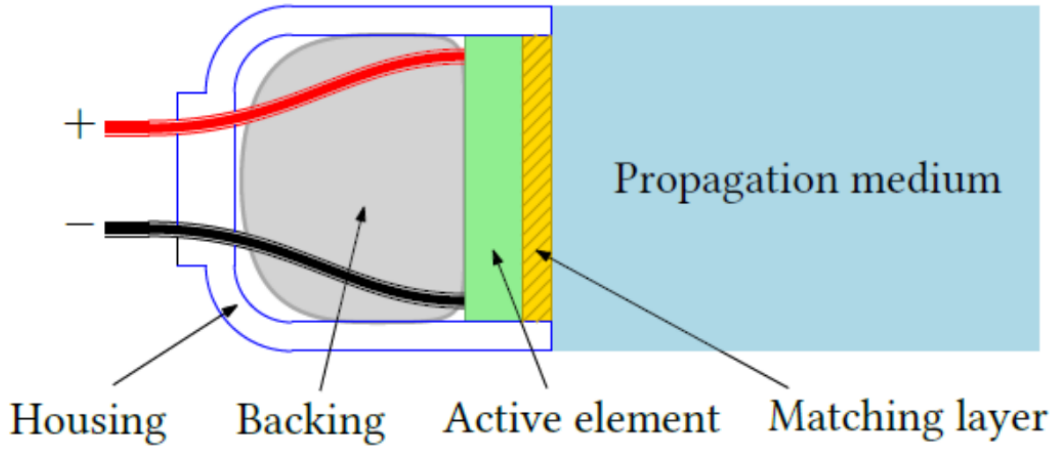

Figure 3.4: Component of Piezoelectric Transducer(11)

Active element

The active element in a piezoelectric transducer is essential for energy conversion, utilizing materials with specific piezoelectric properties to transform electrical energy into acoustic energy. Piezoelectric materials are categorized into two main types: hard and soft. Hard materials have lower piezoelectric constants but high mechanical quality factors, making them durable for high-power applications with continuous signals. Soft materials, with higher piezoelectric constants, are more responsive to signals and are commonly used in sensing applications with single or multiple pulses.

The most widely used piezoceramic material in ultrasonic transducers is lead zirconate titanate (PZT). PZT offers a high electromechanical coupling coefficient and a high dielectric constant, enabling effective electrical matching to cables and electronics, typically in the range of 50Ω to 80 Ω(11). For numerical modelling in COMSOL, PZT-5H was Chosen with Material Properties required for Simulations are already Provided in COMSOL.

Parameter	Value with Unit
Density	$7500\,\text{kg/m}^3$
Piezoelectric constant (d_{33})	$593\,\text{pC/N}$
Speed of sound	$4580\,\text{m/s}$
Acoustic impedance	$34.35\,\text{MRayl}$[3]

Table 3.2: Properties of PZT-5H

However, PZT's large acoustic impedance, compared to LH_2's 0.08 MRayl, significantly limits energy transfer. Using Equation (3.12), the transmission coefficient indicates that only 0.46% of the amplitude of the generated acoustic pressure enters the LH_2 medium. This limitation necessitates the use of a matching layer to enhance the transmission of acoustic waves into the LH_2 medium.

The thickness of the PZT material directly affects the resonance frequency. To generate 50 kHz acoustic pressure, the transducer thickness must correspond to the resonance frequency of the piezoelectric transducer.

The resonance frequency f_s of a cylindrical piezoelectric disc is governed by the relationship:

$$f_s = \frac{c}{2 \cdot t} \tag{3.21}$$

where t is the thickness of the element, and c is the speed of sound in the material.

According to a similar experiment conducted by Wanjia Gao et al.(42) for level detection in water, it was found that a transducer diameter of 15 mm provided the most favourable results, increasing the detectability of the received signal. The experiment was conducted using 5 V, 10 V, and 15 V as excitation signals, with 15 V generating greater initial acoustic pressure and better signal retention. Based on these findings, 15 V and a 15 mm diameter were selected for the simulation. The choice of 15 V also aligns with the constraints posed by ultrasound sensors used in aircraft, ensuring compliance with safety regulations(45).

According to ultrasonic field theory, the emitter diameter d and wavelength λ shape the acoustic field's structure. In the near field, which is located close to the transmitter, wave interference creates fluctuations in sound intensity due to overlapping wavefronts emitted from the piezoelectric surface. Beyond this region lies the far field, where the ultrasonic beam stabilizes and becomes more uniform(22).

[3] $1\,\text{MRayl} = 10^6\,\text{kg} \cdot \text{m}^{-2} \cdot \text{s}^{-1}$

For optimal LH_2 level detection, the sensor should ideally measure at the start of the far field, where interference diminishes, and the acoustic field reaches uniformity. The end of the near field, l_0, which defines the transition to the far field, can be calculated as:

$$l_0 = \frac{d^2}{4\lambda} \tag{3.22}$$

where

$$\lambda = \frac{c}{f} \tag{3.23}$$

and λ is the wavelength, c is the speed of sound in the medium, and f is the frequency of the emitted signal.

Thus, the dimensions and geometry of the piezoelectric material influence both the resonance frequency and the spatial distribution of the ultrasonic field. At 20 K and a frequency of 50 kHz, the near field extends up to 2.194 mm. Therefore, to correctly measure the level of LH_2, the liquid hydrogen level should lie beyond the near field.

The piezoelectric properties of materials are highly temperature-dependent, as discussed in Section (2.2.1). Daniel E. Grupp et al. (46) found that Strontium Titanate (STZ) exhibits a giant piezoelectric effect at cryogenic temperatures, with its response increasing rapidly below 50 K. At approximately 1 K, STZ's piezoelectric response was comparable to that of the best-performing materials at room temperature. In contrast, the piezoelectric material used by Martin et al. (25) retained only 30% of its piezoelectricity at 20 K, highlighting the superior performance of STZ in cryogenic conditions.

The purpose of this study, however, is to investigate the key acoustic interactions between LH_2 and GH_2 media to evaluate the feasibility of ultrasound-based level measurement. The selection of piezoelectric materials is beyond the scope of this thesis. Therefore, PZT-5H was used, as it has well-defined material properties and facilitates the analysis of acoustic interactions within a system.

Matching Layer

The significant acoustic impedance disparity between LH_2 and PZT results in reduced energy transfer into the LH_2 medium. To enhance energy transmission, a matching layer with a thickness equal to one-quarter of the resonance wavelength is required. The acoustic impedance of this matching layer is selected to be intermediate between that of the PZT element and LH_2, with the specific value essential for minimizing reflections

of the ultrasonic wave. In theory, complete transmission for a sinusoidal wave occurs when the following conditions are met:

$$Z_m = \sqrt{Z_{II} \cdot Z_I}, \tag{3.24}$$

The parameter Z_m represents the acoustic impedance of the matching layer, while Z_{II} and Z_I denote the impedances of liquid hydrogen (LH_2) and the PZT element, respectively. Based on calculations using the impedance value of LH_2 at 20 K, the optimal value of Z_m is approximately 1.66 MRayl. Polyurethane (RP-6422) exhibits an acoustic impedance close to this value, approximately 1.66 MRayl, with a density of 1040 kg/m^3 and a speed of sound around 1600 m/s at room temperature (47).

Additionally, the thickness d_m of the matching layer should satisfy:

$$d_m = \frac{c_m}{4f}, \tag{3.25}$$

where d_m represents one-quarter of the wavelength at the matching layer's resonance frequency, c_m is the speed of sound in the matching layer, and f is the frequency.

However, when exposed to LH_2, polyurethane is susceptible to hydrogen embrittlement. Therefore, alternative materials with similar acoustic properties or a multilayer matching structure using materials resistant to hydrogen embrittlement should be considered for practical applications.

In practice, however, full transmission is unachievable with just one matching layer. The acoustic mismatch between LH_2 and the PZT material produces reflected waves that reverberate inside the transducer, causing prolonged ringing of the ultrasonic pulse, which is known as the ringing effect. To reduce this, a backing layer is typically used to absorb part of the energy from the vibration at as shown in Figure 3.4(11).

Backing Layer

The ringing effect makes the transducer emit a pulse for a long time, which reduces the axial resolution of the signal. This oscillation of the PZT element can be reduced by placing a lossy backing material behind it. This material absorbs a large part of the energy. Although this reduces the signal amplitude, it improves the resolution.

If there is a mismatch in acoustic impedance between the active element and the backing material, more energy is reflected into the medium. As a result, the transducer

exhibits lower resolution due to a longer waveform duration but higher sensitivity because of the stronger signal amplitude. The primary goal is to enhance the transducer's sensitivity by emitting a stronger signal and receiving a higher amplitude of the reflected waveform. To achieve this, the backing material is designed with a significant impedance mismatch relative to the PZT material(11).

However, this prolonged emission of a single pulse may be beneficial for measuring higher LH_2 levels, as it allows the signal to propagate effectively over larger distances. At lower LH_2 levels, however, it can cause interference with the received signal due to overlapping reflections, which should be carefully mitigated to avoid measurement inaccuracies.

Housing

As discussed in Chapter 2, vacuum insulation is preferred between the insulation layers to minimize heat transfer into the LH_2 tank and reduce boil-off. Ultrasound waves cannot propagate through a vacuum, which means ultrasonic transducers cannot be used as a non-invasive level sensing method in vacuum-insulated tanks.

For a contact transducer, the housing must be durable and corrosion-resistant. The material must be chosen to withstand hydrogen embrittlement. Suitable materials for the transducer body include Polytetrafluoroethylene (PTFE), which can operate in the temperature range of $-260°\mathrm{C}$ to $+260°\mathrm{C}$ and are resistant to hydrogen embrittlement.

3.3 Factors Affecting Measurement Accuracy

The primary objective of the ultrasound level sensor is to accurately measure the LH_2 level during all flight phases of an aircraft. Besides the attenuation of ultrasound in LH_2, Variations in density and temperature can significantly affect sensor readings. This section discusses the factors that hinder accurate LH_2 level measurement, including thermal stratification and sloshing modes, both of which can impact sound propagation and sensor accuracy, and discusses the industry-standard methods to measure the level despite these challenges.

3.3.1 Thermal Stratification

During the ascent and descent of the flight, there are variations in ambient temperature, resulting in different rates of heat transfer into the Cryogenic Tank. Less heat transfer occurs at lower temperatures, while higher temperatures lead to increased heat influx.

Heat transfer from the surrounding ambient environment into a cryogenic tank induces temperature variations, resulting in density differences between the liquid adjacent to the tank wall and the bulk liquid. This temperature gradient causes the liquid near the wall, which is at a lower density, to rise due to buoyancy forces, as illustrated in Figure 3.5. This movement leads to the accumulation of warmer liquid near the vapour-liquid interface, creating a temperature gradient along the vertical axis of the commonly known as Thermal stratification

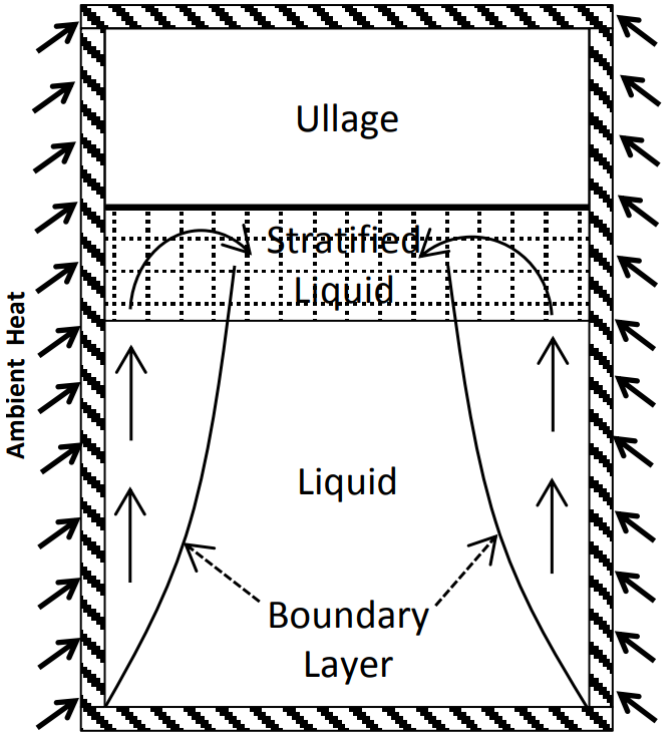

Figure 3.5: Liquid stratification phenomenon in a cryogenic tank(12).

Although the use of a vacuum-insulated tank significantly reduces heat influx and subsequent boil-off, complete elimination of heat transfer is not possible. Due to the temperature and corresponding density gradients, the speed of sound within the LH_2 also varies along these gradients. In LH_2, within the temperature range of 13K-20K, a

temperature change of just 1 K can result in a 2-3% variation in the speed of sound(21). In comparison, kerosene exhibits only a 0.3% change in the speed of sound per degree of temperature variation, which is approximately ten times smaller than that of LH_2. This sensitivity of LH_2 to temperature changes significantly affects the accuracy of level measurements, making it crucial to determine the real-time speed of the Sound of LH_2 in the tank, to determine the accurate level using an ultrasonic sensor. The real-time thermal stratification is hard to model as the heat influx into the tank changes continuously during filling and flight, therefore remains uncertain(12).

3.3.2 Dynamic Condition

As discussed in the earlier section (2.3.2), the dynamic movement of an aircraft causes sloshing of the fluid inside the tank, leading to variations in the surface level of the LH_2 depending on the aircraft's motion. Changes in the surface level can cause the ultrasound echo to reflect away from the transducer, resulting in a weak signal. Additionally, depending on the location of the transducer, this can lead to an overestimation or underestimation of the fluid level in the tank.

To minimize sloshing, baffle structures are typically incorporated into the tank. However, due to the partial fill nature (up to 85% capacity) and the low viscosity of LH_2, even slight movements can induce sloshing. Under severe conditions, sloshing can lead to boil-off and the formation of bubbles in the tank, causing premature reflections of the sound waves to the transducer. This results in an underestimation of the measured liquid level, further complicating accurate measurements.

Therefore, when designing the ultrasound level sensor for LH_2, it should be placed in a location within the tank that is less prone to sloshing and away from the refuelling valve to reduce measurement errors during the refuelling process and ensure reliable operation. The number and location of probes should be determined through tank geometry models and simulations, which account for fuel surface dynamics under varying fuel quantities, aircraft attitudes, and g-forces. These models are essential for optimizing the probe array configuration, improving measurement accuracy, and analysing unusable and measurable fuel quantities.

Dead Zone and Calibration in Ultrasound Level Measurement

Another factor influencing the accuracy of level measurement in LH_2 tanks is the dead zone, an unmeasurable liquid level near the sensor. This occurs due to the dimensions of the transducer and the width of the near field region surrounding it. As the LH_2 level decreases, the time required for the emitted ultrasound pulse to travel to the surface and reflect shortens. In this situation, interference between the transmitted pulse and the received echo can occur, introducing noise into the signal and complicating signal processing.

To mitigate this issue, the duration of the emitted pulse must be carefully calibrated based on the level of LH_2 in the tank. This calibration ensures that the processor can effectively distinguish between transmitted and received signals, minimizing overlap and noise.

For larger measurement distances, high-amplitude signals and longer emitted pulses are more suitable. These accommodate factors like attenuation, which becomes more significant over longer distances. However, this requires precise optimization to balance resolution and avoid excessive overlap or loss of signal clarity in the lower fill levels. Additionally, the applied energy in the circuit to generate ultrasound waves must remain below the ignition energy of hydrogen to ensure safe operation.

3.4 Design of Measurement system

To cope with the challenges posed by thermal stratification, it is necessary to continuously measure the speed of sound within the LH_2 tank. This real-time measurement helps to compensate for the variations caused by thermal stratification and ensures an accurate determination of the LH_2 level.

Additionally, to address the effects of sloshing, it is essential to utilize multiple ultrasonic-level measurement probes. A typical layout consists of a single velocity meter and at least two ultrasonic sensors with Stillwell, as shown in Figure 3.6. By combining the real-time speed of sound measurements with level data from both sensors and accounting for varying flight conditions, the more accurate level of LH_2 can be determined using ultrasonic level sensors.

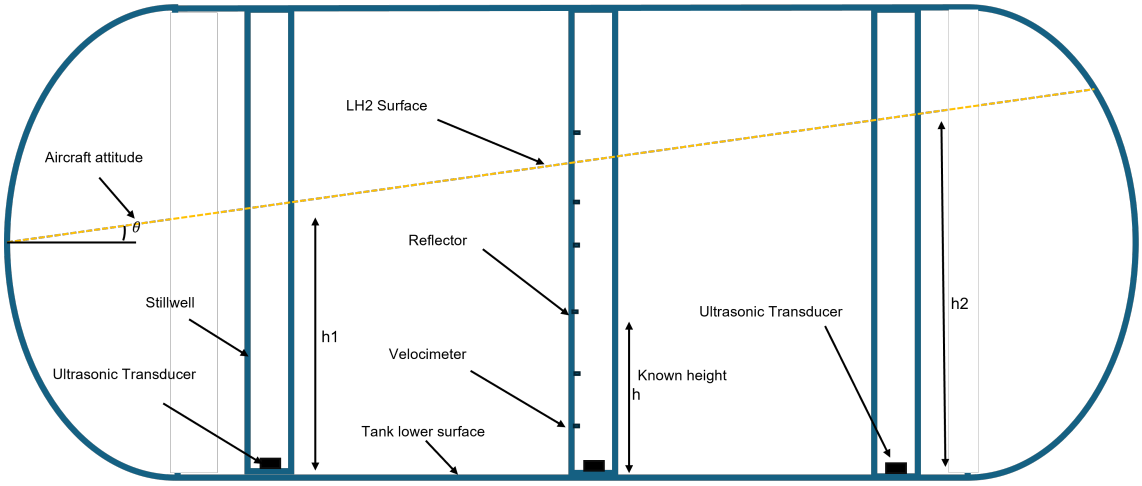

Figure 3.6: Illustration of Ultrasonic Probe and Velocimeter in an LH_2 Tank

Signal Processing in Ultrasonic Level Measurement

To accurately measure the LH_2 level and compensate for the challenges of thermal stratification and sloshing, the system requires a highly capable signal processing unit. The signal processing unit typically consists of advanced software and hardware components designed to dynamically calibrate signal strength, pulse duration, and real-time processing of measured data.

The basic method of detecting the interface between fluids using an ultrasonic level sensor is illustrated in Figure 3.7. Through processor control, the piezoelectric crystal of the transducer is excited with a specific amplitude and duration. This involves applying an AC voltage pulse, which causes the crystal to resonate and transmit an ultrasonic signal. The excitation frequency is chosen to match the resonant frequency of the crystal.

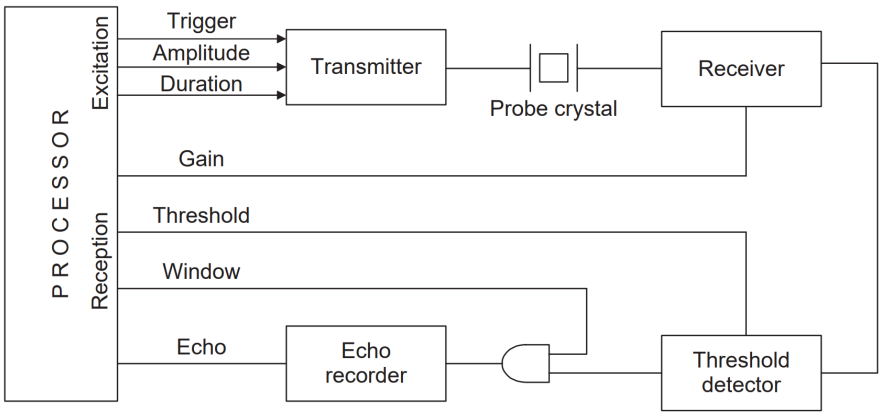

Figure 3.7: Signal Processing Method for the Ultrasonic Transducer(13)

The transmitted ultrasound signal reflects the Liquid gas interface level. The reflected echo is received back by the same crystal, now acting as a receiver. Upon reception, the reflected signal is amplified to enhance its strength as required. Subsequently, the signal passes through a threshold detector to eliminate unwanted noise.

The refined signal is then gated using a timing window, ensuring that only echoes within the target region are recorded. These echoes are stored in memory for subsequent processing and analysis by the processor. This system architecture ensures precise and reliable measurement of the LH_2 level, even under complex conditions such as thermal stratification and sloshing(13).

Typical Design of an Ultrasonic Probe

The typical design of an ultrasonic probe is shown in Figure 3.8. It generally consists of an ultrasound transducer, which is housed within a protective assembly featuring a bubble baffle and a Stillwell. The design of a velocimeter is similar to that of an ultrasonic probe but includes a reflector positioned at a known height. The reflectors must be arranged non-linearly to prevent secondary reflections from a lower reflector from being mistaken for primary reflections from an upper reflector. This design consideration helps to improve the reliability of speed of sound in LH_2 measurements and ensures accurate compensation for the effects of thermal stratification. This reflector allows the velocimeter to measure the speed of sound in the liquid with high precision by timing the reflected signals over a fixed distance.

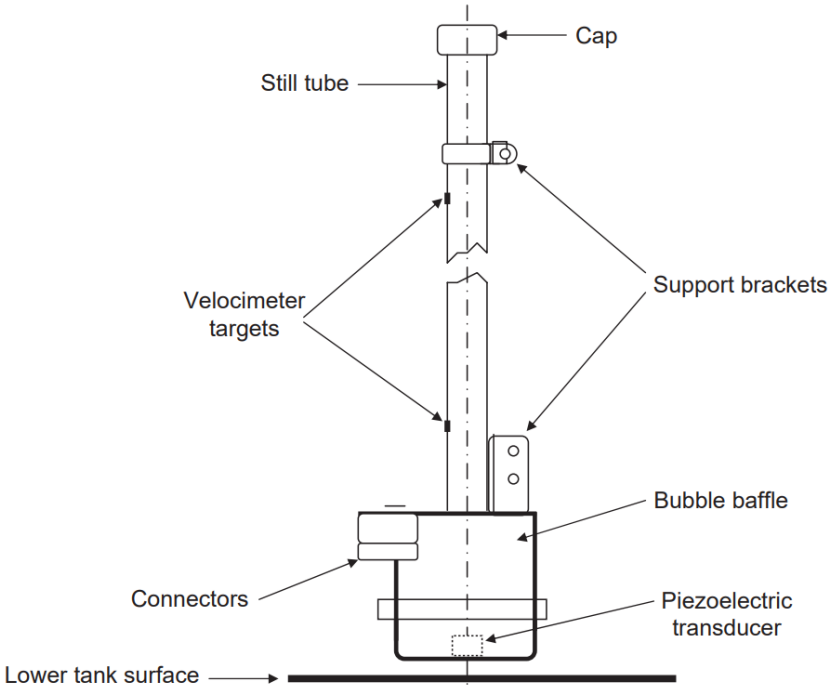

Figure 3.8: Typical Design of an Ultrasonic Probe with Bubble Baffle and Stillwell(13)

This design ensures accurate and reliable measurement performance even in challenging environments such as cryogenic LH_2 tanks, where factors like turbulence and thermal stratification must be accounted for.

Bubble Baffle

Bubbles and boil-off gas within the LH_2 can cause premature reflections of the ultrasonic signal back to the transducer, resulting in incorrect level measurements. This effect can be minimized by using bubble baffles, which are installed around the lower portion of the Stillwell or the probe, as shown in Figure 3.8. These baffles are typically constructed from concentric sleeves with offset interconnecting holes. This structure allows the liquid to enter Stillwell while providing a path that traps or redirects bubbles and boil-off gas away from the entry point, thereby minimizing interference and improving measurement accuracy(48).

Stillwell

The primary purpose of the Stillwell is to both collimate the sound generated and received by the transducer and provide a sheltered area for accurate measurement. The Stillwell protects the measurement process from major phenomena such as sloshing and the entry of large bubbles within the measurement area. The design of the transducer assembly should allow the LH_2 within the Stillwell to follow the level changes of the surrounding liquid, ensuring accurate tracking of the overall tank level.

To avoid hydrogen embrittlement, the Stillwell must be made of a material capable of withstanding this phenomenon, while also being lightweight to minimize the weight of the overall assembly of the ultrasonic probe. Furthermore, the Stillwell should be uniformly coated or lined with an acoustically suitable material to minimize ultrasound reflections within the Stillwell, thereby improving the accuracy and reliability of level measurements(13).

4 Numerical Modelling of Ultrasonic Measurement System in COMSOL

Building upon the theoretical concepts presented in Chapter 3, a simplified ultrasonic sensor was numerically designed using COMSOL Multiphysics 6.2. The reference for the model was taken from (49). This chapter provides a comprehensive overview of the numerical modeling process for the ultrasonic measurement system for liquid hydrogen tanks, detailing each step from preprocessing to post-processing.

4.1 Conceptual Design of the Ultrasonic Measurement System

The conceptual model of the ultrasound system, adapted in COMSOL Multiphysics, is shown in Figure 4.1. This model represents a column of LH_2 with a height that is parameterized to account for varying hydrogen levels in the tank. The interface between gaseous hydrogen and LH_2 is also parameterized to consider changes in the angle of the interface caused by aircraft movements, including roll and pitch angles.

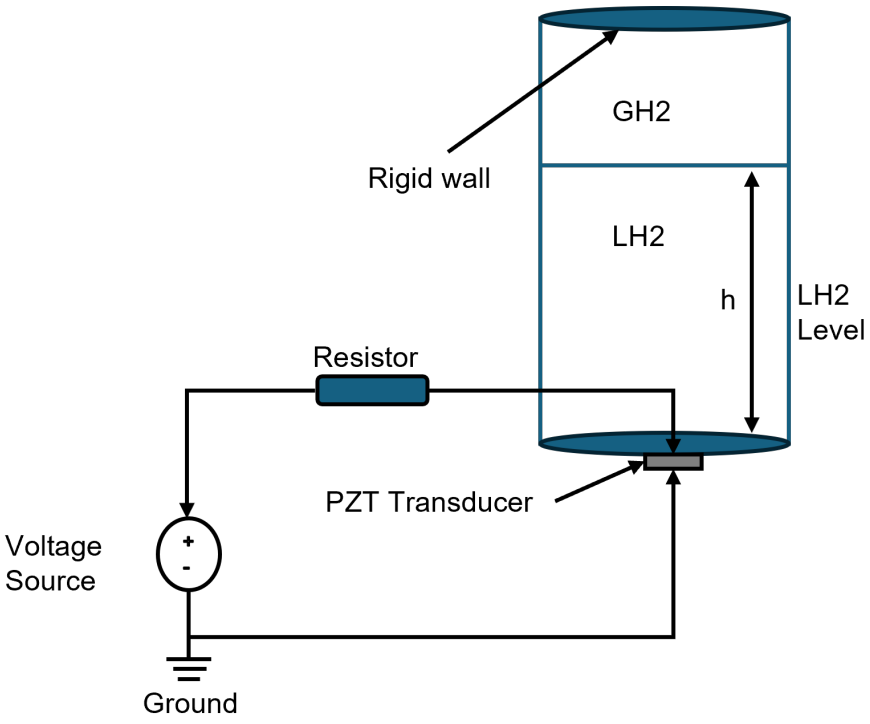

Figure 4.1: Design of Simulation setup

A simplified circuit is employed to excite the PZT-5H material using a Gaussian-modulated signal pulse with a duration of $60\,\mu$s. The excitation signal is represented by the Gaussian-modulated voltage pulse $V(t)$, as defined by the following equation (4.1). The corresponding signal is illustrated in Figure 4.2.

$$V(t) = V_0 \cdot \exp\left(-\left(\frac{t - 1.5T_0}{T_0/2}\right)^2\right) \cdot \sin(2\pi f_0 t) \tag{4.1}$$

The parameter V_0 represents the amplitude of the input signal voltage. The parameter f_0 denotes the frequency of the sinusoidal wave, while T_0 corresponds to its period, given by $T_0 = \frac{1}{f_0}$. The sinusoidal component, $\sin(2\pi f_0 t)$, oscillates at the frequency f_0.

Parameter	Value
V_0	$15\,\mathrm{V}$
f_0	$50\,\mathrm{kHz}$
T_0	$60\,\mu\mathrm{s}$
R	$1000\,\Omega$

Table 4.1: Parameters used in Excitation Signal

With the parameters used in Table (4.1), the energy in the circuit is calculated to be $0.0135\,\mathrm{mJ}$. This energy is less than the ignition energy threshold of LH_2, which is $0.017\,\mathrm{mJ}$.

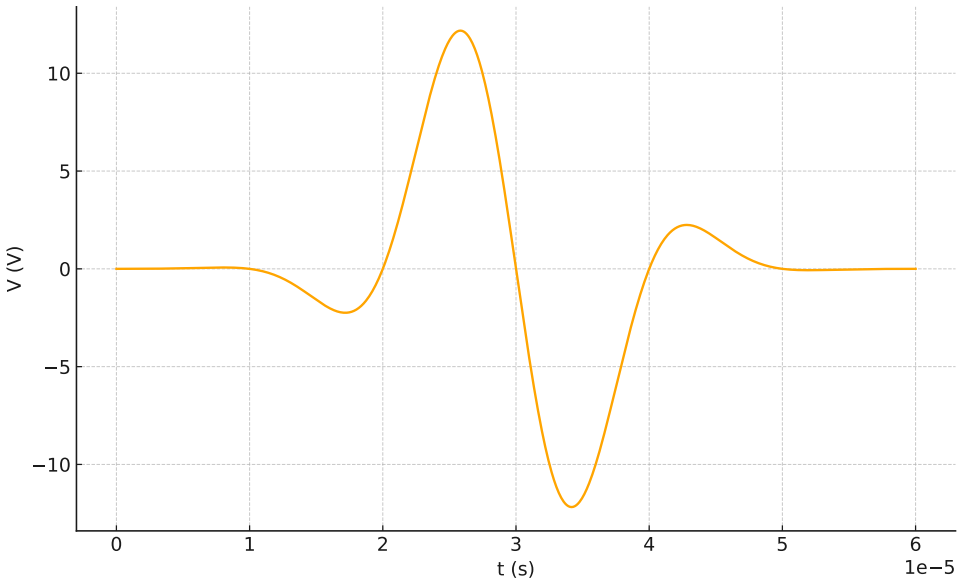

Figure 4.2: Excitation Signal used in simulation to produce Ultrasound

Model Assumptions

To simplify the model and focus on key acoustic interactions, the following assumptions were made:

- **Infinite Horizontal Acoustic Propagation:** Acoustic waves were assumed to propagate infinitely in the horizontal direction, with no reflection from the tank boundaries except from the boundary directly above the GH_2 medium in the column.
- **Absence of Bubbles and Boil-Off Gas:** The model assumed a pure LH_2 medium without entrained gas bubbles or boil-off gas, and no phase transition allowed during ultrasound sensor operation, ensuring a stable acoustic propagation environment without discontinuities.
- **No Initial Acoustic Pressure:** Initially, the system was assumed to be acoustically quiescent, with zero pre-existing acoustic pressure within the medium, allowing the simulation to focus solely on the acoustic waves generated by the ultrasound sensor.
- **Thermal Stability with No Gradients:** A thermally stable system was assumed, with no thermal gradients within the fluid, eliminating temperature-related variations in acoustic properties.
- **Stationary Fluid Assumption:** The fluid was assumed to be stationary, with no fluid dynamics or motion coupled to the acoustic model, simplifying the system by excluding variables related to fluid movement.
- **Neglect of Bulk Viscosity:** Bulk viscosity effects were not included in the model, removing their contribution to the attenuation or dissipation of acoustic waves.
- **Constant Ullage Gas Temperature and Pressure:** The temperature of the ullage GH_2 gas was held constant at 22 K, and the pressure was maintained at 1.5 bar, ensuring a stable acoustic environment.

4.2 Model Definition

The geometrical parameters used in the model to simulate the ultrasound sensor are presented here. The 2D-Axis symmetry approach is chosen to model the varying levels of LH2 effectively, and the 2D approach is Chosen for the unsymmetrical sloshing behaviour caused by changes in roll and pitch angles.

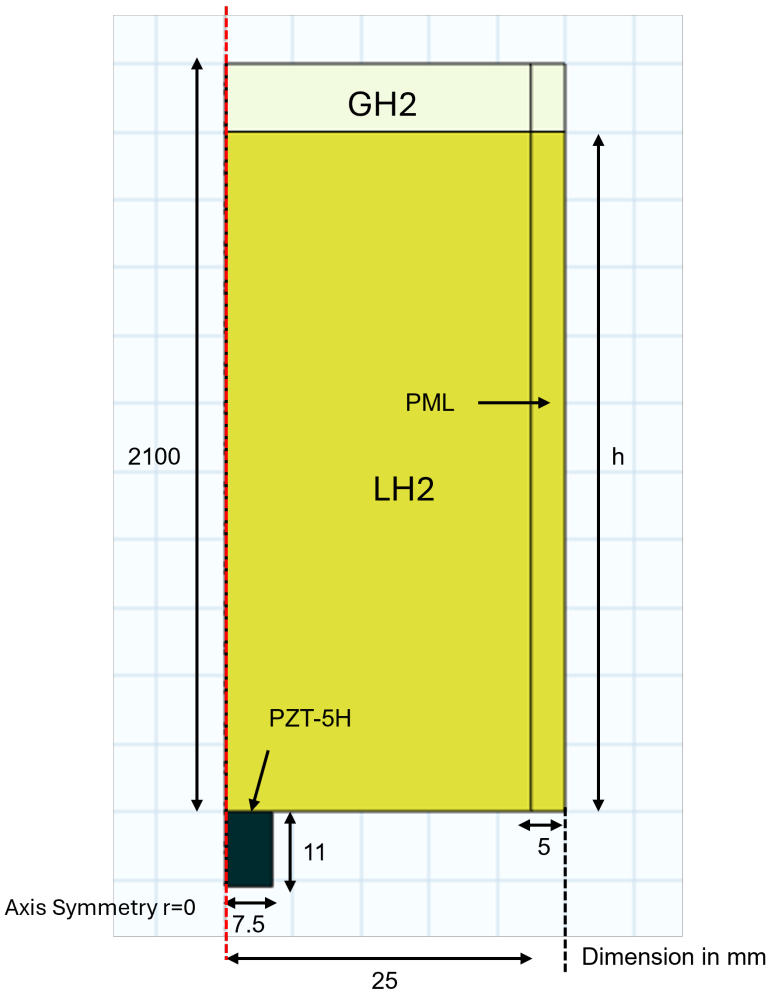

Figure 4.3: Geometry of the Simulation Model

The geometry, shown in Figure 4.3, is kept simple for clarity. A small rectangle in the model represents the PZT-5H material, which acts as the ultrasound transducer.The boundary interface between LH_2 and GH_2 is marked by a horizontal line and represented by different colours. For the 2D model, the horizontal dimensions were doubled to ensure adequate spatial representation, and the interface between LH_2 and GH_2 was parameterized to accommodate varying angles. This parameterization allows the model to simulate different interface inclinations, enabling system performance analysis under varying operational conditions.

Material Properties

The material properties presented in Table (4.2) were sourced from (21), for Para LH_2 at a pressure of 1.5 bar and a temperature of 20 K, which are the operating conditions of the LH_2 tank used in aircraft, as described in Chapter 2.

Property	Value
μ (Dynamic viscosity)	1.3536×10^{-5} Pa · s
ρ (Density)	$71.1714\,\text{kg/m}^3$
k (Thermal conductivity)	$0.09859\,\text{W/(m} \cdot \text{K)}$
c (Speed of sound)	1097 m/s
C_p (Heat capacity at constant pressure)	$9.50\,\text{J/(kg} \cdot \text{K)}$
γ (Ratio of specific heats)	1.65505

Table 4.2: Material Properties for LH_2 at 1.5 bar and 20 K

For GH_2, a temperature slightly above the boiling point at 1.5 bar, specifically 22 K has been selected. All necessary material properties are presented in the Table (4.3) below.

Property	Value
μ (Dynamic viscosity)	1.234×10^{-6} Pa · s
ρ (Density)	$1.8757\,\text{kg/m}^3$
k (Thermal conductivity)	$0.01879\,\text{W/(m} \cdot \text{K)}$
c (Speed of sound)	366 m/s
C_p (Heat capacity at constant pressure)	$12.67\,\text{J/(kg} \cdot \text{K)}$
γ (Ratio of specific heats)	1.9343

Table 4.3: Material Properties of GH_2 at 1.5 bar and 22 K

The bulk viscosity values for both liquid hydrogen (LH_2) and gaseous hydrogen (GH_2) are not available in the current literature. Bulk viscosity plays a significant role in accurately simulating the attenuation of ultrasound waves within these media. Nevertheless, as shown in Equation (3.16), the theoretical model for sound attenuation in LH_2 does not incorporate a term for bulk viscosity. Due to this limitation, and in the absence of empirical data, a bulk viscosity value of zero is adopted for this simulation.

This assumption enables the continuation of the model while acknowledging that the exclusion of bulk viscosity may result in a minor underestimation of attenuation effects, which is further discussed in the context of simulation accuracy in later sections.

A density of 7500 kg/m^3 and a speed of sound of 4580 m/s are assigned to Piezoelectric material PZT-5H. The elasticity matrix, coupling matrix, and relative permittivity values for PZT-5H are also sourced from the built-in material library in COMSOL Multiphysics.

Physics

To accurately simulate both the direct and inverse piezoelectric effects within the PZT domain, the Solid Mechanics and Electrostatics physics interfaces were employed. To facilitate the transducer's dual role as both transmitter and receiver, the Terminal feature in the Electrostatics interface was used, which connects the transducer to an external electrical circuit interface. This configuration as shown in Figure 4.4 mirrors real-life applications where a piezoelectric layer is connected between electrodes to a circuit for excitation and signal detection. The Electrical Circuit interface then drives the transducer with an excitation pulse shown in the Equation (4.1).

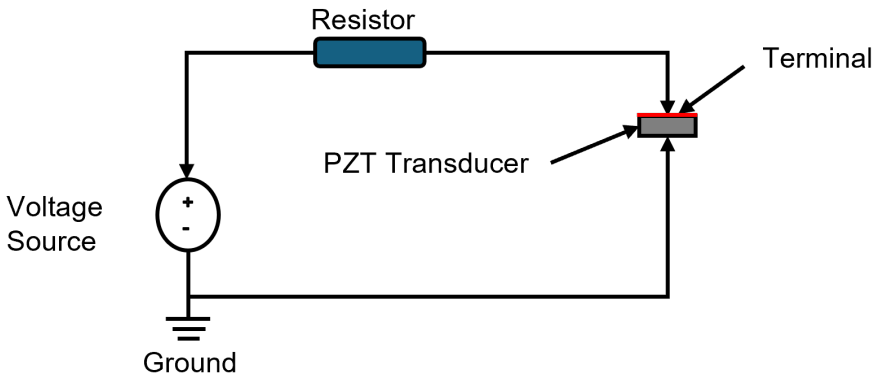

Figure 4.4: Illustration of Electrical Circuit Used in Simulation

To simulate ultrasound wave propagation within the fluid domain and measure the time-of-flight, the Pressure Acoustics, Transient interface was applied. This interface models dynamic pressure variations in both LH_2 and gaseous hydrogen GH_2 domains, representing ultrasound waves. The reference sound pressure level was set to 1 µPa, following standard practices (10).

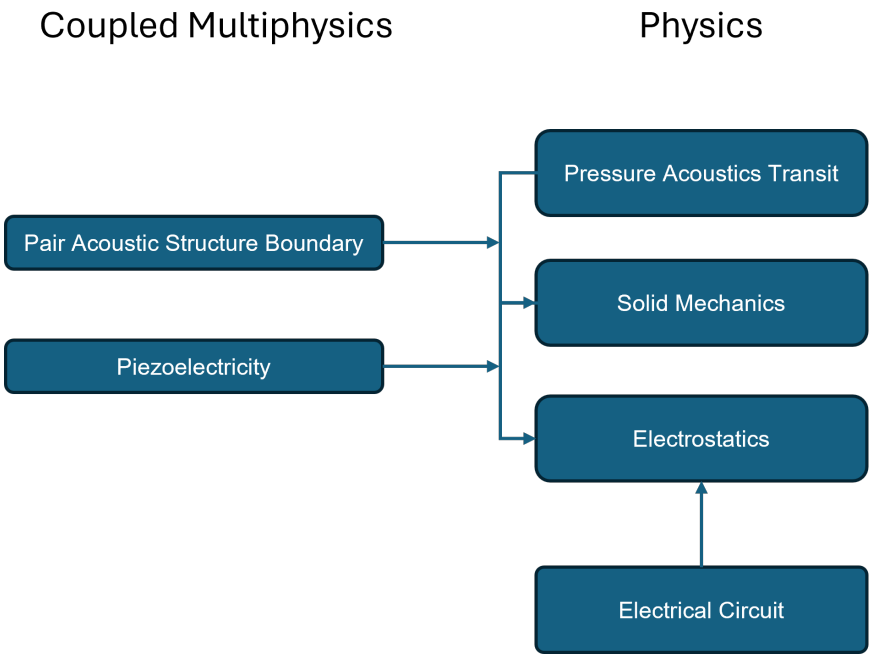

Figure 4.5: Physics and Coupled multiphysics in Model

After defining each physics, the paired Acoustic-Structure Interaction multiphysics interface was used to couple the fluid and solid domains. The graphical representation of used Physics and multiphysics Coupling is shown in Figure 4.5. This interface enables the fluid's acoustics pressure variations to exert forces on the transducer's solid structure, inducing deformations ensures that acoustic pressure loads are transferred accurately between the fluid and solid domains(40).

The Piezoelectricity multiphysics interface was employed to couple the electrostatics and Solid Mechanics interfaces in the PZT-5H domain. This interface models the piezoelectric effect, which couples mechanical stress with electric displacement, enabling the transducer to generate an electric signal in response to mechanical deformation and to deform in response to an applied electric field(40). Through these coupled interfaces,

which link acoustic, structural, and piezoelectric behaviours, a physics setup for the simulation of the ultrasound measurement system is achieved.

4.3 Boundary Conditions

After assigning the physics, different boundary conditions were applied in each physics module to accurately model the ultrasound propagation in the fluid.

Boundary Conditions in the Pressure Acoustics, Transient Interface

In the Pressure Acoustics Transient interface, the boundary conditions shown in Figure 4.6 were applied to accurately simulate sound wave propagation. The fluid models for thermally conducting and viscous fluids were selected in both the LH_2 and GH_2 domains to account for energy dissipation within the fluid. This approach effectively captured both thermal and viscous losses, as outlined in Chapter 3.2.

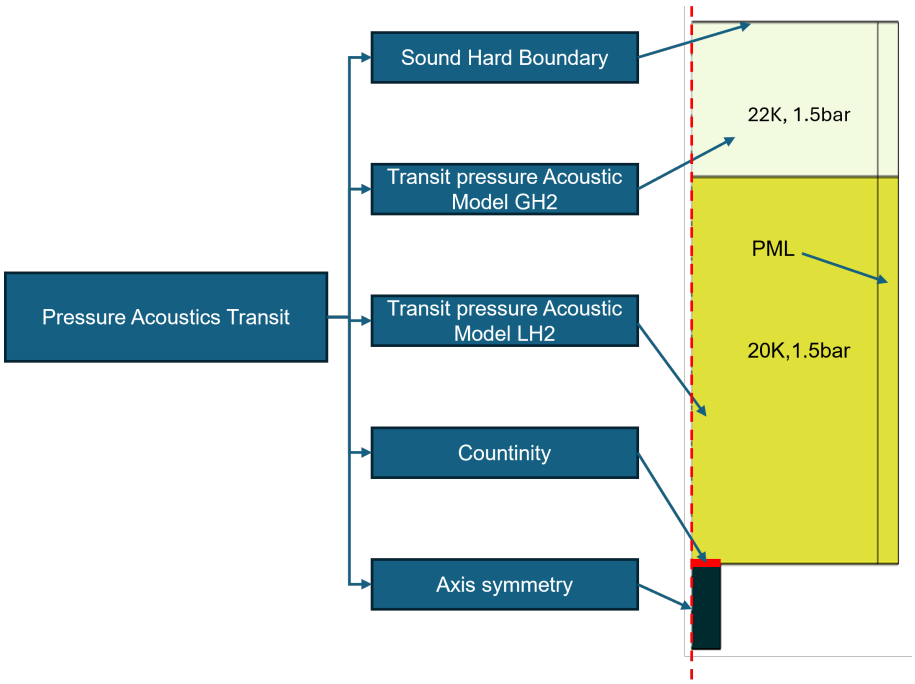

Figure 4.6: Boundary Condition in the Pressure Acoustics transit

- **Sound Hard Boundary:** This boundary condition was applied at the end of the column, simulating the behaviour of a rigid wall in a cryogenic tank.
- **Perfectly Matched Layer (PML):** The PML boundary was placed along the side edges of the simulation domain to absorb outgoing acoustic waves, preventing

reflections back into the main simulation area and ensuring clean wave propagation without interference. To accurately model the simulation, two different PMLs were applied for GH_2 and LH_2, as the speed of sound differed in these domains.

In the 2D axisymmetric model, a cylindrical-type PML was assigned, whereas a Cartesian-type PML was used for the 2D model. The PML was positioned beyond the wavelength of the acoustic wave at 50 kHz to accurately simulate ultrasound propagation. This setup effectively simulated not only 50 kHz but also higher frequencies. The thickness of the PML was chosen to be 5 mm, which was larger than the minimum required value of 1.38 mm in the LH_2 domain, ensuring proper absorption of acoustic waves and avoiding reflection back into the LH_2 domain. This design minimized interference and noise (40).

- **Continuity Boundary:** A continuity boundary was assigned at the interface between the PZT domain and the LH_2 domain. This boundary condition allowed sound waves to propagate smoothly from the PZT material into the LH_2 domain, maintaining continuity in pressure and particle velocity. It accurately modelled the seamless transmission of acoustic waves from the PZT domain to the LH_2 domain.

Solid Mechanics Interface Boundary Conditions

The boundary condition applied in the Solid Mechanics physics interface is shown in the figure(4.7).

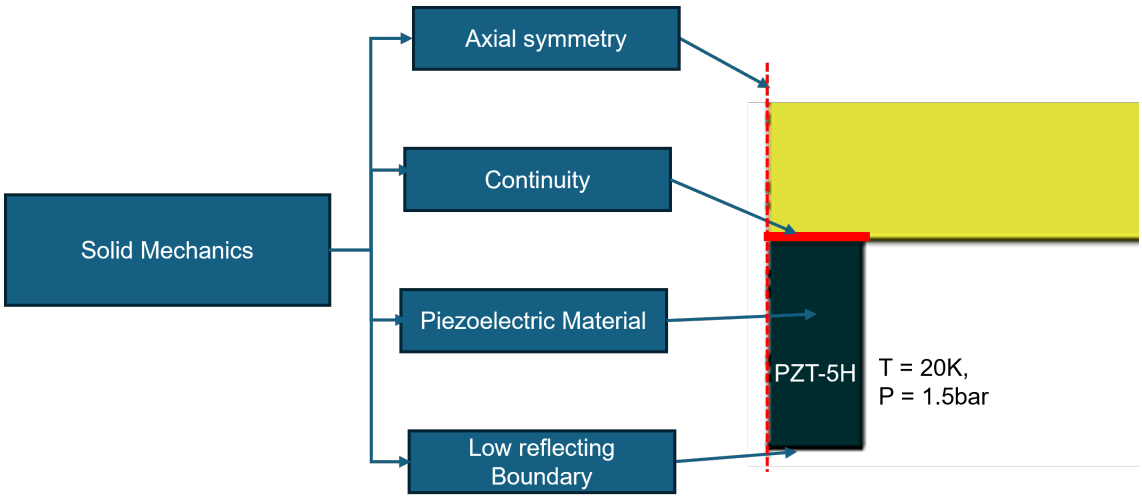

Figure 4.7: Boundary Condition in Solid Mechanics Interface

- **Continuity Boundary Condition:** Similar to the Pressure Acoustics Transient interface, this boundary was applied at the interface between the PZT material and the LH_2 domain to ensure smooth and continuous wave transmission.
- **Low-Reflecting Boundary Condition:** This condition was assigned to the non-contacting boundary opposite the continuity boundary, allowing waves to pass out of the model without reflecting into the PZT domain. It simulated a boundary with perfect impedance, effectively minimizing reflections and preventing unwanted ringing effects, as described in Section 3.2.
- **Piezoelectric Material Property:** To accurately capture the transducer's piezoelectric behaviour, the Piezoelectric Material property was selected for the PZT domain, overriding the default linear elastic material properties.

Boundary Conditions in the Electrostatics Interface

Similar to the other two physics interfaces, the following boundary conditions, shown in Figure 4.8 below, were applied in the Electrostatics physics interface:

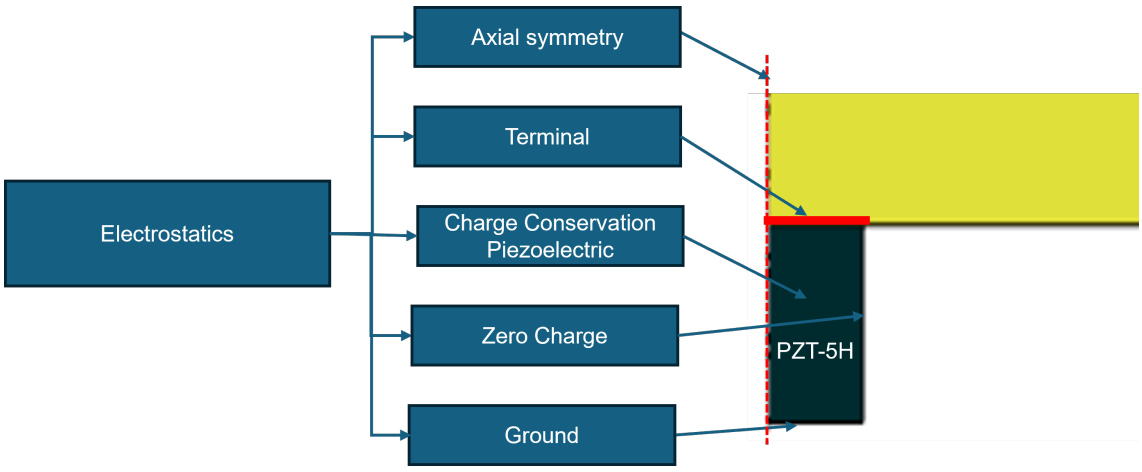

Figure 4.8: Boundary Condition in the Electrostatics Interface

- **Charge Conservation, Piezoelectric:** To achieve accurate piezoelectric behaviour, the charge conservation model was overridden by the piezoelectric charge conversion boundary condition. This implementation ensured proper electromechanical coupling within the PZT material.

- **Ground:** The Ground boundary condition was applied to the lower electrode of the PZT, setting its electric potential to zero volts. This boundary condition provided a stable ground for the transducer's electrical circuit.
- **Terminal:** The Terminal boundary condition was applied to the upper electrode of the PZT and was set to circuit mode, as shown in Figure 4.4, allowing direct interfacing with the external electrical circuit in the Electrical Circuit interface. This boundary enabled the transducer to receive excitation from a voltage source and to respond dynamically.

Boundary Condition Electrical Circuit Interface

As shown in Figure 4.4 and using the parameters listed in Table (4.1), the circuit was constructed using the following boundary conditions. Nodes 0, 1, and 2 were defined to create the circuit for each boundary condition:

- **Ground Node:** To provide the reference potential for the entire circuit, the potential at Node 0 was set to 0 volts. This stable reference ensured accurate voltage measurements across other components in the circuit, such as the PZT and resistor.
- **Voltage Source V1:** A voltage source was placed between Nodes 0 and 1 to apply the excitation voltage to the PZT. A sine wave was selected as the input signal, with its frequency chosen to match the operating frequency of the ultrasound sensor. This sine wave was modulated with a Gaussian envelope function, as given in Equation(4.1). The voltage amplitude was set to 15 V for a duration of 60 microseconds.
- **Resistor:** A 1000-ohm resistor was added to the circuit between Nodes 1 and 2 to control the current flow and simulate realistic circuit behaviour.
- **Electrical T-Terminal:** The external I-terminal node was connected directly to the terminal boundary condition of the PZT in the Electrostatics interface at Node 2. Using this boundary condition, the node allowed the current and voltage in the circuit to interact directly with the piezoelectric transducer, driving its mechanical deformation through electrical responses.

4.4 Meshing

Ultrasound waves are characterized by their wavelength, which is defined by Equation (3.23). To ensure that the wave behaviour was accurately captured within the LH_2 and GH_2 domain, the mesh was refined to resolve the wavelength effectively. To represent the wavelength accurately, each mesh element was made significantly smaller. Which was done by defining the maximum frequency f_{max}, which corresponded to the smallest wavelength, λ_{min}, that the mesh needed to resolve. The minimum wavelength was calculated using the following equation:

$$\lambda_{\text{min}} = \frac{c}{f_{\text{max}}} \tag{4.2}$$

where c represents the speed of sound in the medium, and f_{max} the maximum frequency to resolve by mesh(44). To ensure accurate representation of the ultrasound waves, the maximum element size h_{max} was set to approximately $\lambda_{\text{min}}/5$, as defined by the following equation:

$$h_{\text{max}} = \frac{\lambda_{\text{min}}}{5} = \frac{c}{5 f_{\text{max}}} \tag{4.3}$$

In this study, f_{max} was chosen as $2f_0$, where f_0 is the frequency of Ultrasound. A custom user-defined meshing was applied to achieve optimal accuracy. Specifically, a Free Triangular Mesh was used for the LH_2 and GH_2 domains, while a Mapped Mesh was implemented for the PZT domain and in PML regions. The mesh size was parameterized with the settings outlined in Table (4.4), and the resulting mesh structure was illustrated in Figure 4.9.

Parameter	Value
Maximum element size	h_{max}
Minimum element size	0.00135 m
Maximum element growth rate	1.3
Curvature factor	0.2
Resolution of narrow regions	1

Table 4.4: Element Size Parameters for Custom Mesh

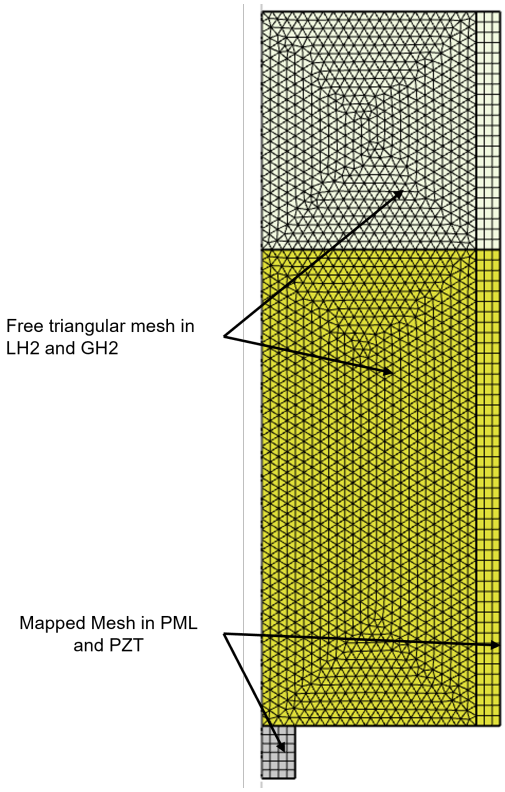

Figure 4.9: Mesh Structure Used in the Model

4.5 Time-Dependent Study and Time-Stepping

To accurately model the system, both meshing and time-stepping needed to be precise. The mesh generated by the above settings provided the spatial resolution required to resolve the wavelength. However, correct time-stepping was essential to complement this spatial setup. A fixed time-stepping method was employed across all three physics interfaces except in electrical circuit interface. The fixed time step, Δt, was calculated based on the Courant–Friedrichs–Lewy (CFL) condition, expressed as:

$$\text{CFL} = \frac{c\Delta t}{h_{\text{max}}} \tag{4.4}$$

where c is the speed of sound in the medium, Δt is the time step, and h_{max} is the maximum mesh element size defined by Equation (4.3). For this model, the CFL number was conservatively set to 0.1, ensuring that the wave propagated through only a small fraction of a mesh element per time step. This approach minimized temporal discretiza-

tion errors while aligning well with the spatial resolution of the mesh. The time step was further defined by:

$$\Delta t = \frac{h_{\text{max}} \cdot \text{CFL}}{c} = \frac{\text{CFL}}{f_{\text{max}} \cdot N} \approx \frac{1}{60 \cdot f_{\text{max}}} \tag{4.5}$$

where N represents the number of elements per wavelength, which was chosen as 6.

To handle time-stepping, the generalized-α method was used, as outlined in the COMSOL User Guide (40). The simulation output time range was defined as:

$$\text{range}(0, T_0/6, \text{ToF} + 150\,\mu\text{s}) \tag{4.6}$$

where T_0 is $60\,\mu$s, the period of the ultrasound source, $T_0/6$ specifies the time increment between output points, and ToF $+ 150\,\mu$s is the total simulation duration. Here, ToF represents the theoretical TOF calculated using Equation (3.2), which was parameterized based on the LH_2 level and the speed of sound in LH_2. An additional offset of $150\,\mu$s was added to the theoretical time to capture the all the reflected acoustic pressure from the interface.

4.6 Post-processing and Validation of the Model

As a standard method for measuring the TOF, the interval from the initial sent pulse to the start of the voltage generated by the reflected acoustic pressure from the interface was measured as shown in the Figure 4.10. For post-processing of the simulation data, the voltage at the terminal of the PZT transducer was measured. The acoustic pressure generated by the transducer in the LH_2 domain and reflected from the interface was measured on the continuity boundary using a point probe.

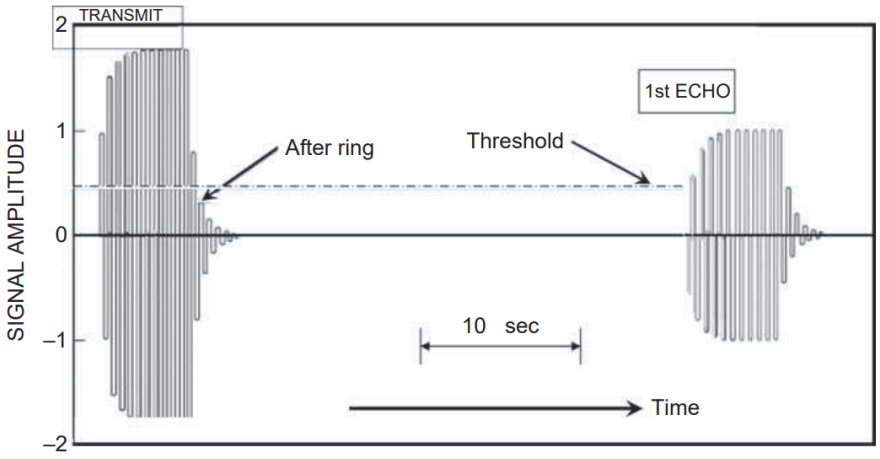

Figure 4.10: TOF measurement method(13)

Post-processing of the simulation data and graph plotting were conducted using Python[1]. To determine the TOF for the ultrasonic wave from the reflected echo, the time corresponding to 5% of the maximum amplitude of the echo voltage was used. The complete code for identifying the TOF is provided in the Appendix (6).

After data post-processing, the validity of the model was conducted by comparing the theoretical TOF for ultrasound wave propagation with the TOF values obtained from the simulation. Simulations were conducted at two different LH_2 temperatures, 20K and 14K, to evaluate the model. The TOF was measured for a 0.75 m LH_2 level at each temperature, with all simulations performed at a frequency of 50 kHz.

The theoretical TOF for each condition was calculated using Equation 3.2. Table 4.5 presents the parameters used in each simulation, including the speed of sound, LH_2 height, and the corresponding theoretical TOF values.

Table 4.5: Simulation Parameters and Theoretical ToF Values

Temperature (K)	Speed of Sound (m/s)	LH_2 Level (m)	Theoretical ToF (ms)
20	1097	0.75	1.3673
14	1257	0.75	1.1933

For the simulation at 20 K and 1.5 bar, the material properties defined in the model corresponded to conditions at 20K. However, for the simulation at 14 K, all the corresponding material properties were sourced from (21)

[1]Programming language

The acoustic pressure emitted from the transducer and received at the continuity boundary is presented in Figure 4.11, for a temperature of 14 K and an LH_2 level of 0.75 m.

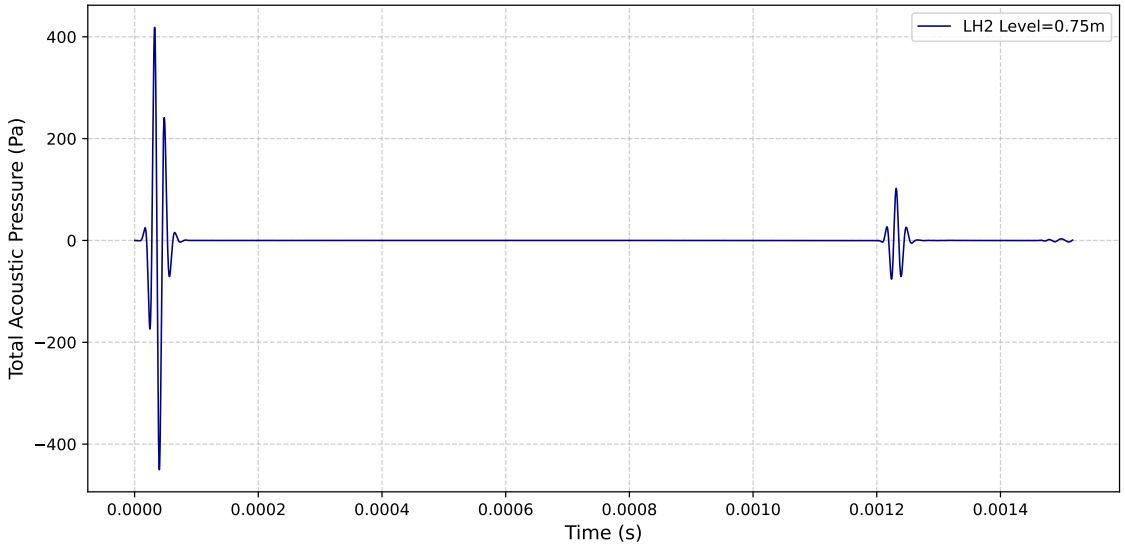

Figure 4.11: Total Acoustic pressure of Transmitted and received Ultrasonic wave at T=14K

The voltage detected in the transducer due to the received acoustic pressure at T=14 K is shown in Figure 4.12. The green line represents the time of flight of the ultrasound wave, while the orange line represents the theoretical.

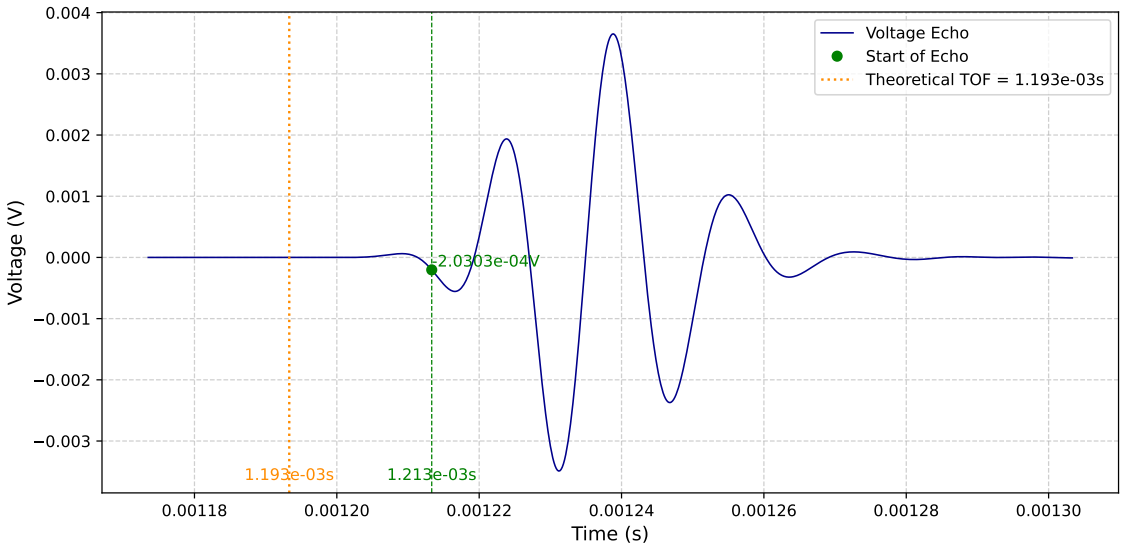

Figure 4.12: Theoretical TOF vs Experimental TOF of Ultrasonic wave at T=14K

Figure 4.13 represents the acoustic pressure transmitted from the transducer at a temperature of 20 K and an LH_2 level of 0.75 m, as well as the acoustic pressure reflected from the interface.

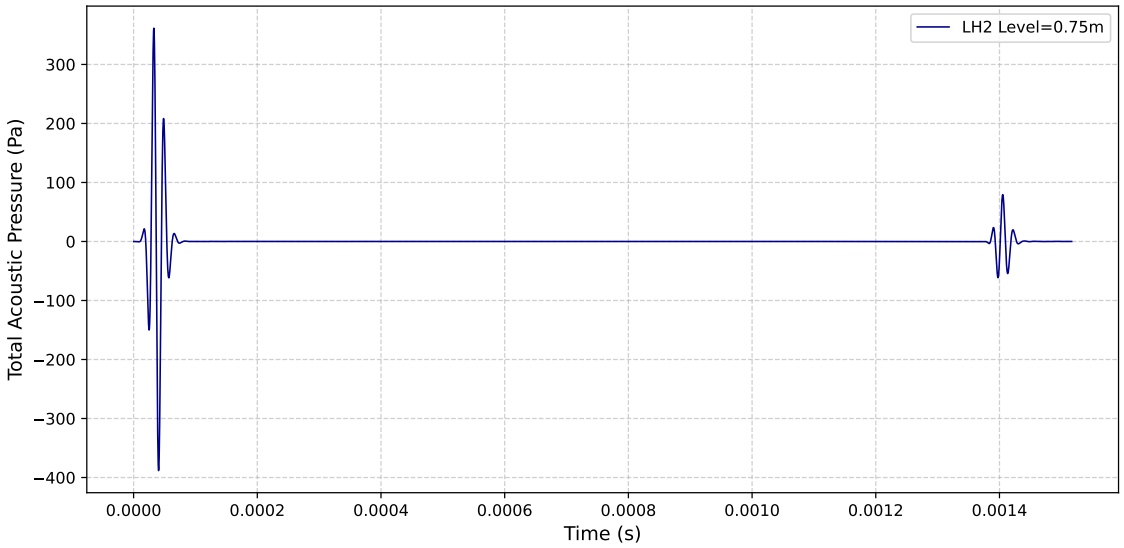

Figure 4.13: Total Acoustic pressure of Transmitted and received Ultrasonic wave at T=20K

The voltage detected in the transducer at 20 K, due to the received echo from the interface, is shown in Figure 4.14 below.

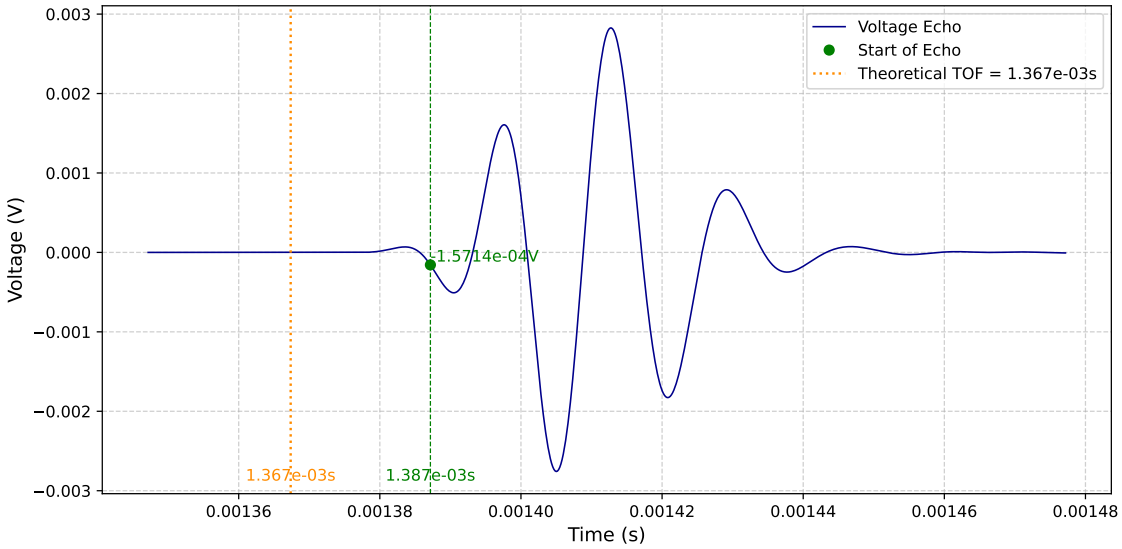

Figure 4.14: Theoretical TOF vs Experimental TOF of Ultrasonic wave at T=20K

The absolute and relative errors presented in Table (4.6) demonstrate the model's accuracy in simulating ultrasound wave propagation within LH_2. With error values consistently below 2% across both temperatures and their corresponding speeds of sound, the model exhibits a high degree of reliability, closely aligning theoretical and simulated TOF values. This consistency validates the model's effectiveness in accurately capturing the acoustic behaviour of LH_2, including the reflection of acoustic waves at the LH_2-GH_2 interface.

Temperature (K)	LH_2 Level (m)	Theoretical ToF (ms)	Simulated ToF (ms)	Absolute Error (ms)	Relative Error (%)
20	0.75	1.3673	1.3871	0.0198	1.44
14	0.75	1.1933	1.213	0.0200	1.67

Table 4.6: Comparison of Simulated and Theoretical TOF Values

5 Results And Findings

Building upon the validation conducted in the previous chapter, several simulation conditions were established to enable precise measurement of LH_2 levels within the tank. As described in Chapter 2.3, the diameter of hydrogen tanks varies across aircraft depending on the diameter of the aft fuselage. For this simulation, a tank diameter of 2.1 meters was selected, which exceeds the required minimum diameter of 1.9 meters for the ATR72 regional aircraft (33). This setup allowed measurements of LH_2 levels ranging from 10% to 90% of the tank's capacity, reflecting typical operational conditions.

5.1 Simulation Parameter

To capture accurate and reliable measurements of LH_2 levels, the following parameters were simulated:

- **Tank Fill Levels:** Measurements were taken with the LH_2 level varying incrementally from 10% to 90% of tank capacity. This range was chosen to assess the model's performance across low, medium, and high fill levels, ensuring for diverse operational scenarios.
- **Frequency analysis:** A frequency of 50 kHz was used in all simulations, except for the frequency analysis section. In this section, the least accurate LH_2 level measurement was re-evaluated at 100 kHz and 125 kHz to analyse the effect of frequency on measurement accuracy.
- **Surface Angle Variations:** The effect of varying surface angles due to sloshing was incorporated into the simulations, corresponding to different phases of flight. Bank angles are limited to 15° during takeoff at speeds of V2[1] + 10 knots to ensure stability and control (50). During holding patterns and cruise, a 30° bank angle

[1]Takeoff Safety Speed

is maintained for passenger safety and comfort. In extreme manoeuvres, bank angles can reach up to 60° for passenger aircraft (51). Simulations were performed at two LH_2 levels (0.5 m and 1.0 m) with bank angles ranging from 0° to 60°. These simulations aimed to evaluate the ultrasonic sensor's accuracy in measuring TOF under varying sloshing conditions.

- **Temperature Variation:** To analyse the effect of temperature variations on acoustic properties, TOF measurements were conducted across a temperature range of 18K to 20K. The least accurate LH_2 level from the primary measurements was selected and re-simulated with the corresponding speed of sound and properties adjusted to account for thermoviscous dissipation effects at 50 kHz.

Time Delay Analysis

The initial TOF was measured from the start of the signal (0 seconds) to the maximum amplitude of the first significant echo, serving as the primary time delay estimate based on the reflection from the LH_2-GH_2 interface. A more accurate method for TOF measurement was employed to calculate the true time delay between the emitted and received signals using cross-correlation[2]. This approach provided precise TOF measurements across all simulations, with the calculated true time used for LH_2 level estimation. The analysis was conducted in Python using the NumPy library, and the corresponding code is provided in Appendix B 6.

5.2 Result

Result for varying LH_2 Level

For each level, Cross-correlation of the signal was performed to identify the true time delay. This process provided a more accurate TOF measurement by isolating the time delay from 0 seconds to the peak of the Cross-correlation function, representing the true TOF. Figure 5.1 illustrates the comparison between theoretical and experimental TOF values for 1.26m, with the direct TOF measurements serving as a preliminary estimate. Figure 5.2 shows the results of the Cross-correlation analysis, where the true TOF for

[2]mathematical tool to determine the time delay between two signals by measuring their similarity at different time shifts

each LH_2 level was identified.Following parameter provided in the Table (5.1) were used for the simulation across 10%-90%.

Parameter	Value	Unit
LH_2 Level	0.21-1.89	m
LH_2 Temperature	20	K
GH_2 Temperature	22	K
Speed of Sound(LH_2)	1097	m/s
Speed of Sound(GH_2)	366	m/s
Voltage	15	V
Frequency	50	kHz

Table 5.1: Simulation Parameters for Varying Surface Level

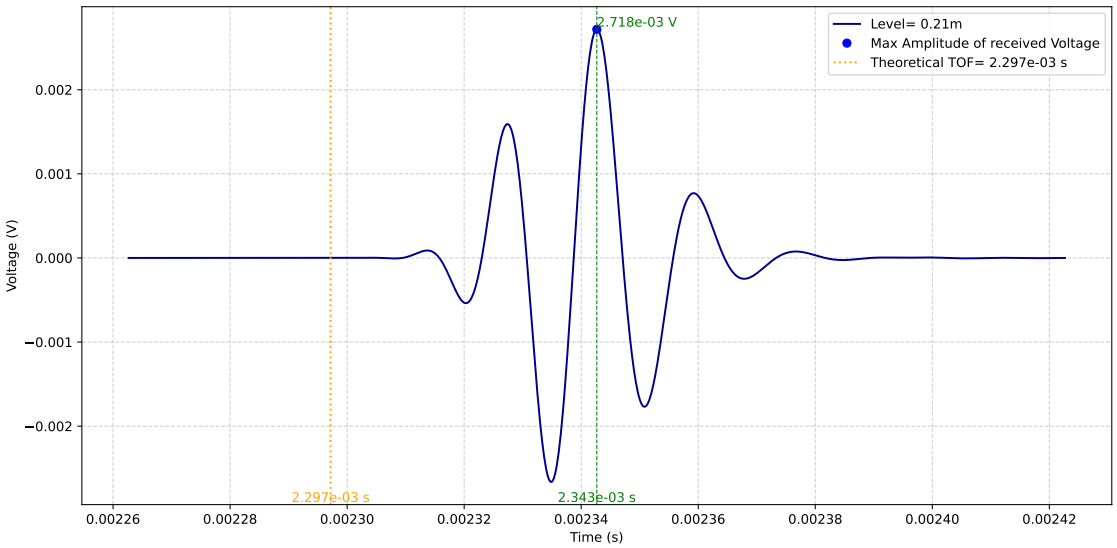

Figure 5.1: Theoretical TOF vs Experimental TOF of Ultrasonic wave at LH_2 level of 1.26m

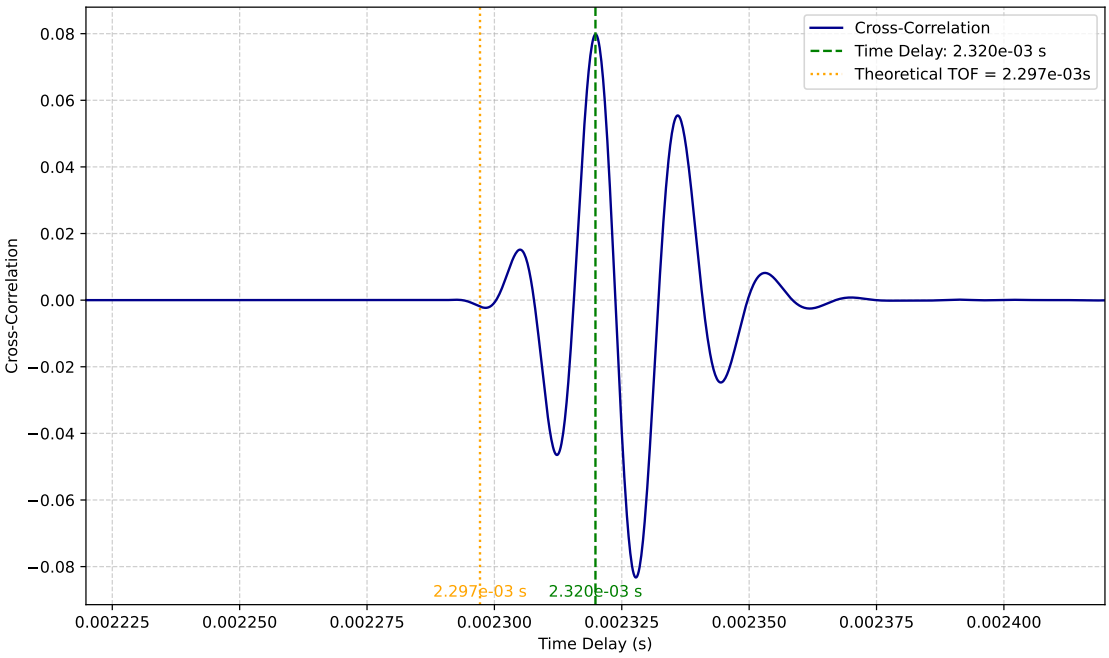

Figure 5.2: True TOF of the Ultrasonic wave at LH_2 level of 1.26m

Using the true TOF values obtained through Cross-correlation, the level of LH_2 in the tank was calculated according to Equation (3.2). Table (5.2) presents the time delay from 0s, the true time delay values in (ms) for each LH_2 level and the maximum amplitude of reflected echo Voltage detected in PZT Transducer.

Table 5.2: Primary and Secondary Time Delay Measurements for Varying LH_2 Levels in a 2.1m Tank

LH_2 Level (%)	Time Delay (ms)	True Time Delay (ms)	Max Amplitude (mV)
10%	0.4282	0.40533	2.9582
20%	0.8110	0.7882	2.9095
30%	1.1940	1.1717	2.8595
40%	1.5768	1.5540	2.8069
50%	1.9598	1.9368	2.7594
60%	2.3427	2.3194	2.7180
70%	2.7256	2.7027	2.6819
80%	3.1085	3.0855	2.6328
90%	3.4915	3.4683	2.5949

Additionally, the Table (5.3) provides the calculated LH_2 level, along with the relative and absolute errors in comparison to the actual LH_2 level.

LH_2 Level (m)	Calculated Height (m)	Relative Error (%)	Absolute Error (mm)
0.21	0.2223	5.85	12.3235
0.42	0.4323	2.92	12.3112
0.63	0.6423	1.95	12.3867
0.84	0.8523	1.46	12.3690
1.05	1.0623	1.17	12.3510
1.26	1.2723	0.97	12.3389
1.47	1.4824	0.84	12.4144
1.68	1.6923	0.73	12.3967
1.89	1.9023	0.65	12.3790

Table 5.3: Calculated Height and Error for varying Level of LH_2

Figure 5.3 presents the absolute error at various levels, with the horizontal line indicating the average absolute error across all measurement levels.

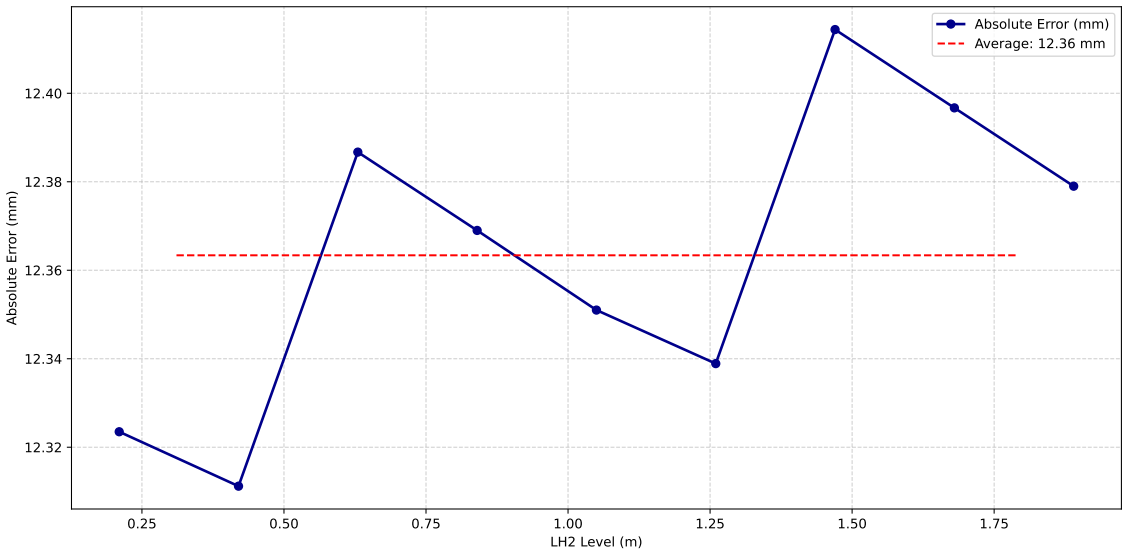

Figure 5.3: Absolute error between 0.21 m and 1.89 m

Result for varying Frequency

From Table (5.3), it is evident that at the 0.21 m level, there is a noticeable relative error in the LH_2 level measurement. To further investigate, simulation results at 50 kHz were compared with those at 100 kHz and 125 kHz to evaluate the effect of frequency on measurement accuracy. Only the frequency parameter was altered and simulation was conducted for only 0.21m, while all other parameters remained consistent with those listed in Table (5.1). All graph below represents the simulation result for 50kHz and 100kHz frequency.

Figure 5.4 presents the results of the acoustic pressure measured at the source for 50kHz and 100kHz frequency. It can be observed that the 50 kHz ultrasound receives a higher acoustic pressure at the source, while the 100 kHz frequency receives a lower acoustic pressure. This effect is directly reflected in the transducer's measured voltage, as shown in Figure 5.5, where the lower-frequency ultrasound wave corresponds to a higher received voltage, while the higher-frequency ultrasound shows a reduced received voltage.

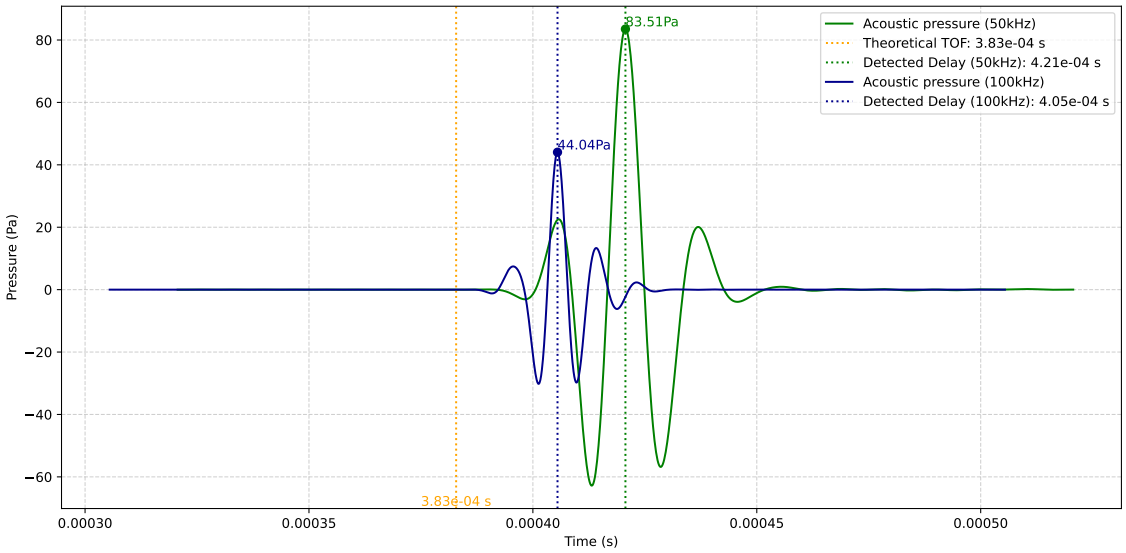

Figure 5.4: Acoustic pressure of the echo at the source for 50 kHz and 100 kHz at LH_2 level of 0.21 m

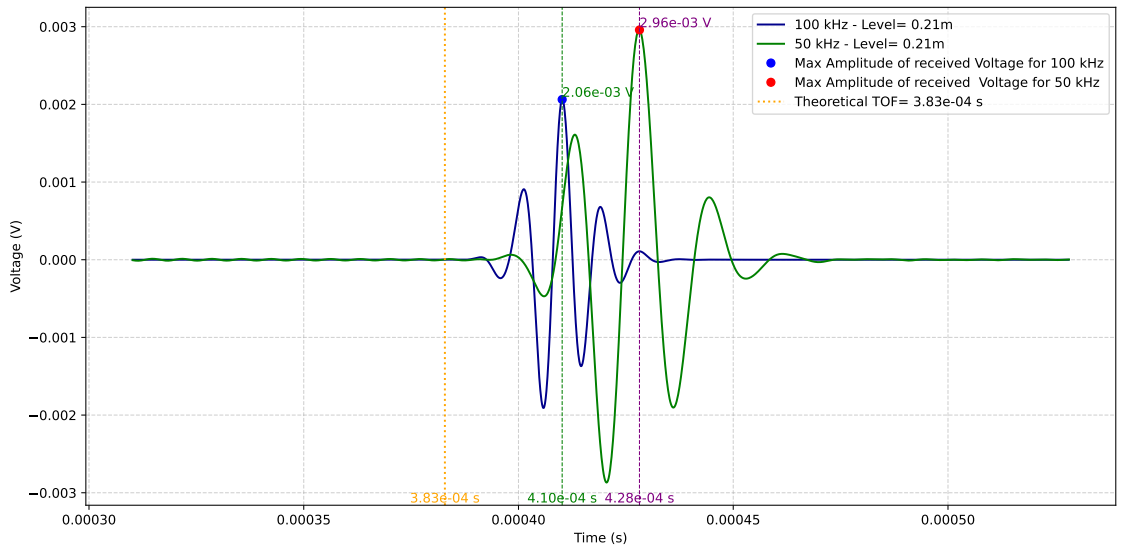

Figure 5.5: Detected echo voltage at the transducer for 50 kHz and 100 kHz frequencies at LH_2 level of 0.21 m

To measure the true time of flight, cross-correlation of the received voltage signal is performed, as shown in Figure 5.6. It can be observed that the 100 kHz frequency exhibits a shorter time delay compared to the 50 kHz frequency. To further analyse the time difference between both frequencies, cross-correlation of the received echo signals is conducted and illustrated in Figure 5.7, highlighting the time delay between the 50 kHz and 100 kHz frequencies.

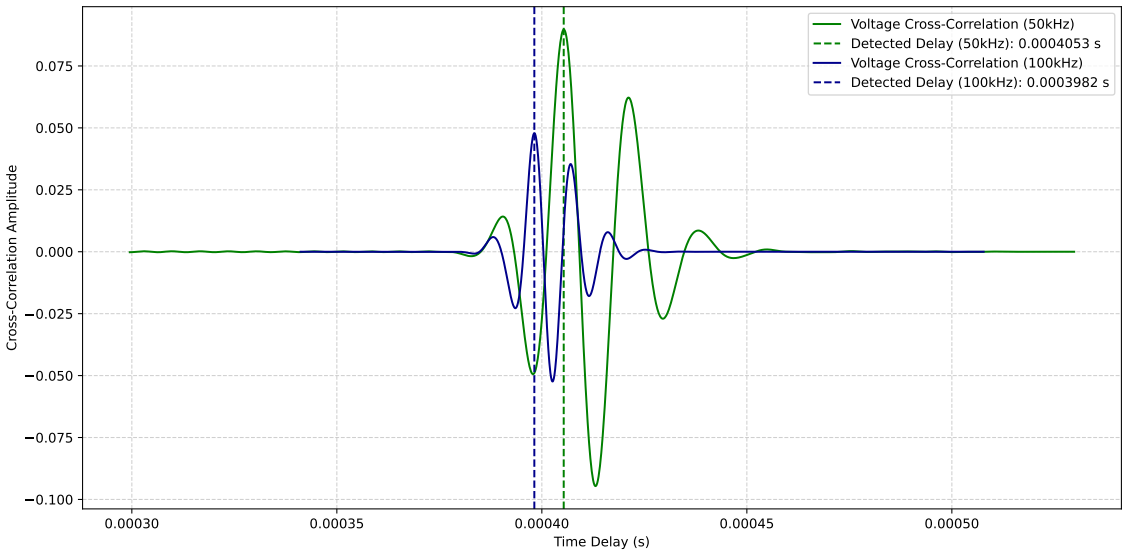

Figure 5.6: True TOF for 50 kHz and 100 kHz Signals at the LH_2 Level of 0.21 m

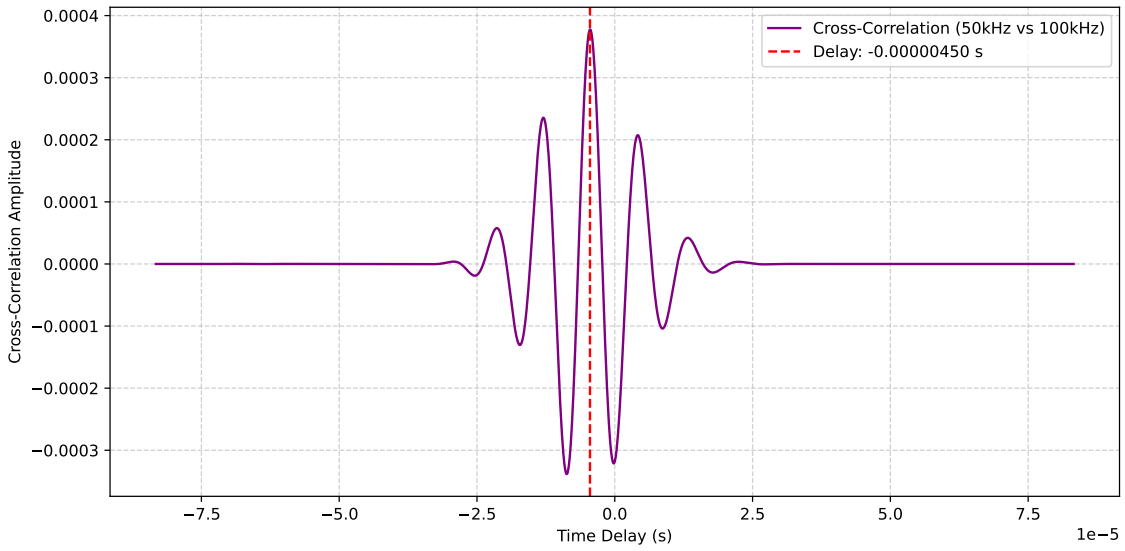

Figure 5.7: Time delay between 50kHz and 100kHz Detected Voltage echo

The effect of frequency on measurement accuracy is presented in the following tables. Table (5.4) provides the values measured from the simulation, while Table (5.5) shows the calculated height corresponding to the true delay measured. Additionally, the Relative and the absolute errors for 50kHz,100kHz and 125kHz frequencies are also compared in the Table (5.5).

Frequency (kHz)	Level (m)	Time Delay (ms)	Max Amplitude (mV)	True Time Delay (ms)
50	0.21	0.4816	2.9580	0.4053
100	0.21	0.4102	2.0627	0.3982
125	0.21	0.4067	1.7601.	0.3966

Table 5.4: True TOF and Maximum Voltage Amplitude at Varying Frequencies

Frequency (kHz)	Level (m)	Calculated Height (m)	Relative Error (%)	Absolute Error (mm)
50	0.21	0.2223	5.85	12.3235
100	0.21	0.2184	3.95	8.4127
125	0.21	0.21753	3.58	7.5351

Table 5.5: Calculated Height and Errors at Varying Frequencies

Result for varying Surface Angle

As described in an earlier chapter, the study investigates unsymmetrical sloshing behaviour using a 2D model, with other parameters held constant as listed in Table (5.1). The results obtained from different LH_2 sloshing angles are analysed here. In Figure 5.8, the acoustic pressure of the reflected echo is shown for sloshing angles of 0°, 15°, 30°, and 45°. Figure 5.9 presents the acoustic pressure received at the source for sloshing angles of 0°, 45°, and 60°. It can be observed that the pressure received from the reflected echoes decreases with increasing surface angle, reaching the lowest value at 60°. All the measurements are done for LH_2 levels of 0.5m and 1m. All graph below represents the simulation result for LH_2 level of 1m.

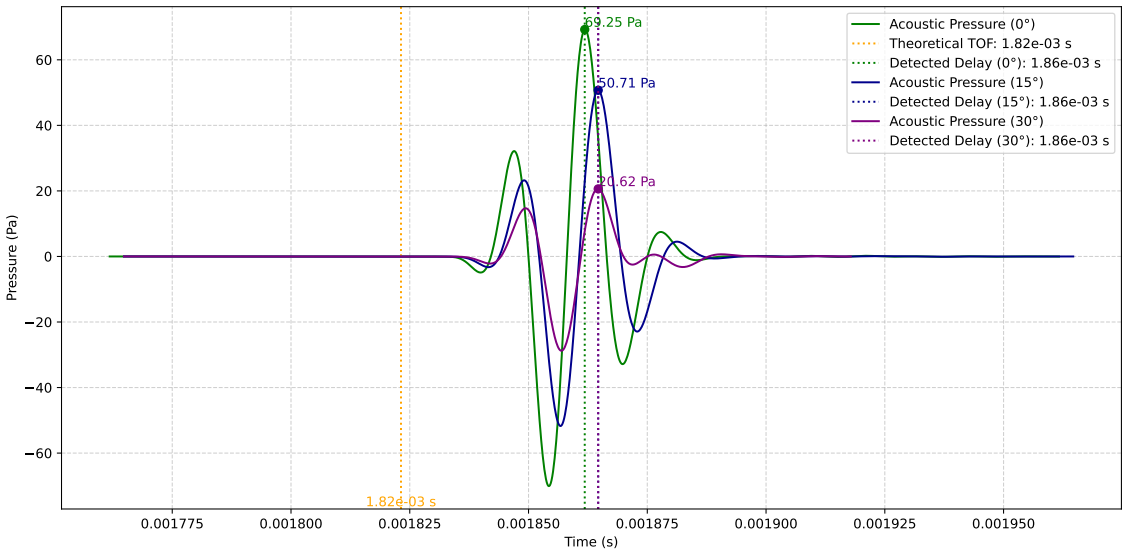

Figure 5.8: Pressure of Reflected Echo at Source for 0°,15°,30° at LH_2 level of 1 m

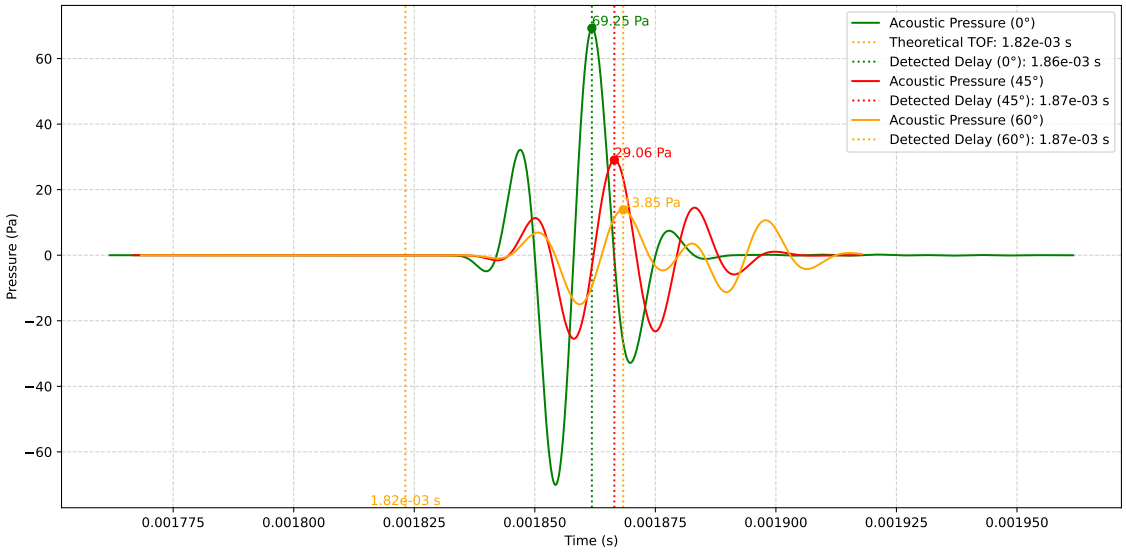

Figure 5.9: Pressure of Reflected Echo at Source for 0°,45°,60° at LH_2 level of 1 m

Figures 5.10 and 5.11 show the voltage received in the transducer for surface angles of 0°, 15°, 30°, and 45° at a level of 1 m, and for angles of 0°, 45°, and 60° at the same level, respectively. It is observed that as the surface angle increases, the acoustic pressure decreases, resulting in correspondingly lower voltages measured in the transducer. This

trend is evident in the maximum amplitude of the voltage, where lower angles yield higher received voltages and higher angles produce lower received voltages.

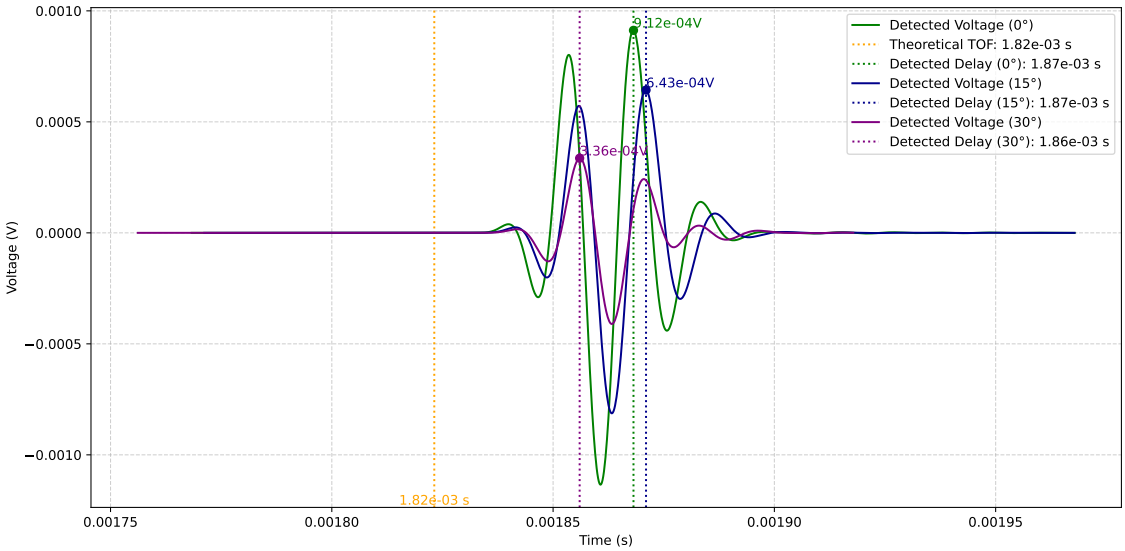

Figure 5.10: Detected Voltage of Reflected Echo at Transducer for 0°,15°,30° at LH_2 level of 1 m

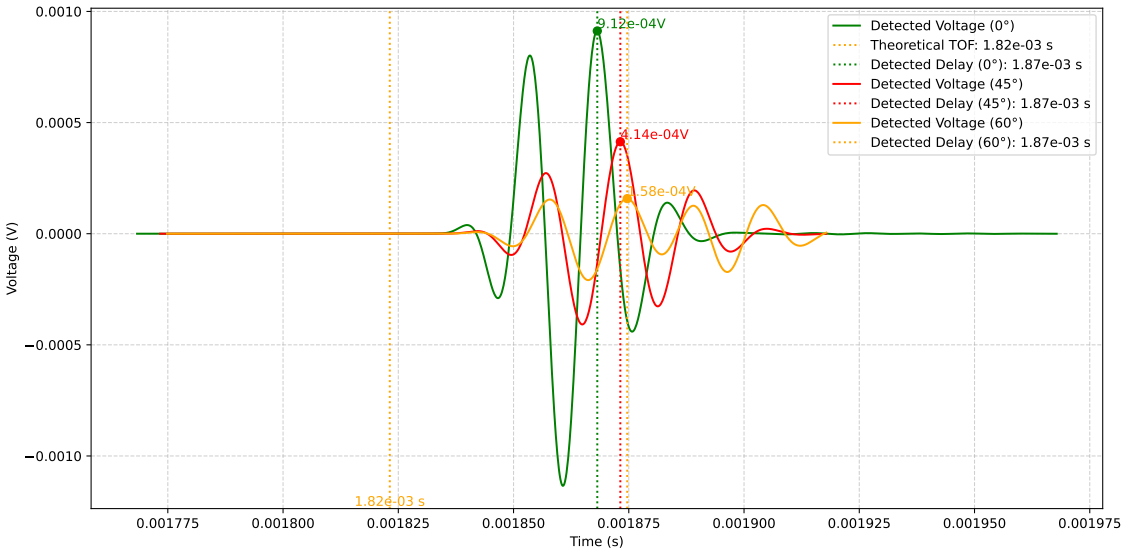

Figure 5.11: Detected Voltage of Reflected Echo at Transducer for 0°,45°,60° at LH_2 level of 1 m

To measure the true time delay between the emitted and received voltages, cross-correlation is performed for each voltage signal, as shown in Figure 5.12 and Figure 5.13. The results indicate that the 45° and 60° angles exhibit larger time delays. To measure the delay cross-correlation of the received voltage signals between 0° and 45° and between 0° and 60° is conducted, with the resulting time lags illustrated in Figure 5.14 and Figure 5.15, respectively.

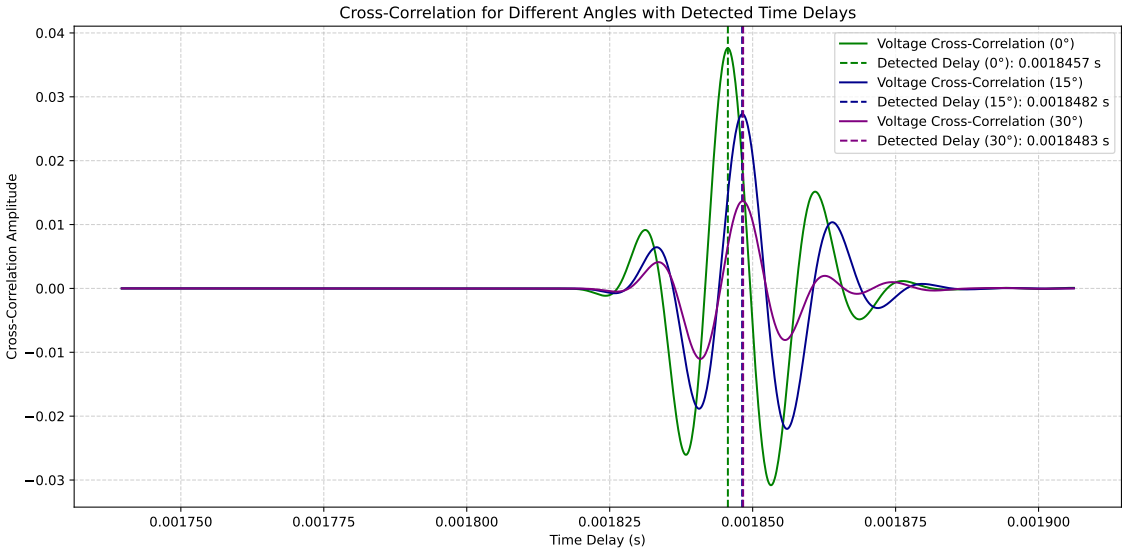

Figure 5.12: True TOF for 0°,15° and 30° at the LH_2 Level of 1 m

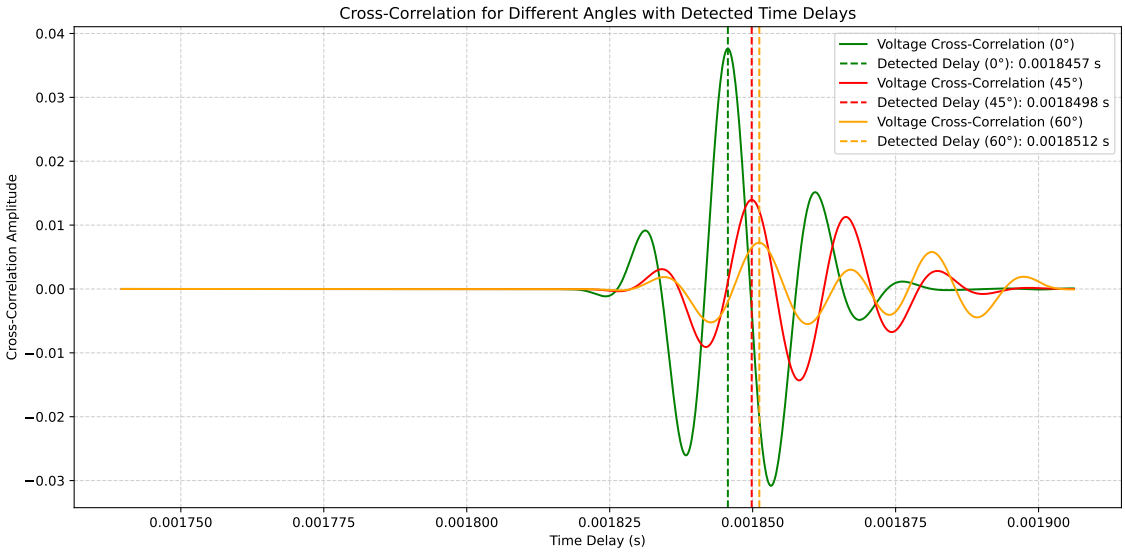

Figure 5.13: True TOF for 0°,45° and 60° at the LH_2 Level of 1 m

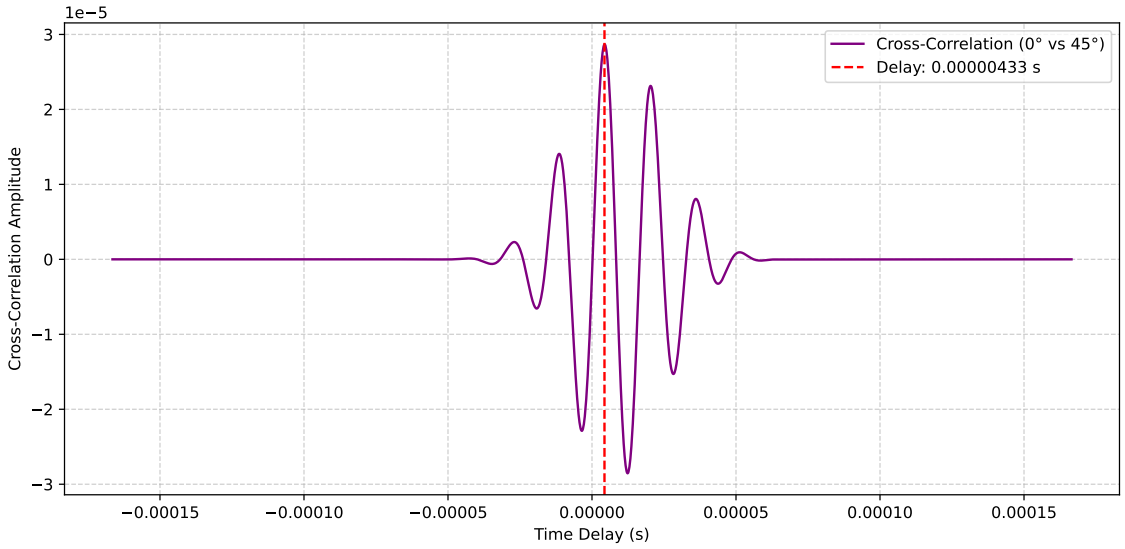

Figure 5.14: Time delay between detected voltage echo at 0° and 45°

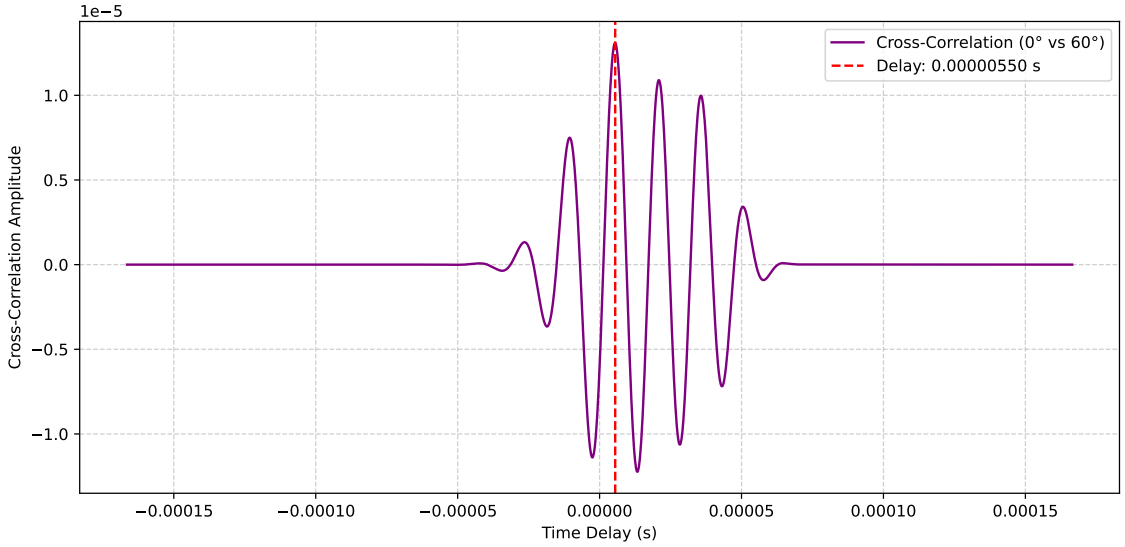

Figure 5.15: Time delay between detected voltage echo at 0° and 60°

Table (5.6) presents the time-of-flight (TOF) measurements from the initial time (0 s) to the maximum amplitude of the received echo voltage (mV) and true TOF from cross-correlation for each sloshing angle in 0.5m and 1m LH_2 Level. In Table (5.7), the true TOF from the simulation is used to calculate the measured height. This calculated height is then compared across all five angles for liquid levels of 0.5 m and 1 m, with both the relative and absolute errors included.

Bank Angle (°)	LH_2 Level (m)	Time Delay (ms)	Max Amplitude (mV)	True Time delay(ms)
0°	0.5	0.9563	0.9360	0.9340
15°	0.5	0.9591	0.6549	0.9365
30°	0.5	0.9443	0.3326	0.9367
45°	0.5	0.9615	0.4143	0.9381
60°	0.5	0.9628	0.1580	0.9393
0°	1.0	1.8680	0.9121	1.8456
15°	1.0	1.8710	0.6432	1.8481
30°	1.0	1.8560	0.3362	1.8483
45°	1.0	1.8731	0.4137	1.8498
60°	1.0	1.8740	0.1578	1.8512

Table 5.6: Primary Results of Time Delay at Varying LH_2 Surface Angles

Bank Angle (°)	LH_2 Level (m)	Calculated Height (m)	Relative Error (%)	Absolute Error (mm)
0°	0.5	0.5129	2.58	12.90
15°	0.5	0.5136	2.72	13.60
30°	0.5	0.5137	2.74	13.70
45°	0.5	0.5145	2.90	14.50
60°	0.5	0.5152	3.04	15.20
0°	1.0	1.0123	1.23	12.30
15°	1.0	1.0137	1.37	13.70
30°	1.0	1.0138	1.38	13.80
45°	1.0	1.0146	1.46	14.60
60°	1.0	1.0153	1.53	15.30

Table 5.7: Calculated Height and Errors at Varying LH_2 Sloshing Angles

The results of the calculated absolute error between both levels are presented in Figure 5.16 for each angle, showing a similar trend in absolute error across all angles.

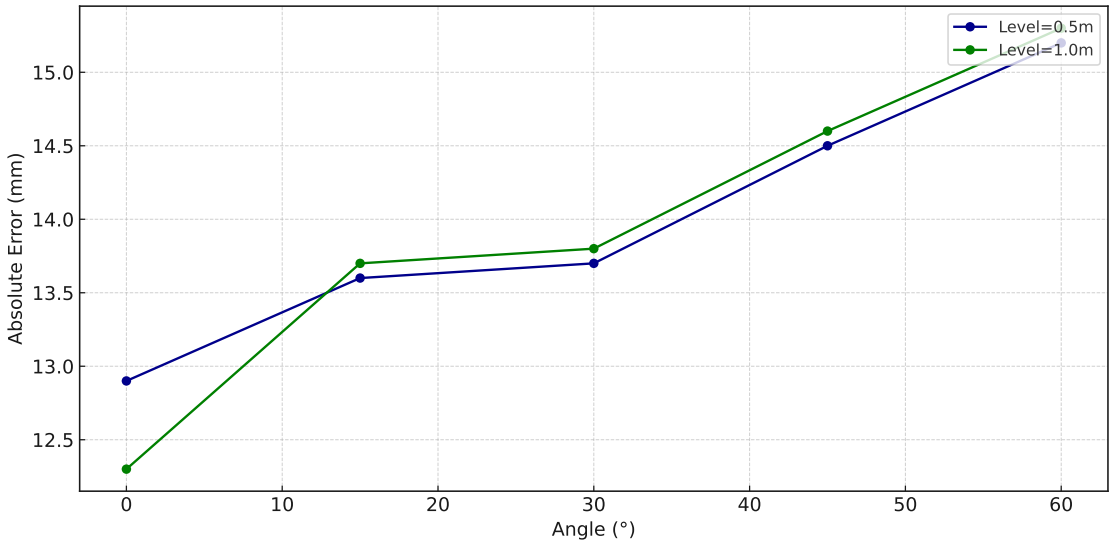

Figure 5.16: Absolute Error vs Sloshing Angle

Result for Different Temperature

To find out the effect on accuracy with varying temperatures, measurements were taken at LH_2 level of 0.21 m and compared between temperatures of 18 K,19 K and 20k. The corresponding speed of sound and density values used for the simulation are provided

in Table (5.8). Additionally, the corresponding dynamic viscosity, thermal conductivity, and specific heat ratio for each temperature were sourced from (21).

Temperature (K)	Speed of Sound (m/s)	Density (kg/m^3)
18	1146	73.37
19	1121	72.33
20	1097	71.23

Table 5.8: Speed of Sound and Density Corresponding to Each Temperature Used in Simulation

The simulation results are presented as follows. In Figure 5.17, the acoustic pressure of the reflected echo at the source is shown for all three temperatures (18 K, 19 K, and 20 K). It is observed that lower temperatures correspond to higher measured pressures due to reduced thermo-viscous dissipative losses, whereas higher temperatures result in greater losses.

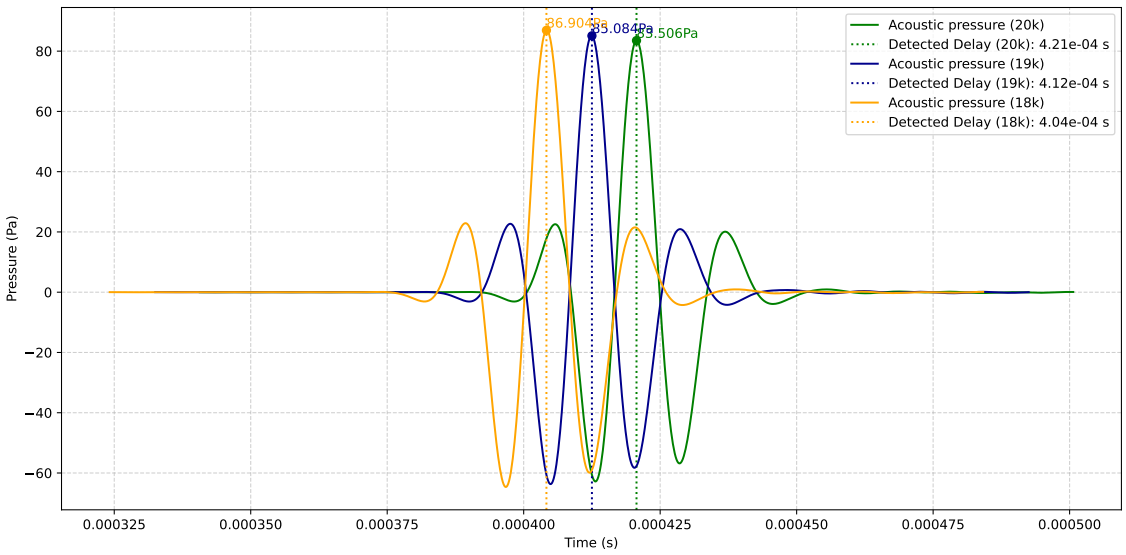

Figure 5.17: Pressure of Reflected Echo at Source for T = 18K,19K and 20K

Following this, Figure 5.18 shows the voltage of the echo measured at the transducer for each temperature, displaying a similar trend to that observed for acoustic pressure, where lower temperatures correspond to higher measured voltages.

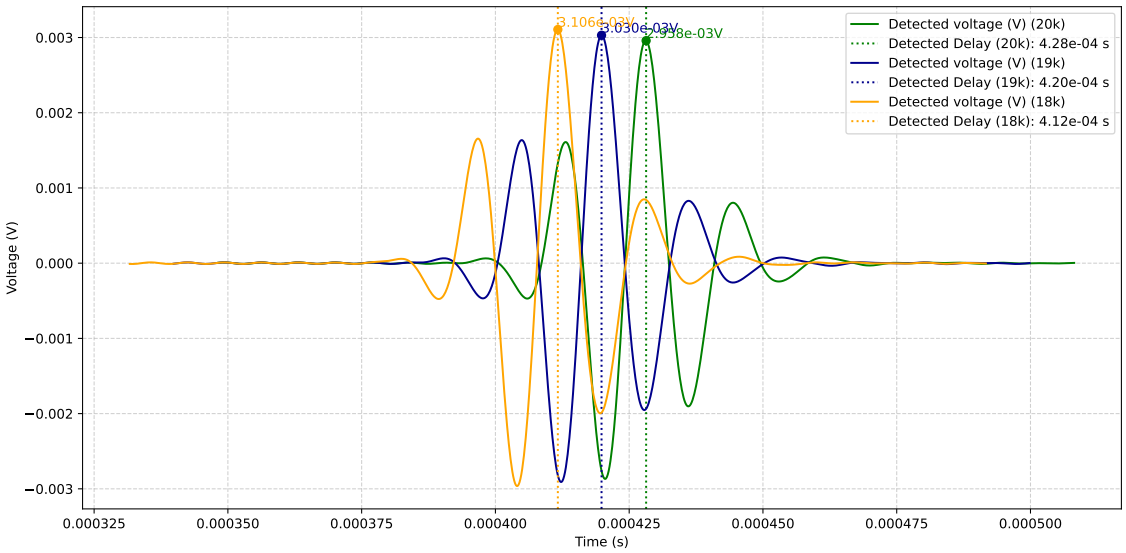

Figure 5.18: Detected Voltage of Reflected Echo at Source for T = 18K, 19K and 20K

Figure 5.19 shows the cross-correlation between the emitted signal and the received voltage signal, representing the true time-of-flight of the ultrasound echo for each temperature. Additionally, the time lag between the received echo voltages from the LH_2/GH_2 interface at 19 K and 20 K is presented in Figure 5.20 below.

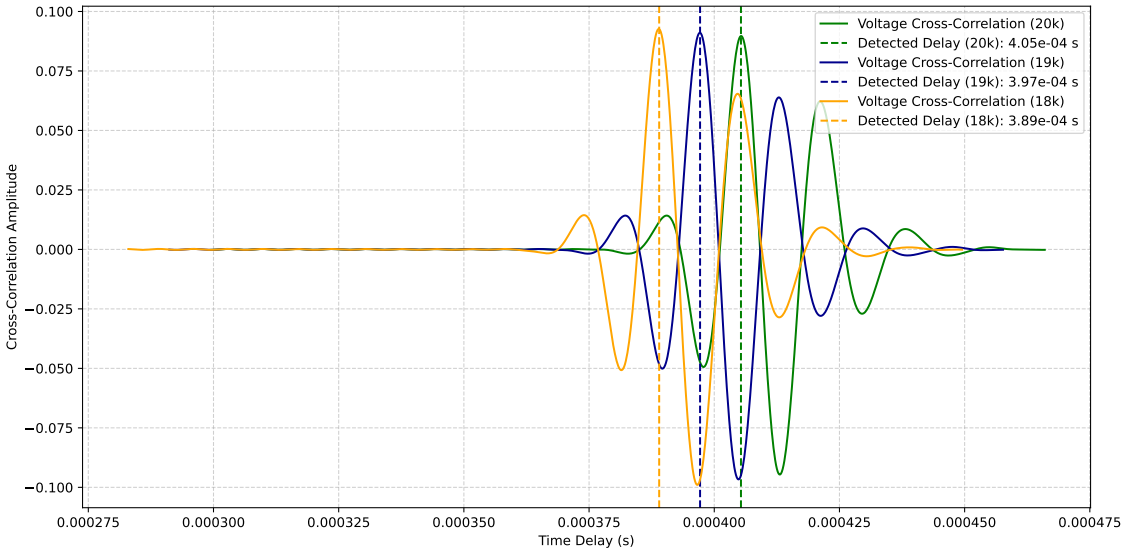

Figure 5.19: True TOF for T=18K, 19K and 20K at the LH_2 Level of 1 m

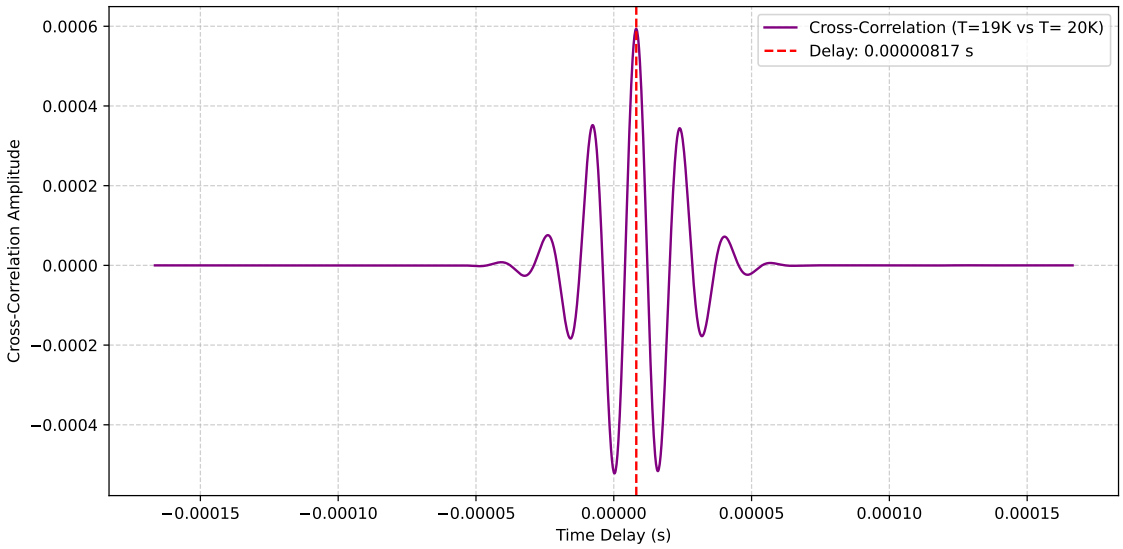

Figure 5.20: Time delay between 19k and 20k Detected Voltage echo

The results measured from all three simulations are presented in the table below. Table (5.9) shows the measured time lag from 0 s to the maximum amplitude of the received signal, the cross-correlation between the emitted and received signals representing the true time delay, and the maximum amplitude of the voltage received in the transducer for each temperature.

After calculating the true time delay, the corresponding height for each temperature is determined using the corresponding speed of sound and true time-of-flight (TOF). These calculated heights, along with the relative and absolute errors between the measured levels, are presented in the Table (5.10) below.

Temperature (K)	LH_2 Level (m)	Delay TOF (s)	True TOF (s)	Max Amplitude (mV)
18	0.21	0.4116	0.3890	3.106
19	0.21	0.4198	0.3972	3.021
20	0.21	0.4281	0.4053	2.950

Table 5.9: Measured Simulation Values

Temperature (K)	Level (m)	Calculated Level (m)	Relative Error (%)	Absolute Error (m)
18	0.21	0.22289	6.13	12.89
19	0.21	0.22226	5.83	12.26
20	0.21	0.22223	5.82	12.23

Table 5.10: Calculated Height from True Delay

5.3 Evaluation and Discussion

Across the varying LH_2 levels measured from 10%-90%, it is observed that the relative error decreases with increasing levels, while the absolute error remains between 12.3 mm and 12.5 mm, with an average of 12.36 mm. At lower levels, the relative error is notably higher, reaching approximately 5.85% at an LH_2 level of 0.21 m. Additionally, the maximum amplitude of the voltage in the transducer, due to the received echo of the acoustic wave, decreases as the LH_2 level increases. This decrease is due to higher attenuation of the LH_2 over longer distances

With frequency analysis, it has been observed that both absolute and relative errors decrease with increasing frequency, leading to improved measurement accuracy. Specifically, increasing the frequency enhances accuracy by reducing the absolute error from 12.3 mm at 50 kHz to 8.5 mm at 100 kHz, and further to 7.8 mm at 125 kHz for an LH_2 level of 0.21 m. This improvement corresponds to a reduction in relative error from 5.85% to 3.58%. However, with increasing frequency, the value of the received acoustic pressure decreased from 83.51 Pa to 44.04 Pa, indicating greater attenuation of the ultrasound at higher frequencies due to increased attenuation effects.

For varying sloshing angles of the LH_2 surface, the error was observed to increase consistently and linearly, with the absolute error rising from 12.33 mm at 0° to 15.30 mm at 60°. The relative error increased by approximately 0.5% at both levels. Another notable observation was the change in acoustic pressure received at the source for the same LH_2 level but different surface angles. The acoustic pressure decreased from 69.25 Pa at 0° to 13.85 Pa at 60° at 1m Level, resulting in a corresponding drop in detected voltage from 0.912 mV to 0.334 mV . At an oblique surface angle, the reflection occurs at the same angle relative to the normal, causing the reflected wave to diverge away from the transducer as shown in the Figure 3.1. This reduces the amount of reflected energy

that returns to the receiver, leading to a lower detected acoustic pressure and eventually lower Voltage(10).

From the simulations, Measurements indicate that lower temperatures in LH_2 result in higher absolute errors. This effect is primarily due to the increased speed of sound at lower temperatures, with a speed about 4.5% higher at 18K compared to 20K. Since the wavelength of ultrasound in the medium is directly proportional to the speed of sound, a higher speed of sound leads to a longer wavelength. This longer wavelength, in turn, reduces the measurement resolution, resulting in lower accuracy for the same frequency.

In the simulation of the 2D model to measure the effect of different sloshing angles, the amount of voltage due to the echo of the reflected pressure wave measured at the source was observed to be lower than that in the 2D axisymmetric model. The parameters used in both models were identical, except for the sloshing level. It was observed that, in the axisymmetric model, the initial pressure at the source for the same conditions was approximately 361 Pa, while in the 2D model with different sloshing angles, it was only around 258 Pa. This difference directly impacted the amount of acoustic pressure propagated and reflected as an echo. A cylindrical transducer, which is the default in the 2D axisymmetric model, was used in the symmetrical analysis, while a rectangular transducer was employed in the 2D model. The piezoelectric material's shape directly affects the amount of acoustic pressure generated, with the cylindrical PZT shape proving to be more efficient than the rectangular shape in generating acoustic pressure(52).

One significant challenge encountered during the simulation was the detection of the received voltage, which was measured in the millivolt range. The low amplitude of the received signal highlights the necessity of amplification to ensure easier and more accurate signal processing. Without proper amplification, in real-life scenarios, the weak signal is prone to noise interference from reflections and existing acoustic pressure, making it difficult to extract meaningful data. This finding underscores the importance of designing robust signal amplification and processing mechanisms to enhance the reliability and accuracy of the ultrasonic level sensor.

Furthermore, the piezoelectric transducer was simplified to include only the piezoelectric element without a matching layer, which reduced the sensitivity of the transducer. Incorporating a matching layer would allow higher acoustic pressure to be transmitted into the LH_2 medium, resulting in stronger reflections and larger acoustic pressures being detected by the transducer. Consequently, a higher voltage signal could be generated, improving the overall detection capability of the piezoelectric transducer.

5.4 Limitations of Numerical model

For the simulations, several idealized conditions were assumed, differing significantly from the complexities of real-world measurements of LH_2 . In the simulations, LH_2 was modelled as a stationary fluid. However, in practical scenarios, the liquid is not stationary; it responds to the dynamic motion of the aircraft and fluctuations in the liquid surface level. The sloshing of LH_2 within the tank can lead to mixing with GH_2, potentially altering the thermodynamic equilibrium of the LH_2. These changes can significantly impact both the temperature and density of the LH_2, thereby affecting the accuracy of the measurements.

Another key assumption was that the temperature within both LH_2 and GH_2 remains constant, with no boil-off of LH_2. This assumption oversimplifies the thermal conditions present in actual cryogenic tanks. In reality, heat leakage into cryogenic LH_2 tanks leads to continuous boil-off of LH_2, causing a gradual temperature gradient to develop along the fuel level over time. The boil-off gas increases the internal tank pressure, and as the pressure rises, the density of LH_2 decreases along the vapour pressure line. These changes directly affect the speed of sound and acoustic impedance in both the liquid and gaseous phases, introducing variability in signal transmission and reflection. Additionally, the temperature gradient along the LH_2 level leads to variations in the speed of sound, which significantly impacts measurement accuracy. Simulations demonstrated that, for the same frequency, changes in the speed of sound result in noticeable differences in measurement accuracy.

In the simulation, bulk viscosity was neglected, leading to an underestimation of acoustic attenuation. In practical scenarios, LH_2 is likely to exhibit slightly higher acoustic energy loss than the values predicted by the simulations. Furthermore, the presence of boil-off gas bubbles inside the Stillwell can scatter ultrasound waves within the cryogenic tank, adding another layer of complexity to accurate measurement.

These limitations highlight the importance of experimental validation to quantify and mitigate the effects of real-world conditions. Experimentally, utilizing piezoelectric materials such as strontium titanate, which exhibit a stronger piezoelectric effect at cryogenic temperatures, could significantly enhance detectability compared to the materials used in the simulations. Despite these challenges, the simulations provide valuable insights into the fundamental behaviour of ultrasound propagation in LH_2 and GH_2, offering a solid foundation for further refinement of the measurement principles.

6 Conclusion

This study explored the ultrasonic level sensor as an innovative solution for determining the level of LH_2 in aircraft cryogenic tanks. To investigate the acoustic behaviour of ultrasound in LH_2, Numerical model of the ultrasound sensor was developed and tested using COMSOL Multiphysics 6.2. The findings revealed that placing the ultrasonic sensor in LH_2 provided high sensitivity for detecting the liquid level, though it resulted in lower transmission of acoustic waves into GH_2, making it a viable method for level detection.

Several parameters were examined to evaluate the accuracy and reliability of the ultrasonic sensor under specific conditions, including stationary fluid levels, the absence of thermal gradients within the tank, limited boil-off within the liquid, and no reflections from the tank surface. Under these conditions, using a 50 kHz ultrasonic signal, it was found that the relative error of the ultrasonic measurement decreased with increasing fuel levels, while the absolute error remained within the range of 12.3 to 12.5 mm. Higher frequencies were observed to improve measurement accuracy. Additionally, the detected signal amplitude and the accuracy varied linearly with the inclination of the fuel surface, with the lowest detection occurring at an angle of 60°, as detailed in Section (5.2).

Simulations conducted between 18 K and 20 K revealed that temperature has a direct influence on the accuracy of level measurements. Variations in LH_2 temperature significantly impacted the acoustic behaviour of ultrasound waves, altering the speed of sound and, consequently, the sensor's measurement accuracy. These findings underscore the critical relationship between cryogenic temperature variations and ultrasonic sensor performance. For example, at lower temperatures, the increased speed of sound led to higher absolute errors.

To validate the use of ultrasonic sensors experimentally, the application of piezoelectric materials such as strontium titanate (SZT), which exhibits enhanced piezoelectric effects at cryogenic temperatures, is recommended. Experimental testing with SZT

could significantly improve detectability and provide critical insights into the real-world performance of ultrasonic sensors for cryogenic applications.

Bibliography

[1] A. Alekseev, T. Arndt, C. Haberstroh, J. T. *et al.*, "Hydrogen liquefaction, storage, transport, and application of liquid hydrogen," *Hydrogen Flagship Project TransHyDE*, 2023, available at KIT, Institute of Technical Physics.

[2] N. M. N. D. J. Mangold, D. Silberhorn *et al.*, "Refueling of lh2 aircraft assessment of turnaround procedures and aircraft design implication," *Energies*, vol. 15, no. 7, p. 2475, March 2022, [Online]. Available: https://doi.org/10.3390/en15072475.

[3] I. Moir and A. Seabridge, *Aircraft Systems: Mechanical, Electrical, and Avionics Subsystems Integration*, 3rd ed. Chichester, West Sussex, England: John Wiley & Sons, 2008, [Online]. Available: https://www.wiley.com.

[4] T. Chen, M. Maklad, P. R. Swinehart, and K. P. Chen, "Self-heated optical fiber sensor array for cryogenic fluid level measurement," *IEEE Sensors Journal*, vol. 10, no. 10, pp. 1632–1636, 2010. [Online]. Available: https://ieeexplore.ieee.org/document/5582187

[5] Control.com, "Capacitive level measurement," 2024, accessed: 2024-11-05. [Online]. Available: https://control.com/textbook/continuous-level-measurement/capacitive/

[6] M. Farrèr, "Differential pressure measurement in industrial applications," 2024, accessed: 2024-11-16. [Online]. Available: https://keller-druck.com/en/company/blog/differential-pressure-measurement-in-industrial-applications

[7] K. Gutiq and K. Kochan, "Modellbasierte entwicklung: experimentelle erprobung von sensortechnologien für tanks," *Mobiles: Fachzeitschrift für Konstrukteure*, vol. 44, pp. 26–29, 2023. [Online]. Available: https://reposit.haw-hamburg.de/handle/20.500.12738/14923

[8] D. S. B. B. T. Burschyk, Y. Cabac and B. Nagel, "Liquid hydrogen storage design trades for a short-range aircraft concept," *CEAS Aeronautical Journal*, vol. 14, no. 4,

pp. 879–893, 2023. [Online]. Available: https://link.springer.com/article/10.1007/s13272-023-00689-4

[9] V. F. R. Morales-Ospino, A. Celzard, "Boil-off hydrogen (boh): Challenges and mitigation strategies in cryogenic storage," 2024, accessed: Nov. 05, 2024. [Online]. Available: https://hal.univ-lorraine.fr/hal-04146246/document#:~:text=Boil%2Doff%20hydrogen%20(BOH)%20is%20the%20result%20of%20the,atmosphere%2C%20resulting%20in%20wasted%20energy.

[10] T. D. Rossing, *Springer Handbook of Acoustics*, 2nd ed. Springer, 2014. [Online]. Available: http://extras.springer.com/2014/978-1-4939-0755-7

[11] F. Suñol, D. A. Ochoa, L. R. Suñé, and J. E. García, "Design and characterization of immersion ultrasonic transducers for pulsed regime applications," *Instrumentation Science & Technology*, vol. 46, no. 6, pp. 637–651, 2018. [Online]. Available: https://upcommons.upc.edu/bitstream/handle/2117/131090/instr-sci-tech-postprint.pdf

[12] F. T. Dodge, "Propellant mass gauging: Database of vehicle applications and research and development studies," Southwest Research Institute, San Antonio, TX, USA, Tech. Rep., August 2008.

[13] R. Langton, C. Clark, M. Hewitt, and L. Richards, *Aircraft Fuel Systems*. Hoboken, NJ, USA: Wiley, 2009.

[14] International Air Transport Association, "Net Zero Roadmaps," 2024, accessed: 2024-11-05. [Online]. Available: https://www.iata.org/en/programs/sustainability/roadmaps/

[15] The International Council on Clean Transportation, "Fuel Efficiency Trends for New Commercial Jet Aircraft: 1960 to 2014," 2015, accessed: 2024-11-18. [Online]. Available: https://theicct.org/publication/fuel-efficiency-trends-for-new-commercial-jet-aircraft-1960-to-2014/

[16] United Nations, "What is Climate Change?" 2024, accessed: 2024-11-18. [Online]. Available: https://www.un.org/en/climatechange/what-is-climate-change

[17] W. contributors, "Tupolev tu-155," https://en.wikipedia.org/wiki/Tupolev_Tu-155, 2024, accessed: 05-Nov-2024.

[18] H. GmbH, "H2fly and partners complete world's first piloted flight of liquid hydrogen powered electric aircraft," 2023, accessed: 05-Nov-2024.

[19] J. H. A. Lanz and C. Messer, "Hydrogen fuel cell engines and related technologies," National Renewable Energy Laboratory, Tech. Rep., December 2001. [Online]. Available: https://rosap.ntl.bts.gov/view/dot/14966

[20] K. Seeckt and D. Scholz, "Jet versus prop, hydrogen versus kerosene for a regional freighter aircraft," in *Proc. Deutscher Luft- und Raumfahrtkongress*, 2009, [Online]. Available: https://www.fzt.haw-hamburg.de/pers/Scholz/GF/GF_Paper_DLRK_09-09-08.pdf.

[21] J. H. R. D. McCarty and H. M. Roder, *Selected Properties of Hydrogen (Engineering Design Data)*. Boulder, CO, USA: National Bureau of Standards, February 1981.

[22] J. Sequeira, A. Sinha, and S. Sinha, "Some aspects of cots ultrasonic fuel level measurement," in *2017 IEEE Aerospace Conference*. Big Sky, MT, USA: IEEE, March 2017, pp. 1–8. [Online]. Available: https://ieeexplore.ieee.org/document/7988823

[23] FlightGlobal, "Boeing modifying 777 fuel indicator after in-flight discrepancy incidents," *FlightGlobal*, 2020, [Online]. Available: https://www.flightglobal.com/safety/boeing-modifying-777-fuel-indicator-after-in-flight-discrepancy-incidents/138706.article. Accessed: 2024-10-25.

[24] G. L. D. Becker, R. Schmidt and K. S. Drese, "Ultrasound measurement technique for validation of cryogenic flows," in *Proc. EUROSOENSORS 2018 Conf.*, vol. 2, no. 13. Graz, Austria: MDPI, Sep. 2018, p. 1090, [Online]. Available: https://doi.org/10.3390/proceedings2131090.

[25] J. G. D. B. M. Siegl, A. Fischer *et al.*, "Advanced sensor technologies for cryogenic liquid propellant flow phenomena," in *Proc. 66th Int. Astronautical Congress (IAC)*. Jerusalem, Israel: International Astronautical Federation (IAF), 2015, pp. 1–7, [Online]. Available: https://elib.dlr.de/98716/1/IAC-15%2CC4%2C5%2C2%2Cx30555.pdf.

[26] H. M. Roder, *Density and Liquid Level Measurement Instrumentation for the Cryogenic Fluids Oxygen, Hydrogen, and Nitrogen*, ser. NASA SP-3083. National Aeronautics and Space Administration (NASA), 1974. [Online]. Available: https://ntrs.nasa.gov/api/citations/19740014209/downloads/19740014209.pdf

[27] R. G. Amamchyan, Y. N. Golunskii, V. I. Shchedrin, and V. A. Shcherbinin, "A cryogenic sensor of an ultrasonic level gauge," *Instruments and Experimental Techniques*, vol. 46, no. 4, pp. 578–579, 2003. [Online]. Available: https://link.springer.com/article/10.1023/A:1025171124170

[28] W. L. R. A. P. H. M. C. A. R. Parker, Jr. and J. A. Bakalyar, "Cryogenic liquid level sensor apparatus and method," Patent, July 7, 2015, u.S. Patent nr 20150014985. [Online]. Available: https://patents.google.com/patent/US9074921B1/en

[29] H. M. Chan, "Novel fiber optic sensing arrays with enhanced sensitivity in cryogenic temperatures," NASA Armstrong Flight Research Center, Edwards, California, NASA Technical Memorandum NASA/TM-20205009645, August 2021. [Online]. Available: https://ntrs.nasa.gov/api/citations/20205009645/downloads/20205009645.pdf

[30] K. A. Y. N. S. A. K. Matsumoto, M. Sobue and T. Numazawa, "Capacitive level meter for liquid hydrogen," *Cryogenics*, vol. 51, pp. 114–115, 2011, [Online]. Available: https://doi.org/10.1016/j.cryogenics.2010.11.005.

[31] T. Neeser and R. Kuechenmeister, "Differential pressure gauge for cryogenic fluids," Patent US 6,542,848 B1, April, 2003, [Online]. Available: https://patents.google.com/patent/US6542848B1/en. Patent issued on Apr. 1, 2003.

[32] R. J. P. Scholtes, "Design of a level sensing system for the propellant tank of a microlauncher," Master's thesis, KTH Royal Institute of Technology, Stockholm, Sweden, May 2021, second Cycle, 30 Credits, School of Electrical Engineering and Computer Science.

[33] Aerospace Technology Institute. (2021, September) Primary energy source comparison and selection. [Online]. Available: https://www.ati.org.uk/wp-content/uploads/2021/09/FZ_0_6.1-Primary-Energy-Source-Comparison-and-Selection-FINAL-230921.pdf. Accessed: Nov. 14, 2024.

[34] R. Parello, Y. Gourinat, E. Benard, and S. Defoort, "Structural sizing of a hydrogen tank for a commercial aircraft," in *Journal of Physics: Conference Series*, vol. 2716. IOP Publishing, 2024, p. 012040, eASN-2023 Conference. [Online]. Available: https://doi.org/10.1088/1742-6596/2716/1/012040

[35] M. Gollnow, "Passenger aircraft towards zero emission with hydrogen and fuel cells," Hamburg University of Applied Sciences, Tech. Rep., 2022, [Online]. Available: https://archive.org/details/TextGollnow.pdf.

[36] Y. F. Z. Liu and G. Lei, "Fluid sloshing dynamic performance in a liquid hydrogen tank," *International Journal of Hydrogen Energy*, vol. 44, pp. 13 885–13 894, 2019, [Online]. Available: https://doi.org/10.1016/j.ijhydene.2019.04.014.

[37] A. S. E. Frosina and A. Andreozzi, "Experimental and numerical analyses of the sloshing in a fuel tank," *Energies*, vol. 11, p. 682, 2018, [Online]. Available: https://doi.org/10.3390/en11030682.

[38] Aerospace Technology Institute, "Cryogenic hydrogen fuel system and storage roadmap report," Aerospace Technology Institute, Tech. Rep., March 2022, [Online]. Available: https://www.ati.org.uk/wp-content/uploads/2022/03/FZO-PPN-COM-0027-Cryogenic-Hydrogen-Fuel-System-and-Storage-Roadmap-Report.pdf.

[39] J. Mukhopadhaya and D. Rutherford, "Performance analysis of evolutionary hydrogen-powered aircraft," International Council on Clean Transportation, Tech. Rep., 2022. [Online]. Available: https://theicct.org/wp-content/uploads/2022/01/LH2-aircraft-white-paper-A4-v4.pdf

[40] COMSOL Multiphysics, *Acoustics Module User's Guide*, 2018, cOMSOL 5.4 Documentation. [Online]. Available: https://doc.comsol.com/5.4/doc/com.comsol.help.aco/AcousticsModuleUsersGuide.pdf

[41] A. Forum, "Ultrasonic level transmitter working principle," October 2024, online. [Online]. Available: https://automationforum.co/ultrasonic-level-transmitter-working-principle/

[42] W. Gao, W. Liu, F. Li, and Y. Hu, "Analysis and validation of ultrasonic probes in liquid level monitoring systems," *Sensors*, vol. 21, no. 4, p. 1320, 2021.

[43] J. Allen, "Chapter 6: Acoustic reflection and transmission," https://jontallen.ece.illinois.edu/uploads/473.F18/Lectures/Chapter_6a.pdf, accessed: 2024-11-15.

[44] COMSOL Multiphysics, *Introduction to the Acoustics Module*, 2018, cOMSOL 5.4 Documentation. [Online]. Available: https://doc.comsol.com/5.4/doc/com.comsol.help.aco/IntroductionToAcousticsModule.pdf

[45] S. R. Durkee, "Ultrasonic liquid gauging system," Patent US6 236 142B1, 2001, available at: https://patents.google.com/patent/US6236142B1/en.

[46] D. E. Grupp and A. M. Goldman, "Giant piezoelectric effect in strontium titanate at cryogenic temperatures," *Science*, vol. 276, no. 5312, pp. 392–394, April 1997. [Online]. Available: http://www.sciencemag.org

[47] Onda Corporation, "Acoustic properties of rubbers," 2003, accessed: 2024-11-17. [Online]. Available: https://www.ondacorp.com/images/Rubbers.pdf

[48] R. E. Birkett, "Baffle assembly for ultrasonic liquid level measuring probe," Patent US5 456 108, 1995, available at: https://patentimages.storage.googleapis.com/d1/e1/ff/c4618d04268bf2/US5456108.pdf.

[49] J. Huang, "How to model piezoelectric devices as both transmitters and receivers," December 2018, accessed: 2024-11-17. [Online]. Available: https://www.comsol.com/blogs/how-to-model-piezoelectric-devices-as-both-transmitters-and-receivers

[50] The Airline Pilots Forum Archive. (n.d.) Boeing 777 non-normal procedures. [Online]. Available: https://theairlinepilots.com/forumarchive/b777/b777nonnormalprocedures.pdf. Accessed: Nov. 14, 2024.

[51] CFI Notebook. (n.d.) Steep turns - maneuvers and procedures. [Online]. Available: https://www.cfinotebook.net/notebook/maneuvers-and-procedures/airborne/steep-turns. Accessed: Oct. 25, 2024.

[52] L. Y. X. L. J. H. L. Zhang, K. Yan and X. Chou, "Design and fabrication of high-performance piezoelectric micromachined ultrasonic transducers based on aluminum nitride thin films," *Micromachines*, vol. 15, no. 8, p. 1001, 2024, [Online]. Available: https://doi.org/10.3390/mi15081001.

Declaration of Independent Work

Hereby, I declare that I have independently authored the Bachelor's Thesis titled: **Numerical Study of Ultrasound-Based Level Sensors in Liquid Hydrogen Tanks** using only the specified resources. All passages, figures, and tables taken verbatim from literature or other sources are quoted with an indication of the source.

Hamburg, 20.11.2024 Chhabi Lal Bashyal

Appendix A - Python script for validation of the Model

This appendix provides the Python script used to validate the simulation model by analysing the echo region and comparing the start time with the theoretical time of flight.

```
import pandas as pd
import numpy as np

# Load simulation data
file_path = 'validation_75cm.txt'
# Column in the files
columns = ["Time", "Total acoustic pressure (Pa)", "Terminal voltage (V)"]
data = pd.read_csv(file_path, sep=r"\s+", skiprows=6, names=columns)

# Extract time and voltage data
time = data["Time"].values
voltage = data["Terminal voltage (V)"].values

# Define parameters
height = 0.75  # Height of liquid in meters
speed = 1097   # Speed of sound in liquid hydrogen in m/s
theoretical_time = (height / speed) * 2  # Theoretical time of flight

#  start index for echo search near the theoretical time
```

```
start_index = np.argmax(time >= theoretical_time * 0.9)  # Start 10% before theoretical time

# the threshold as 0.05% of the maximum absolute voltage
threshold = 0.05 * np.max(np.abs(voltage[start_index:]))
echo_start_index = start_index + np.argmax(np.abs(voltage[start_index:]) > threshold)

# Get the time corresponding to the start of the echo region
time_echo_start = time[echo_start_index]

print(f"Time for 0.05% of the start of the echo region: {time_echo_start:.6e} seconds")
```

Listing 1: Python script for model validation.

Appendix B - Python Script for TOF measurement

This appendix provides the Python script used for processing simulation data, calculating time delay, and analysing maximum amplitudes in the echo region. The script handles multiple files, processes acoustic signals, and saves the results to a text file.

```
import numpy as np
import pandas as pd
import os

# Result extracted from the simulation
data_files = [
    '10%_LH2.txt',
    '20%_LH2.txt',
    '30%_LH2.txt'
]

# Sound speed and expected distances for each file in meters
distances = [0.1*2.1, 0.2*2.1, 0.3*2.1]
sound_speed = [1097, 1097, 1097]  # m/s

results = []

# Iterate over each file and calculate time delay and max
   amplitude within the expected echo region
for i, file_path in enumerate(data_files):
    try:
        # Check if file exists
        if not os.path.isfile(file_path):
```

```
23            print(f"File not found: {file_path}")
24            continue
25
26        # Load data
27        data = pd.read_csv(file_path, delimiter='\s+',
              skiprows=7, names=["Time", "Pressure", "Voltage"])
28        time = data["Time"].values
29        voltage = data["Voltage"].values
30
31        # Expected delay based on distance
32        expected_tof = (distances[i] / sound_speed[i]) * 2
              # two-way travel time
33        expected_tof_samples = int(expected_tof / (time[1] -
              time[0]))  # Convert to samples
34
35        # Define a search range around the expected echo
              region
36        start_index = max(0, expected_tof_samples - 500)
37        end_index = min(len(voltage), expected_tof_samples +
              500)
38        if start_index >= end_index:
39            print(f"Invalid search range for file
                  {file_path}")
40            continue
41
42        # Find maximum voltage within the expected echo
              region and its corresponding time
43        max_voltage_amplitude =
              np.max(voltage[start_index:end_index]) * 1000  #
              Convert to mV
44        time_max_voltage_amplitude = time[start_index +
              np.argmax(voltage[start_index:end_index])]
45
46        # Assume the transmitted signal is the initial part
              of the received signal
47        reference_signal = voltage[:5000]
```

```
48
49          # Calculate cross-correlation between the reference
               and the received signal
50          cross_corr = np.correlate(voltage, reference_signal,
               mode='full')
51          lags = np.arange(-len(reference_signal) + 1,
               len(voltage))
52
53          # Limit the cross-correlation plot around the
               expected TOF
54          search_range = (len(reference_signal) - 1 +
               start_index, len(reference_signal) - 1 +
               end_index)
55          limited_lags = lags[search_range[0]:search_range[1]]
56          limited_cross_corr =
               cross_corr[search_range[0]:search_range[1]]
57
58          # Detect peak in cross-correlation within the search
               range
59          peak_index = np.argmax(limited_cross_corr)
60          found_delay_samples = limited_lags[peak_index]
61          found_delay_time = found_delay_samples * (time[1] -
               time[0])  # Convert samples to time
62
63          # Append results for this file to the list
64          results.append({
65              "File": file_path,
66              "Distance (m)": distances[i],
67              "Detected Delay (s)": found_delay_time,
68              "Maximum Amplitude (mV)": max_voltage_amplitude,
69              "Time of Max Voltage (s)":
                   time_max_voltage_amplitude
70          })
71
72      except Exception as e:
73
```

```
74 # Write results to a .txt file
75 with open('results.txt', 'w') as f:
76     for result in results:
77         f.write(f"File: {result['File']}\n")
78         f.write(f"Distance: {result['Distance (m)']} m\n")
79         f.write(f" True Detected Delay: {result['Detected
              Delay (s)']:.8f} seconds\n")
80         f.write(f"Maximum Amplitude in Echo Region:
              {result['Maximum Amplitude (mV)']:.8f} mV\n")
81         f.write(f"Time of Maximum Voltage in Echo Region
              from 0s: {result['Time of Max Voltage (s)']:.8e}
              s\n")
82         f.write("-" * 40 + "\n")
83
84 print("'results.txt'")
```